

AN ABSTRACT OF THE DISSERTATION OF

Harrison Neal for the degree of Doctor of Philosophy in Chemistry presented on June 7, 2018.

Title: Organic/Inorganic Hybrid Materials of Uranyl Peroxide Clusters and Uranium Minerals

Abstract approved:

May Nyman

Frontier research of non-aqueous actinide clusters is discussed. Since the inception of the uranyl peroxide clusters over the last decade, they have only been synthesized and characterized as solid crystals and in aqueous solution. This thesis provides thorough characterization of aqueous uranyl clusters and the first demonstration of uranyl cluster transfer and characterization in organic solvents. Uranyl peroxide clusters self-assemble in mild alkaline solution in the presence of peroxide. Primary solution characterization used throughout this work is Small-Angle X-ray Scattering (SAXS), giving information on particle size, shape, and electron density contrast. SAXS characterization shows the capsule-structures of clusters are maintained, but unique behavior is observed under further characterization. Hydrophilic encapsulated counterions (i.e. alkalis, ammonium) become isolated in this hydrophobic environment. Immobile counterion environments are specific to cluster identity, allowing for variable-temperature solution Nuclear Magnetic Resonance (NMR) spectroscopy of ion exchange dynamics within clusters. This provides an unprecedented opportunity to probe structure of lithium atoms, not visible under x-ray diffraction, leading to an understanding of self-assembly and stabilization of clusters. Research of uranyl peroxide clusters in the organic phase have led to discoveries of a new cluster structures not seen before in an aqueous environment. Study of uranyl

species in an organic solution has implications for back-end nuclear fuel processing and separations within the nuclear fuel cycle. The use of polynuclear clusters for separation chemistry, and simple ion association as the mechanism of phase transfer is not currently employed in nuclear fuel reprocessing or radionuclide separations. All current processes utilize molecular complex formation or inorganic, solid-phase ion exchangers. Distinct benefits offered by the process presented here include; 1) the extractant molecules are benign, and 2) the process functions best if their concentration is sub-stoichiometric to the uranium concentration, yielding an 'atom efficient' process. These features are compared to the Plutonium Uranium Redox Extraction (PUREX) processes. Additionally, transition and rare earth metals precipitate in the alkaline aqueous conditions in which these clusters self-assemble, which provides initial separation of many isotope decay products. As uranyl peroxide clusters are considered a molecular analogue of the uranyl mineral, studtite; other uranyl mineral compounds were explored. Solid-state studies of layered uranyl minerals theoretically allows for intercalation of organic molecules for exfoliation and eventual solution/film preparation. This could also lead to clusters with different dimensionalities, derived from the layer structural motifs. Improved synthesis, alkylamine intercalation and characterization of uranyl phosphate mineral, chernikovite, is discussed. Similar intercalation behavior can be seen in transition metal chalcogenides (TMC), revealing weak Van Der Waals interlayer interactions. This approach to non-aqueous uranyl clusters and uranium mineral compounds will stimulate much more in-depth and diverse studies in the scientific community.

©Copyright by Harrison Neal
June 7, 2018
All Rights Reserved

Organic/Inorganic Hybrid Materials of Uranyl Peroxide Clusters and Uranium
Minerals

by
Harrison Neal

A DISSERTATION

submitted to

Oregon State University

in partial fulfillment of
the requirements for the
degree of

Doctor of Philosophy

Presented June 7, 2018
Commencement June 2018

Doctor of Philosophy dissertation of Harrison Neal presented on June 7, 2018

APPROVED:

Major Professor, representing Chemistry

Chair of the Department of Chemistry

Dean of the Graduate School

I understand that my dissertation will become part of the permanent collection of Oregon State University libraries. My signature below authorizes release of my dissertation to any reader upon request.

Harrison Neal, Author

ACKNOWLEDGEMENTS

To my advisor Dr. May Nyman, for giving me the opportunity to work with her on advancing the field of uranyl cluster chemistry. Thank you for giving me all the guidance and ability to pursue all that I accomplished over the last 5 years. Your mentoring has been invaluable for my career and my life. It has been a privilege to be part of your research group.

To the Nyman research group members past and present for friendly conversation, support and brainstorming sessions. Especially:

Dr. Clément Falaise – for working with me for years, teaching me all your tricks in the chemistry laboratory and for sharing laughs and stories of life in France.

Karoly Kozma – for putting up with me and all of my poking and prodding on instrumentation. You have been a tremendous help during my Ph.D. work.

Dr. Lauren McQuade – for being the best friend and lab mate I could have asked for. Your questions (often silly) kept me on my toes. I'm happy to follow in your footsteps.

Dr. Omid Sadeghihosseinabadi – for all the interesting antics and fun conversations.

To Dr. Richard Nafshun – for mentoring me for the past 5 years. Your helpful guidance and conversation has kept me focused on the important goals in my education and my life.

To Dr. Todd Alam – for your NMR expertise, patience, and kind advice for my crazy/abstract ideas.

To the Burns Research Group for professional support and collaborations

To the Gagliardi Research Group for collaborations and computational experimentation.

To my Mom, Dad and sister Harmony – you have always been the best and most supportive. I can't thank you enough for all the love and drive you have given me to pursue my dreams in life. You have helped make my dream a reality.

To Haley – for loving and supporting me even when I’ve lost my mind. You have always been there to keep me sane and keep me smiling. I love you!

To Rowyn – for being my primary motivation over the last year. One day, I hope you read this and understand the love and care I have for you, my baby girl.

My family and friends have always supported and encouraged me to succeed in everything I do. I appreciate all of you for everything you have done for me.

CONTRIBUTION OF AUTHORS

M. N. provided substantial guidance for experiment design, project direction, result interpretation and manuscript edits. In Chapter 4, all authors provided edits and feedback during the writing process; J. S. provided data acquisition of Induced Coupled Plasma Mass Spectroscopy (ICP-MS); J. B. F. provided access to the ICP-MS instrumentation; P. C. B. and M. N. contributed to funding and project direction. In Chapter 5, all authors provided edits and feedback during the writing process. J. X. contributed significantly to writing and provided data/interpretation of computational results. J. S. provided data acquisition of Induced Coupled Plasma Mass Spectroscopy (ICP-MS); P. C. B. provided access to the ICP-MS instrumentation; T. M. A. provided data acquisition and interpretation of two-dimensional Nuclear Magnetic Resonance Spectroscopy (NMR) and solid-state NMR results; M. N. and L. G. contributed to funding and project direction. In Chapter 6, all authors provided edits and feedback during the writing process; K. K. provided data acquisition and interpretation of pair distribution function (PDF) analysis of total x-ray scattering; M. N. contributed to funding and project direction.

TABLE OF CONTENTS

	<u>Page</u>
1 Introduction to Uranium Chemistry.....	1
1.1 Uranium in the Nuclear Fuel Cycle.....	1
1.2 Chemistry of Uranium.....	5
2 Introduction to Aqueous Clusters.....	6
2.1 Cluster Chemistry of Transition Metals.....	6
2.2 Uranyl Clusters.....	8
3 Introduction to Characterization Techniques.....	16
3.1 Small Angle X-ray Scattering Introduction.....	16
3.2 Nuclear Magnetic Resonance Introduction	21
4 Benchmarking Uranyl Peroxide Capsule Chemistry in Organic Media.....	26
4.1 Abstract.....	27
4.2 Introduction	28
4.3 Results and Discussion.....	30
4.4 Conclusions.....	44
4.5 Experimental Section.....	44
4.6 Acknowledgements	47
5 Resolving Confined ^7Li Dynamics of Uranyl Peroxide Capsule U_{24}	48
5.1 Abstract	49
5.2 Introduction	50
5.3 Methods.....	53
5.3.1 Experimental Methods.....	53
5.3.2 Computational Methods.....	54

TABLE OF CONTENTS (Continued)

	<u>Page</u>
5.4 Experimental Results	56
5.5 Computational results.....	64
5.5.1 Cluster Model.....	64
5.5.2 Full U ₂₄ Cage Model.....	68
5.5.3 Explicit Water Molecules Studies.....	74
5.6 Conclusion.....	76
5.7 Acknowledgements.....	76
6 Synthetic Pathways and Exfoliation of Uranyl Phosphate Layered Materials	78
6.1 Abstract	79
6.2 Introduction	80
6.3 Experimental.....	82
6.4 Results and Discussion.....	83
6.5 Conclusion.....	89
6.6 Acknowledgements.....	89
7 Conclusions.....	90
8 Bibliography	92
9 Appendices	110
9.1 Supplementary Information for Chapter 4: Benchmarking Uranyl Peroxide Capsule Chemistry in Organic Media.....	110
9.2 Supplementary Information for Chapter 5: Resolving Confined ⁷ Li Dynamics of Uranyl Peroxide Capsule U ₂₄	123
9.3 Supplementary Information for Chapter 6: Synthetic Pathways and Exfoliation of Uranyl Phosphate Layered Materials.....	135

LIST OF FIGURES

<u>Figure</u>	<u>Page</u>
1.1 PUREX Process Versus Proposed Novel Extraction Model.....	4
2.1 Effect of pH on Group V & VI Transition Metal POMs.....	7
2.2 Clusters Across the Periodic Table.....	9
2.3 Uranyl Triperoxide Monomers to Cluster Self-Assembly.....	11
2.4 Templating Effect of Counterions in the Cluster Faces	12
2.5 Oligomer Ring Structures of Uranyl Peroxide Found in the Cluster Face	13
2.6 Uranyl Peroxide Clusters Description.....	15
3.1 SAXS Instrumentation Model.....	17
3.2 Qualitative Interpretation of SAXS Data.....	18
3.3 Quantitative Analysis of SAXS Data.....	20
3.4 Schematic of NMR instrumentation.....	22
3.5 Solution and Solid-state NMR of Aqueous LiU_{24} Cluster Species.....	24
4.1 Comparing Simulated and Experimental SAXS data for Aqueous Uranyl Peroxide Clusters.....	31
4.2 Extraction of Uranyl Peroxide Clusters into the Nonaqueous Phase.....	32
4.3 ^7Li NMR Data of U_{24} in Octadecene.....	37
4.4 Log q-log I(q) Scattering Curve for 0.75 M U ($\text{NH}_4\text{-U}_{32}$) extraction with TMAOH	38
4.5 Extraction of Uranium from SIMFUEL.....	40
4.6 Composition Analysis of SIMFUEL Extraction.....	42
5.1 Representations of the Topology of U_{24}	52
5.2 Solid-state and Two Dimensional NMR of U_{24}	57

LIST OF FIGURES (Continued)

<u>Figure</u>	<u>Page</u>
5.3 SAXS Comparison of Aqueous and Organic U ₂₄ cluster solutions.....	60
5.4 Experimental and Simulated Variable Temperature Solution NMR of U ₂₄ Clusters in Organic Solvent.....	63
5.5 Structures of Cluster Models with Different Li ⁺ Cation Coordination Environments.....	65
5.6 Optimized structures of full-cage U ₂₄ models.....	70
5.7 Li ⁺ Cation chemical Shift Models as a Function of z Coordination and Relative Single Point Energy (kcal/mol).....	73
5.8 Structures of Square Model with Solvated Li ⁺ Ions.....	75
6.1 Proposed Delamination Mechanism of Layered Chernikovite Structure.....	81
6.2 XRD data of Chernikovite Before and After Delamination.....	84
6.3 IR Spectra of Chernikovite Before and After Delamination.....	85
6.4 TEM Imaging of Chernikovite Layered Materials.....	86
6.5 PDF Analysis of Pristine Chernikovite and Delaminated Chernikovite.....	88

LIST OF TABLES

<u>Table</u>	<u>Page</u>
1.1 Simulated Spent Nuclear Fuel Composition.....	3
4.1 Composition Analysis (U, Br) of Aqueous Phase Post-extraction.....	35
5.1 ⁷ Li NMR Chemical Shift δ (ppm) and Relative Energy E (kcal/mol) of the Different Cluster Models.....	67
5.2 Formation Energy (ΔE) and Average Contribution (ΔE_{ave}) of the U ₂₄ Structure.....	71

LIST OF APPENDIX FIGURES

<u>Figure</u>	<u>Page</u>
S1.1 Raman Analysis of $\text{NH}_4\text{-U}_{32}$ Clusters.....	112
S1.2 SAXS Scattering from Solvents.....	113
S1.3 SAXS Scattering from Series of $\text{NH}_4\text{-U}_{32}$ Extracted with Different Surfactant: Cluster Ratios.....	114
S1.4 SAXS Scattering Contribution from CTAB Surfactant.....	115
S1.5 SAXS of Maximum Surfactant Concentration Extraction Sample.....	116
S1.6 SAXS of Uranyl Oxalate Cluster ($\text{U}_{60}\text{Ox}_{30}$).....	117
S2.1 SAXS Size Distribution Model of U_{24} Clusters in Aqueous and Organic Solvents.....	123
S2.2 Eyring Plots of CTA- U_{24} from Variable Temperature NMR Results.....	124
S2.3 ^7Li Solution NMR of CTA- U_{24} Contacted With Various Aqueous Solution...	125
S2.4 Structures of Hexagon Cluster Models with One Li^+ Cation.....	126
S2.5 Chemical Shift of Li Cation in Cluster Models as a Function of Different Functionals. Data are Present in Table S2.1.....	128
S2.6 Chemical Shift of Li Cation in Cluster Models as a Function of Solvent Types. Data are Present in Table S2.2.....	130
S3.1 Raman Spectra from Solid Chernikovite Samples.....	135
S3.2 Raman Spectra of Delaminated Chernikovite.....	136
S3.3 XRD Data of Delamination Trials of Chernikovite Using Cation Intercalate..	137
S3.4 SEM Images and Composition Data (EDX) of Chernikovite Delamination Samples.....	138
S3.5 Simulated PDF Peak of Chernikovite.....	139

LIST OF APPENDIX TABLES

<u>Table</u>	<u>Page</u>
S1.1 Experimental X-ray Scattering Data compared to structure metrics.....	118
S1.2 U_{32} and U_{24} Extraction Series Description.....	119
S1.3 R_g Values from SAXS Data Analysis of U_{24} and U_{32} Extraction Series.....	121
S2.1 Chemical shift of Li cation in cluster models using different functional with SMD(water) solvent model.....	127
S2.2 Chemical shift of Li cation in cluster models using different solvents (SMD) with B3LYP. The B3LYP-“SMD=water”-optimized structures were used for all calculations.....	129
S2.3 Chemical shielding and chemical shift of Li cation in cluster models. Both structure optimization with constraints and NMR calculations were performed in solvent of water, hexanol, and cyclohexane, respectively, using SMD solvent model and B3LYP functional.....	131
S2.4 ^7Li NMR chemical shift scan in the square model. B3LYP/6-31G(d,p)&SDD with water (SMD) as solvent.....	132
S2.5 ^7Li NMR chemical shift scan in the hexagon model. B3LYP/6-31G(d,p)&SDD with water (SMD) as solvent.....	133
S2.6 Li NMR chemical shift, Li position, and structure formation energies as a function of water molecules in square model. B3LYP/6-31G(d,p)&SDD with water (SMD) as solvent.....	134

LIST OF ABBREVIATIONS

POM	Polyoxometalate
NMR	Nuclear Magnetic Resonance
VT NMR	Variable Temperature Nuclear Magnetic Resonance
MAS	Magic Angle Spinning
CP/MAS	Cross-polarization Magic Angle Spinning
HETCOR	Heteronuclear Correlation
MOX	Mixed Oxide Fuel
SAXS	Small Angle X-ray Scattering
PDF	Pair Distribution Function
PDDF	Pair Distance Distribution Function
BVS	Bond Valance Sum
R _g	Radius of gyration
TMA	Tetramethylammonium
TBA	Tetrabutylammonium
TBP	Tributylphosphate
CTAB	Cetyltrimethylammonium Bromide
ICP-MS	Induced Coupled Plasma Mass Spectrometry
XRD	X-ray diffraction
TEM	Transition Electron Microscope
SEM	Scanning electron microscopy
TGA/DSC	Thermogravimetric Analysis/Differential Scanning Calorimetry
SIMFUEL	Simulated Spent Nuclear Fuel
UREX	Uranium Redox Extraction
PUREX	Plutonium Uranium Redox Extraction
TALSPEAK	Trivalent Actinide Lanthanide Separation with Phosphorus-Reagent Extraction from Aqueous Komplexes
UNEX	Universal Solvent Extraction

Chapter 1

Introduction to Uranium Chemistry

1.1 Uranium in the Nuclear Fuel Cycle

The nuclear fuel cycle is a string of processes for the generation of electricity by means of nuclear fission reactions. Uranium and thorium are the most common fuel sources found in nuclear reactors as they are both found naturally and have relatively stable isotopes, uranium being the most abundant and stable. Front end nuclear fuel cycle processes follows from mining and milling of the radioactive metals to conversion and enrichment to produce a fissionable mixed oxide (MOX) fuel source.¹⁻³ Fission of uranium-based fuels produces a large amount of energy and an assortment of metal oxides. Spent nuclear fuel is an element soup (**Table 1.1**) of uranium oxide, plutonium oxide, transition metal oxides (Zr, Mo, Sr, etc), rare earth oxides (La, Ce, Pr, etc), barium oxide and cesium oxide.³⁻⁵

Understanding chemistry of uranium has implications in the nuclear fuel cycle as back end spent fuel and legacy waste material speciation are directly affected by the chemical interaction between uranium, fission products, and naturally occurring metals in water. Backend extraction of uranium in the UREX/PUREX process⁶⁻⁹ works with spent mixed oxide fuel dissolved in concentrated nitric acid where uranium is extracted to a kerosene solution by tributylphosphate (TBP) coordination. Issues arise in acidic solution as most fission products readily dissolve, leading to more intricate separations from aqueous solution like TALSPEAK^{6,10,11} and UNEX.¹⁰ The combustion of uranyl complexed with TBP in kerosene produces UO_2 , toxic P_4O_{10} , and with other PO_x byproducts. Extraction of uranium using TBP requires multiple extraction cycles to acceptably separate out the uranium/plutonium from spent fuel. Principles of green chemistry would suggest that a different approach should be taken when extracting uranium to minimize processing steps, reagent quantities, and exposure to harsh acid solutions and airborne P_4O_{10} toxins. Alternative ligation has been studied extensively with alternative polydentate phosphate compounds to increase atom economy. Research included in this thesis (**Chapter 4**) explores an alternative pathway for uranium extraction beginning in mild base solutions and using ammonium-based surfactant molecules as extractant. This method

would minimize reagent quantities and hazardous exposure while increasing atom economy by extracting multiple uranium atoms at a time. **Figure 1.1** shows an early proposed extraction system in comparison to a simplified PUREX process model.



SIMFUEL composition	
Metal Oxide	Mass Percent (%)
Uranium dioxide (depleted)	95.2365%
Strontium oxide, SrO	0.1530%
Yttrium oxide, Y ₂ O ₃	0.0934%
Zirconium(IV) oxide, ZrO ₂	0.7270%
Molybdenum trioxide, MoO ₃	0.6758%
Ruthenium(IV) oxide, RuO ₄	0.4607%
Palladium(II) oxide, PdO	0.2727%
Tellurium(IV) oxide, TeO ₂	0.0992%
Cesium oxide, Cs ₂ O	0.4262%
Barium oxide, BaO	0.2835%
Lanthanum(III) oxide, La ₂ O ₃	0.2160%
Cerium(IV) oxide, CeO ₂	0.2246%
Praseodymium (III,IV) oxide, Pr ₂ O ₃	0.2028%
Neodymium (III) oxide, Nd ₂ O ₃	0.7218%
Gadolinium oxide, Gd ₂ O ₃	0.1416%
Europium oxide, Eu ₂ O ₃	0.0335%
Samarium oxide, Sm ₂ O ₃	0.0317%

Table 1.1 A representation of the metal oxide composition of fission products in spent nuclear fuel. This simulated spent fuel (SIMFUEL) is without plutonium and was used for experimentation throughout **Chapter 5**.

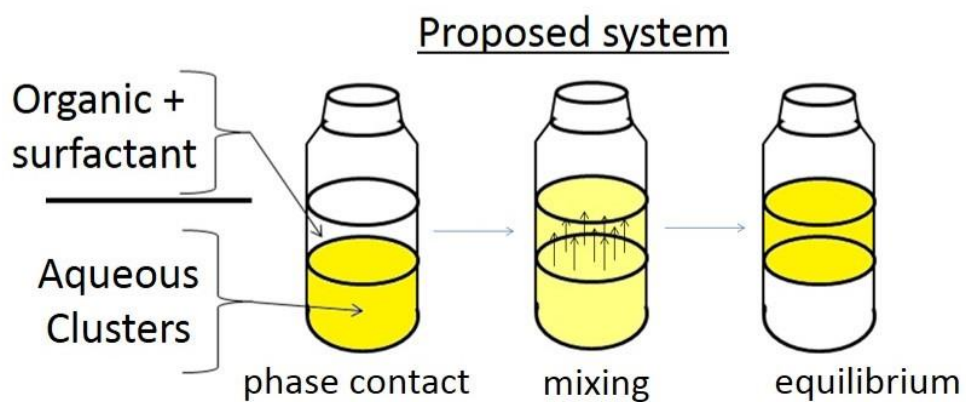


Figure 1.1 Schematic of a proposed extraction pathway that utilizes uranyl peroxide cluster species. The concept is to utilize of the charge of a cluster species (discussed in **Chapter 2.2**) to associate cationic surfactant extractant to a poly-uranyl molecule, increasing atom efficiency, minimizing exposure to harmful reagents compared to other extraction methods.¹²

1.2 Chemistry of Uranium

The intrigue of uranium is not limited to its nuclear properties, as the speciation and chemical reactivity of uranium is diverse and relatively understudied. Uranium can exhibit multiple oxidation states of III, IV, V and VI. The tetravalent and hexavalent oxidation states are naturally occurring. From a practical chemistry standpoint, the hexavalent oxidation of uranium is the most stable in air. Monitoring UO_2 over time, the U(IV) oxidizes to U(VI), going from a black powder to a brown/tan powder. In solution, U(VI) is not stable as a bare $6+$ ion, the speciation of U(VI) is exhibited by the uranyl ion (UO_2^{2+}) with linear multiply bonded oxygens (2-3 bond order from Bond Valence Sums (BVS) calculations). Orbital contributions in the bonding between oxygen and uranium atoms in the uranyl can only be theorized due to the unknown contributions from the f-orbital electrons.¹³ Relativistic effects arise when discussing f orbital bonding contribution as the electrons in the f orbitals are at a velocity approaching the speed of light.¹⁴ This anomaly is found in all heavy elements (periods ≥ 6) and affects oxidation state stabilization, electronegativity (uranium relatively high at 1.7), hydration energy, etc.

Uranyl ions can be found in a variety of coordination compound including uranyl nitrate [$\text{UO}_2(\text{NO}_3)_2$], uranyl carbonate [UO_2CO_3], uranyl triperoxide [$\text{UO}_2(\text{O}_2)_3^{4-}$], uranyl hydroxide [$\text{UO}_2(\text{OH}_2)$], etc. Utilized extensively throughout the nuclear fuel cycle is the solubility trends of uranium oxide and uranyl compounds, where most forms of uranium are soluble in acidic pH (HNO_3) and can be precipitated in alkaline pH (NH_4OH). This trend is broken with the presence of peroxide (generated naturally by the radiolysis of water)¹⁵ as the monomeric uranyl triperoxide is soluble in alkaline environments. Bulk uranyl peroxide or studtite [$(\text{UO}_2)_2\text{O}_2(\text{H}_2\text{O})_2$]¹⁶ is formed in acidic conditions for the nuclear fuel cycle. Studtite exhibits a one-dimensional channel structure, where the channels are uranyl-peroxo-uranyl linkages in a zigzag arrangement (discussed more in **Chapter 2.2**). This minute change in solution chemistry of uranium can have broad impact on the nuclear fuel cycle separations process, the handling of uranium legacy wastes, understanding of uranyl compound formation in solution, and foundational ion-ion interactions in solution chemistry.

Chapter 2

Introduction to Aqueous Clusters

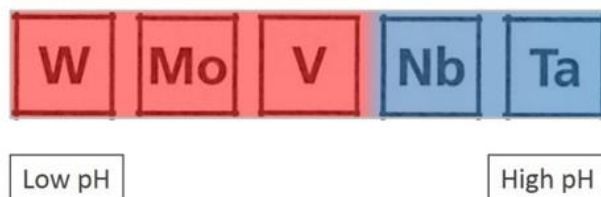
2.1 Cluster Chemistry of Transition Metals

Aqueous cluster chemistry has been studied for over a century. The term “cluster” traditionally refers to a nano sized grouping of metal atoms usually dispersed in an organic solution. In this work we are using the loosened definition for clusters including metal oxides and metal peroxo hydroxides, specifically the family of polyoxometalates (POMs), which are aqueous metal oxo cluster anions. Transition metal POMs (V, Nb, Ta, Mo, and W) have a wide range of molecular structures, the most common being Lindqvist ion and Keggin ion structures.^{17,18}

The Lindqvist ion structure is that of a superoctahedron containing six equivalent edge sharing octahedra with a molecular formula of $[M_6O_{19}]^{n-}$. The α -Keggin ion is a grouping of four edge sharing trimer units linked via corner sharing about a central hetero atom, molecular formula $[XM_{12}O_{40}]^{n-}$. Isomerization in the Keggin structure occurs by rotation of a trimer unit giving way to five possible isomers (α -, β -, γ -, δ -, and ϵ -).

Effect of pH on transition metal POMs

Solubility:



Reactions (acid – bottom up approach, base – top down approach)



Figure 2.1 Transition Metal POMs from Group V & VI form clusters in different environments and in different pathways. Group VI Metals and vanadium form clusters in acidic solution from monomeric units, as the corresponding MO_6^{x-} ions are stable. Niobium and tantalum form clusters in alkaline solution from the bulk M_2O_5 solid, as the monomeric ions are not stable for these metals.

Complexity of POM structures is multiplied when well-known structures like the Keggin ion are missing one or more octahedra units (lacunary) or have one or more extra octahedra capping the exterior structure. Literature has shown applications for various POMs as water oxidation catalysts,¹⁹ thin film precursors,¹³ and protein crystallization agents.²⁰ Under closer examination, the monomeric building unit for transition metal POMs, MO_6 (**Figure S1.1**) is possible due to the phenomenon known as the metal oxo wall. The metal oxo wall is a theoretical barrier in the transition metals within the periodic table, it denotes which metals form stable multiply bonded “yl” oxygens.²¹ Early d0 transition metals (V^{5+} , Nb^{5+} , Ta^{5+} , Mo^{6+} , W^{6+} , etc.) form stable “yl” oxygen bonds, structurally passivating a position on the octahedra in a monomeric MO_6 unit. Bonding of the “yl” oxygen is between the empty d orbitals of the metal and the 2p orbitals of the oxide. Passivation of a single dimension on the octahedra inhibits bulk oxide formation while allowing for monomer units to undergo directed hydrolysis and condensation reactions with the other oxo ligands about the transition metal, forming spherical shaped clusters (**Figure 1.2**).

2.2 Uranyl Clusters

In comparison to transition metals, some early actinides are also able to form stable “yl” oxygens. As discussed above, uranium can form 2 stable “yl” oxygens in a linear orientation (axial). Passivation in the case of the uranyl further directs additional ligation (preferentially bidentate) to occur only in the equatorial plane about the metal. Cluster formation with stable “yl” oxygens in the two axial positions stabilizes the formation of hollow sphere and crown structures (**Figure 2.2**). Common uranyl structures are seen in nature within minerals, an example being the uranyl peroxide mineral, studtite (**Figure 2.3**).²²

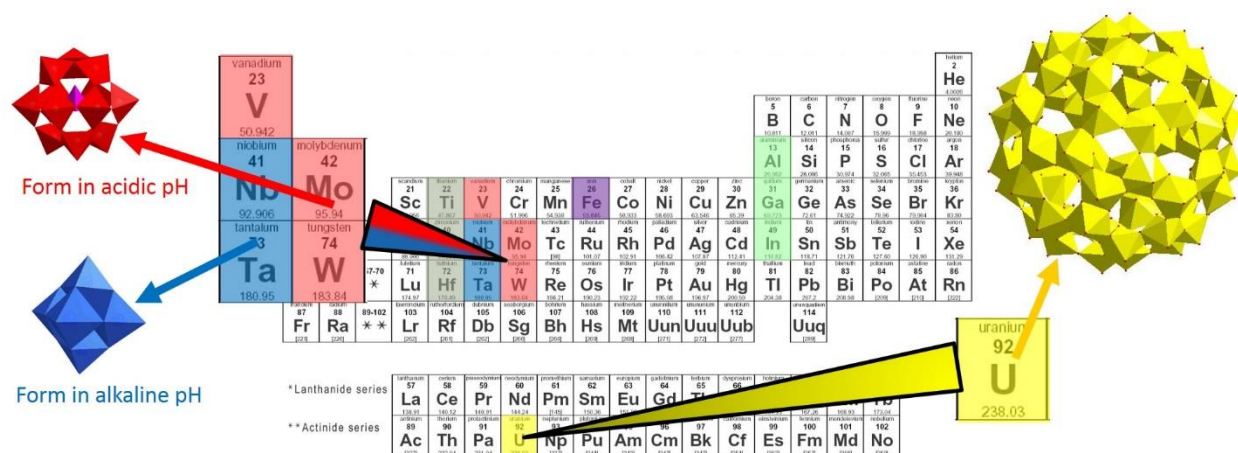


Figure 2.2 Clusters can be found across the periodic table, from classic POMs of the Group V & VI,^{17,18} to more recent discoveries of metal peroxide rings of Group IV metals,²³ iron Keggin ions capped with bismuth,²⁴ and polyoxocations found with semimetals in Group XIII.²⁵ Within the last decade, unique clusters of uranium and actinide metals have been discovered²⁶ which is the focus of this work.

Studtite is a material with one dimensional channels of uranyl triperoxide linkages. The channels have a zig-zag morphology due to the bent angle of the peroxide bridges. Adding excess base to the studtite breaks down the peroxide linkages to yield monomeric uranyl triperoxide and over time, self-assembles into a family of uranyl peroxide clusters (recently discovered in 2005).²⁶ Uranyl peroxide clusters are hollow cage clusters made up of uranyl-peroxo-uranyl and uranyl-hydroxo-uranyl bridges. The bent nature of these peroxo and hydroxo bridges is what gives yields the zig-zag structure of studtite and the spherical cluster geometry. These anionic clusters hold high overall negative charges balanced out by counterions on the interior and exterior of the capsule structures. Cluster charges can seem staggering to most chemists, but the charge per uranium center is lower in the cluster than in the uranyl triperoxide monomer.²⁷ Relegation of charge is a major driving force behind spontaneous cluster self-assembly. Early literature²⁸ of uranyl peroxide clusters describe a one pot synthesis, combining uranyl nitrate, hydrogen peroxide, and alkali hydroxide at the same time, bypassing the bulk studtite, then allowing the self-assembly of clusters to occur.

Crystals from one pot reactions can take days, weeks or sometimes months to form and the purity/quality is difficult to control. More recent developments to the synthesis²⁹ have added an ethanol precipitation/wash step to isolate monomeric uranyl triperoxide. Precipitation removes excess peroxide and base from the reaction and allows for more pH control. The precipitated uranyl monomer is dissolved in water and a Cu^{2+} catalyst is introduced to speed up the cluster self-assembly reaction. The synthesis seems relatively simple, but the slightest deviation can dictate cluster formation, cluster identity, purity, and crystallization time. Changing the identity of the base species, i.e. LiOH , NaOH , KOH , NH_4OH , etc. in the one pot synthesis directly affects the cluster type crystallized. Throughout this thesis, the clusters of uranyl peroxide are referred to as a “family” as there are over sixty structures of uranyl peroxide clusters published and over a hundred more known but not yet properly characterized or reproducible.²⁷ Changing the identity of counterions is a simple method of cluster diversity, but many studies have been done using mixtures of counterions, different alkaline buffers, and transition metal ions for mixed metal clusters.²⁷ Uranyl can have stable bonds to other bidentate ligands beyond peroxide. Oxalate and pyrophosphate cluster compounds have been found in a range of acidic pH, meaning that there are stable uranyl cluster species across the pH scale.^{30,31}

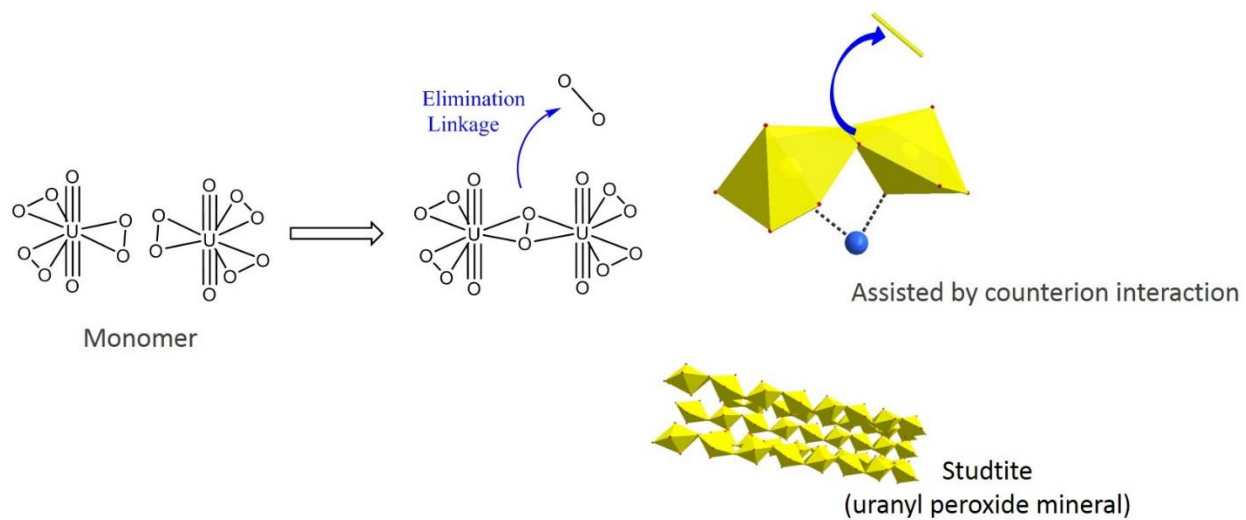


Figure 2.3 Linkages between uranyl triperoxide monomers is shown, leading to uranyl-peroxo-uranyl bridge formation. Previous research has been done to show that catalysis assists with cluster self-assembly²⁹ and counterions (blue) template monomeric interactions.³² Similar linkages are found in the studtite mineral.

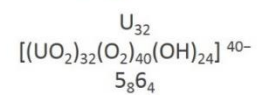
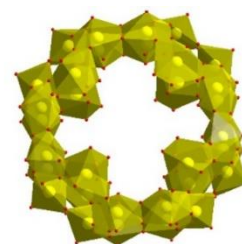
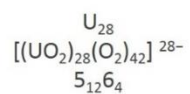
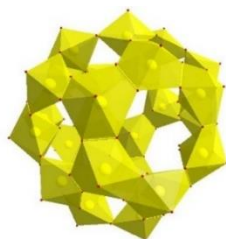
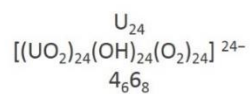
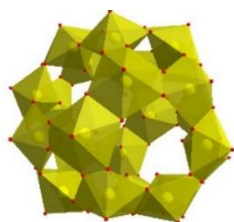
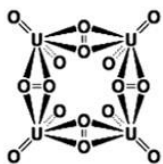


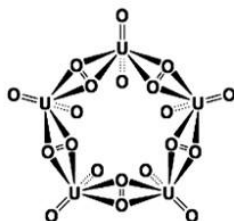
Figure 2.4 Above are specific cluster structures explored in this thesis work including the conventional name, anionic formula and the number of square, pentagonal and hexagonal faces found in the structure.

Tetramer



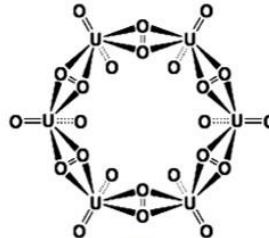
S

Pentamer



P

Hexamer



H

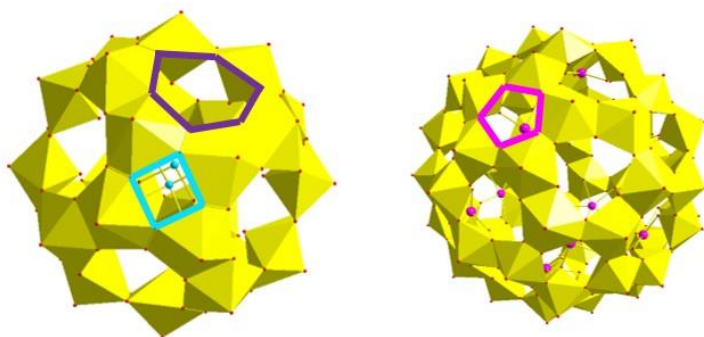


Figure 2.5 Oligomer ring structures are shown above. Uranyl peroxide clusters morphology contains these open rings as facets on the cluster exterior.

Discussed in this thesis are three specific alkaline clusters with structures provided in **Figure 2.4**. Conventionally, uranyl clusters are named by how many uranium atoms are found in the structure, i.e. U_{24} is the cluster (left) containing 24 uranyl centers bridged by peroxide. Occasionally including the counterion is required to better specify the cluster species (like LiU_{24} , $CTAU_{24}$, or KU_{28}). **Figure 2.4** includes the chemical formula for each cluster anion and a convention denoting the number of square, pentagonal and hexagonal open faces in the structure.²⁷ Crystal structure of each cluster is a hollow crown or capsule shape.²⁷ As described previously, most uranyl clusters can be broken down to collections of tetramer, pentamer, and/or hexamer crown units (**Figure 2.5**). These oligomer units are ring shapes that combine to make the open faces on the cluster structure. The convention for describing the faces is used, as the entire three-dimensional structure is difficult to capture in a still image. In the case of U_{24} the notation 4_66_8 means that there are six total tetramer faces (4_6) and eight total hexamer faces (6_8).

It has been shown by experimental and computational studies that the various alkali ions template specific oligomeric face unit.³³ For example, Li^+ preferentially templates the uranyl tetramer unit, leading to formation of clusters containing square face morphology whereas K^+ templates the uranyl pentamer unit, forming a different cluster species than with Li^+ . The templating effect of counterions influences the mechanism by which uranyl peroxide clusters self-assemble. Unlike transition metal POMs, uranyl peroxo cluster formation is not straight forward monomer to cluster assembly. Mechanisms have been suggested that follow a bottom-up (from monomer/oligomer uranyl triperoxide to cluster) synthesis like the one-pot synthesis, a top-down approach (from studtite mineral to cluster) using base titration methods for rapid cluster assembly.³⁴ It has also been experienced that over time clusters transition from one species to another (U_{28} decomposes/converts to U_{24}). As synthetic pathways are developed and expanded upon, the mechanism may be as complicated as the cluster capsule structures and ion association plays a major role. Understanding how counterions associate to uranyl clusters also gives insight into basic scientific understanding of ions in solution.

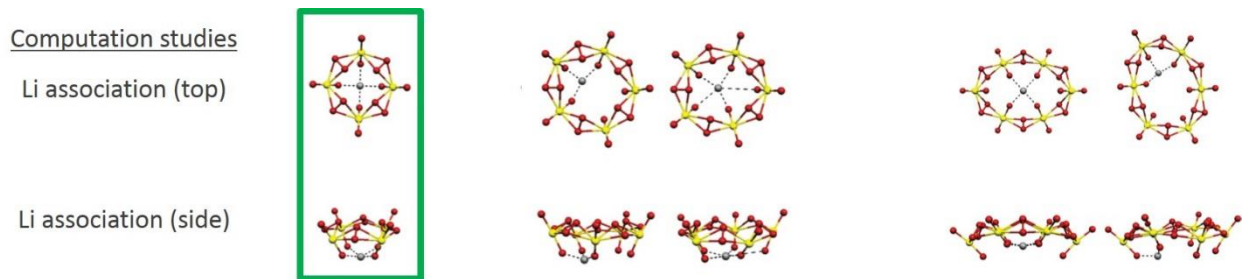


Figure 2.6 Templating effects come from counterions introduced in the synthesis pathway of uranyl peroxide clusters. Computation suggests that these counterions preferentially template specific oligomeric uranyl structures. Featured above are the suggested templating positions in different oligomer rings by a Li^+ ion.

Chapter 3

Introduction to Characterization Techniques

3.1 Small Angle X-ray Scattering Introduction

Small angle X-ray scattering (SAXS) is a characterization technique used to examine structural information of particles in solution. Primarily, SAXS is employed to study biomolecular structures, colloid systems, and sometimes solid samples.³⁵ In this thesis, SAXS is utilized in a unique way to characterize inorganic nano clusters in solution, the description of instrumentation is from this perspective. SAXS measurements are done by timed exposure of a solution sample with a collimated X-ray source. Bench-top SAXS instruments, like the one employed throughout this thesis, use either a Cu or Mo source depending on the sample scattering and experiment; Cu is suitable for strongly scattering uranium samples.

As the X-rays interact with the sample, a fraction of the radiation will be scattered by the particles in the sample. The scattering profile is collected on a detector. Instrumentation discussed in this thesis work were done using an image plate detector. Image plates are reusable film-like strips that collect two-dimensional X-ray scattering intensity from the irradiated sample. After a SAXS exposure, scattering data is scanned into a computer program for data processing. See **Figure 3.1** for an overview of SAXS data collection.

When processing SAXS data, the raw scattering profile (rainbow image in **Figure 3.1**) is transformed to a one-dimensional slice representation (red line in **Figure 3.1**). Scattering data is commonly plotted as the Log of the scattering intensity ($I(q)$) versus the Log of the scattering vector (q), where $d_{Bragg} = \frac{2\pi}{q_{Peak}}$.³⁶ Other processing is done such as primary beam referencing, background subtraction, scaling, desmearing process, and a smoothing process.³⁷

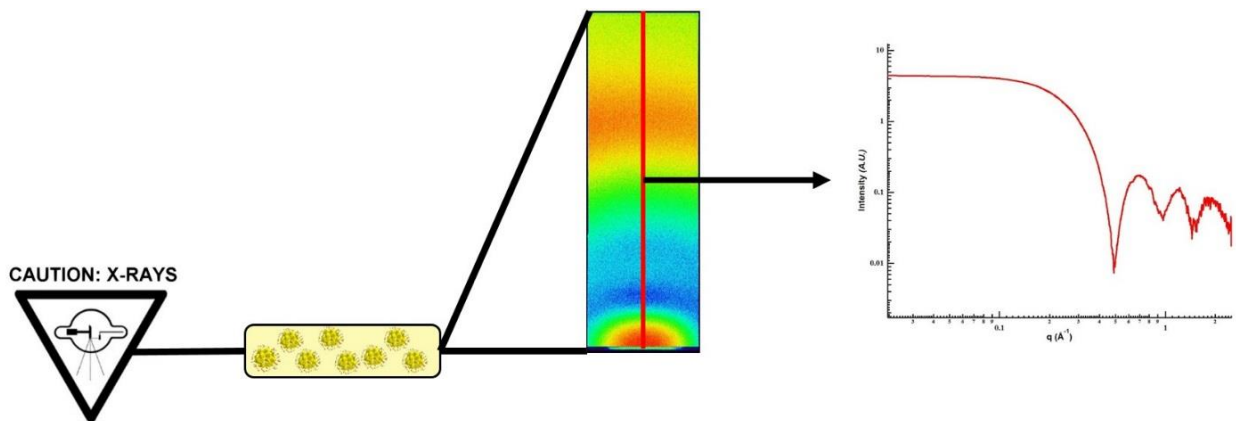


Figure 3.1 A SAXS instrumentation cartoon describing the data collection process. A collimated X-ray beam interacts with the particles in a solution sample to create a scattering profile. The scattering data is collected on an image plate detector.

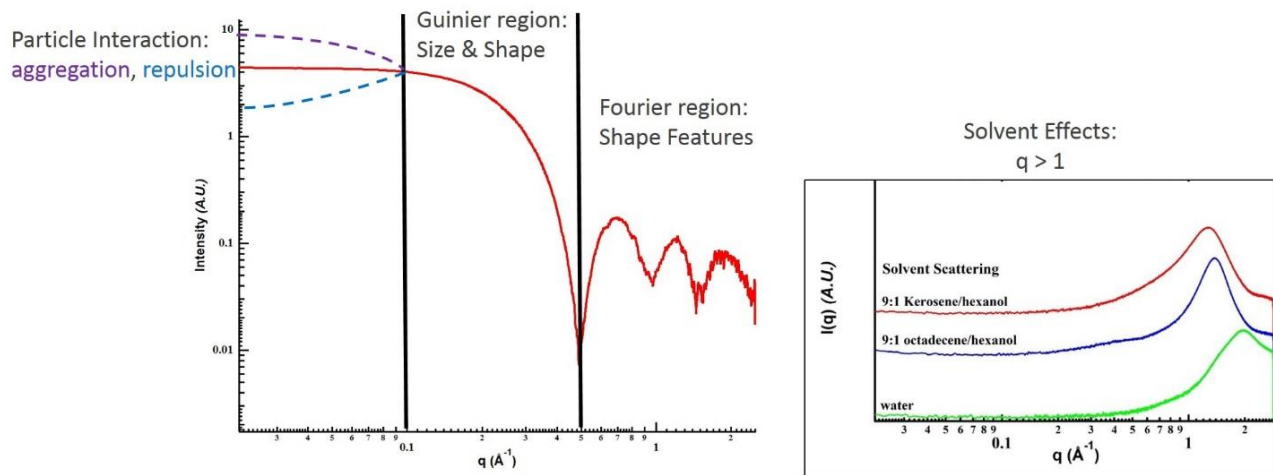


Figure 3.2 Qualitative analysis of SAXS data from uranyl peroxide clusters.

After data processing, the scattering curves are ready for analysis. Important initial information about a sample can be gained from qualitative analysis of the SAXS curve. **Figure 3.2** shows a breakdown of important regions on a SAXS curve and the specific information that can be gained from each region. While interpreting a SAXS curve, it is important to note that the lower the q value, the larger the species. At low q , information on interparticle interactions like aggregation or repulsions is shown. The Guinier region shows size and shape information. Qualitatively, multiple scattering curve Guinier regions must be compared for relative size information, accurate numerical sizes requires quantitative modeling. The Fourier region is where fine shape information and solvent molecules are seen. Different solvent molecules have different scattering profiles and affect the overall particle scattering in different ways. The inhouse instrument used for all data collection shown has a wide-angle attachment, allowing for a larger q region and thus shows smaller particles.

Quantitative modeling of SAXS data is done using Irena software³⁸ within Igor Pro. The Irena package contains modeling tools that vary in complexity and constraint optimization options. Pair Distance Distribution Function (PDDF) and Modelling II are the main modeling tools used for analysis of uranyl cluster SAXS data.^{35,38} PDDF analysis (**Figure 3.3**) gives information on the shape of particles in solution, for the uranyl clusters, the PDDF profile matches with the classic core/shell shape as expected. Radius of gyration (R_g), modeled by PDDF, is a shape independent measure of the size of particles in the solution from the particle center of mass.³⁵ For spherical particles of homogeneous density, the R_g value can be extrapolated to particle radius by using the equation $R = \sqrt{5/3}R_g$. The R_g value alone is not enough for an accurate determination of particle size for core/shell uranyl clusters, which is why Modelling II is utilized. Analysis with Modelling II has the most constraint controls, allowing for the most complete optimization of shape dependent size determination. For uranyl clusters, the core-shell model fit in Modelling II optimizes heterogeneous densities compared to solvent density and thickness of the shell.³⁸

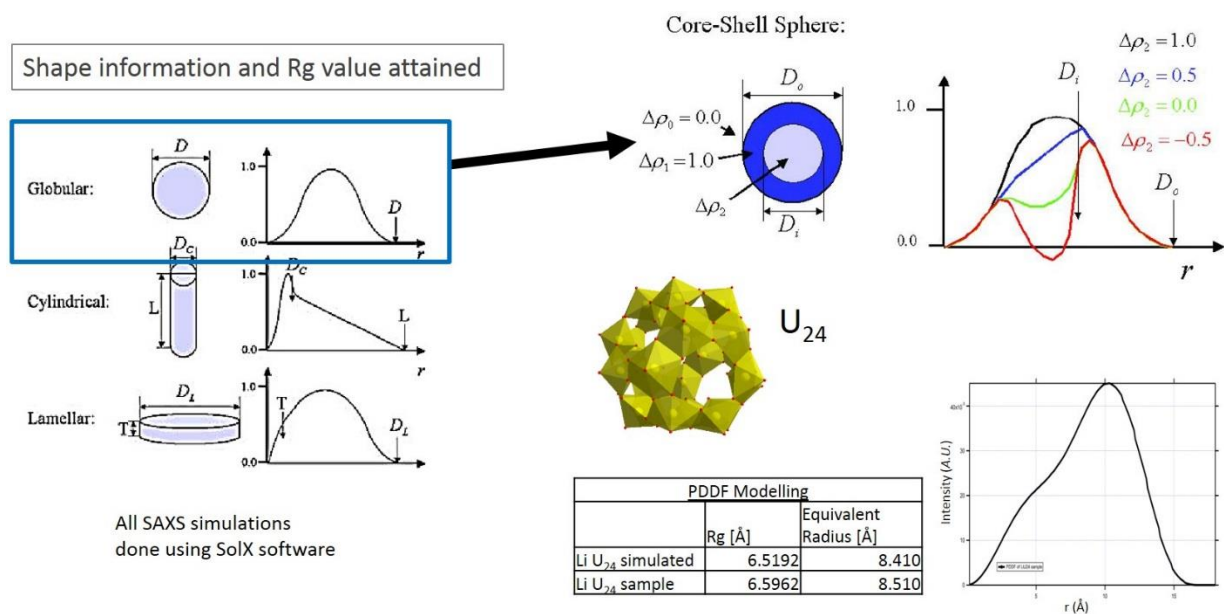


Figure 3.3 Pair Distance Distribution Function (PDDF) modelling of SAXS data from the uranyl peroxide cluster species U_{24} . The cluster shape matches with the expected core-shell shape and the Rg value for particle size determination matches with that of a simulated SAXS curve of U_{24} .

3.2 Nuclear Magnetic Resonance Introduction

Nuclear Magnetic Resonance (NMR) spectroscopy is a characterization technique comparable to infrared or UV-vis spectroscopy, where electromagnetic radiation interacts with a sample. In the case of NMR, radiation in the radio-frequency region is absorbed by the nucleus. Absorption is a function of the nuclear environment of atoms in a sample.

Nuclei, like electrons have a spin state. Spin of the nucleus creates a magnetic moment. In an NMR experiment, a sample is placed in an external magnetic field which aligns the magnetic moments (z-axis by convention) so that two spin states dominate ($\pm\frac{1}{2}$, for spin $\frac{1}{2}$ nuclei) as opposed to indistinguishable spin energy states.³⁹ With two distinct energy states isolated, radiofrequency radiation is introduced to transition nuclei between energy states. This excitation “knocks” the magnetic moments out of alignment with the external magnetic field (xy-plane by convention). After excitation by the radiation pulse, nuclei can relax back to ground state, emit the energy absorbed and realign with the magnetic field. Relaxation occurs as two major components. Spin-lattice (T_1) relaxation is described as the rate the excited state nuclear spin transfers energy to the neighboring molecules (z-axis relaxation).⁴⁰ Spin-spin relaxation (T_2) is a measure of decay rate in the xy-plane. Immediately following excitation, the nuclear spins are aligned in the xy-plane. Over time the spins are desynchronized and propagated within the xy-plane due to interactions between spins.⁴⁰ T_2 relaxation is usually the faster process and thus the limiting contribution to NMR signal duration.⁴¹ Detection of the free induction decay (FID) is a measure of the combination of all decay emissions in a sample. The FID is a time domain measurement. Processing with a Fourier transformation converts the FID to a frequency domain (or ppm of the base resonance frequency). Peak position and shifting, known as chemical shift, is a function of the nuclear environment. Interactions of magnetic fields from neighboring atom electrons shield the nucleus from the primary external field, relaying information about what atoms are adjacent to the nucleus in question.³⁹ Adjustments to the radio frequency pulse sequence can be taken advantage of to provide more information about the chemical environments of nuclei.

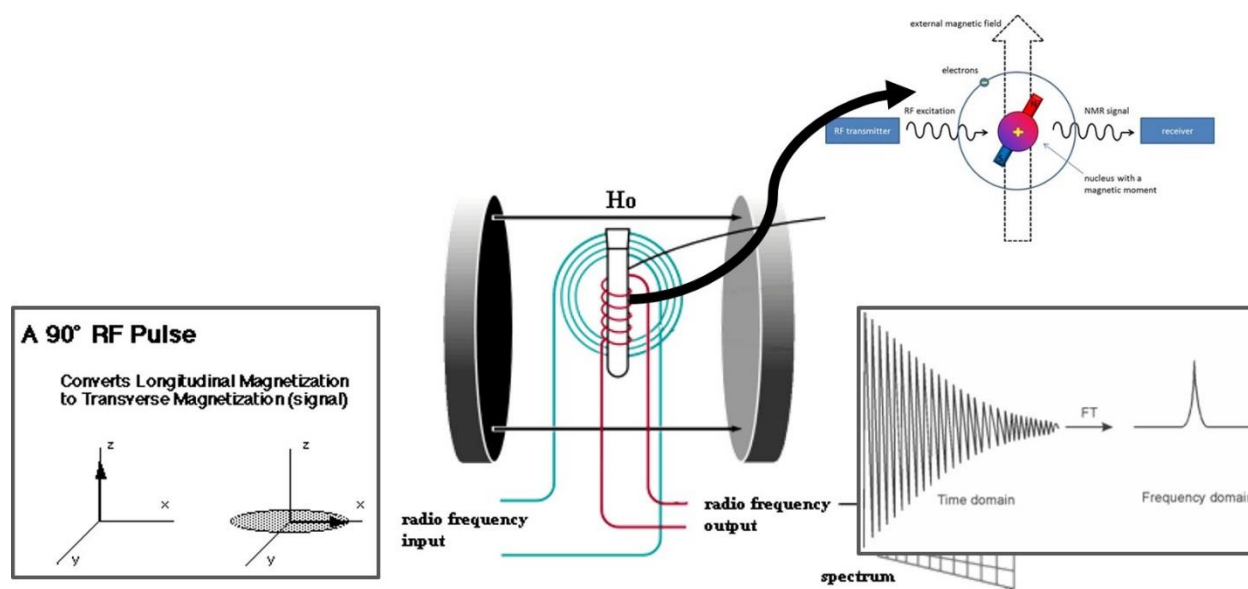


Figure 3.4 A schematic cartoon of an NMR experiment. The sample is placed into a magnetic field (center) that aligns all nuclear spins (top right). Irradiation occurs with radio frequencies specific to the nuclei in question (left), converting spin states to the xy-plane. An inductive precession of an ensemble is observed as the nuclear spins relax back to alignment with the magnetic field, producing a time domain FID (right). The FID undergoes a Fourier transform to the frequency domain (right).

In this thesis work, Solid-state magic angle spinning (MAS), solid-state cross-polarization magic angle spinning (CP/MAS), variable temperature (VT) NMR and heteronuclear correlation 2-D NMR are specific NMR techniques utilized. Magic angle spinning is a technique used in solid-state NMR experiments to reduce line broadening and increase resolution of signal from the solid. MAS dampens dipolar, chemical shift anisotropy, and quadrupolar interactions that are prevalent in solid samples. This is done by spinning the solid sample at kHz frequencies at the “magic angle” (θ_m where $\cos^2 \theta_m = \frac{1}{3}$) with respect to the external magnetic field.^{42,43} Cross polarization (CP) during solid-state MAS enhances the signal from weakly coupled nuclei.⁴⁴ Variable temperature (VT) NMR experiments give information of the exchange dynamics in a system.^{45,46} When the temperature of the sample is increased, nuclei that exchange between two chemical environments tend to broaden and eventually coalesce to a single chemical environment. Simulations can yield rates of exchange and via data analysis, energy of exchange from an Eyring plot.⁴⁵ Heteronuclear correlation experiments (HETCOR) is a 2D NMR pulse sequence that correlates a nucleus in question (in **Chapter 5**, ^7Li) to directly coordinated protons (^1H).⁴⁰ Unlike in common 2D experiments like COSY, there is no diagonal or symmetry in the data output.

NMR spectroscopy is primarily used for structural determination of organic molecules by observation of the ^1H and ^{13}C spectra. Many other nuclei like ^{19}F , ^{31}P , ^{29}Si , etc. are NMR active and contribute extensively to understanding of inorganic materials. In this thesis, ^7Li NMR is utilized to determine the association of lithium ions in uranyl peroxide cluster structures, as lithium is too small for detection with x-ray diffraction. Lithium has two NMR active nuclei but ^6Li (spin = 1) is not suitable for the studies performed in this work as it is less sensitive than ^7Li and has low natural abundance at 7.59%. Major differences between ^7Li and conventional ^1H NMR are: the spin of each nucleus (^7Li spin = 3/2; ^1H spin = 1/2), the NMR frequency for ^7Li is 194.317 (referenced to a 500 MHz instrument), and the 90-degree pulse is not standard which requires measurement.

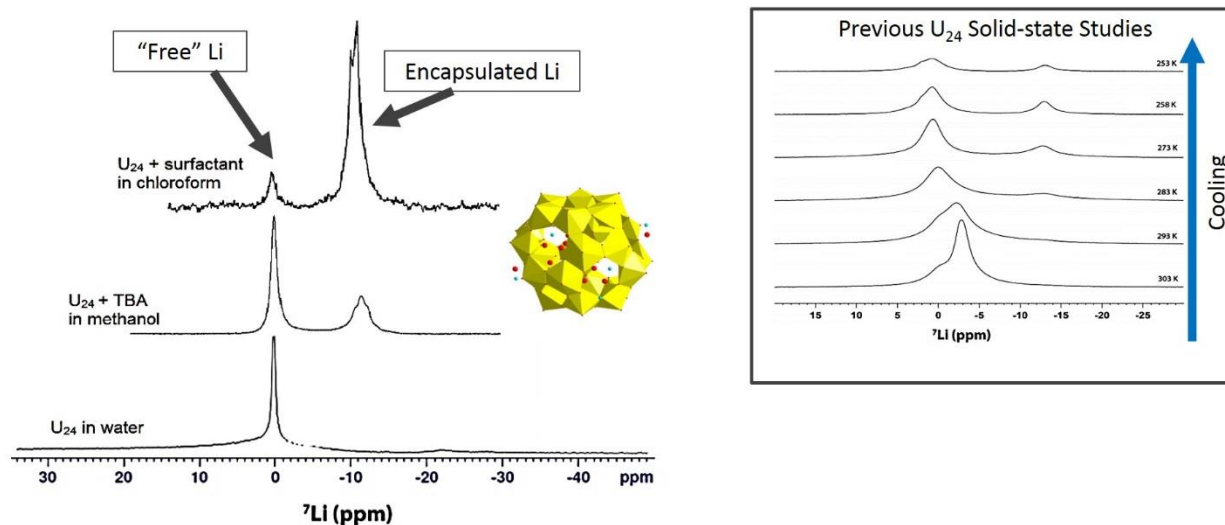


Figure 3.5 Literature studies showing variable temperature solid-state ^7Li NMR of LiU_{24} cluster crystals (right). Encapsulated Li environments are only distinguishable at low temperatures. Included are preliminary solution NMR data on hybrid U_{24} clusters in organic solvents (left). Encapsulated peaks are sharp and higher resolution details can be observed such as multiple encapsulated environments.

Aqueous lithium ions are referenced to 0 ppm, and are the only signal observed with the aqueous U₂₄ sample (Figure 3.5). Solid state NMR studies in the literature show a separation of ⁷Li chemical shifts association with the clusters (-14 ppm) and the lattice lithium (0 ppm) at low temperatures. This means that even in the solid state at ambient temperature, the lattice and encapsulated Li species are exchanging too rapidly to differentiate. Hybrid organic/cluster species in organic solvents should isolate the encapsulated Li and amplify the peaks associated with the cluster environment as there is minimal Li in the surrounding solution (**Figure 3.5**). Isolating Li environments to the cluster interior should reveal number of Li chemical environments and thus the coordination of Li.

Chapter 4

Benchmarking Uranyl Peroxide Capsule Chemistry in Organic Media

Harrison A. Neal, Jennifer Szymanowski, Jeremy B. Fein, Peter C. Burns, and May Nyman

Eur. J. Inorg. Chem. **2017**, 1(17), Page 39

DOI: 10.1002/ejic.201601219

4.1 Abstract

Uranyl peroxide capsules are a recent addition to polyoxometalate (POM) chemistry. Ten years of development has ensued only in water, while transition metal POMs are commonly exploited in aqueous and organic media, controlled by counterion or ligation to render the cluster hydrophilic or hydrophobic. This contribution demonstrates uranyl POM chemistry in organic media. Here, new uranyl POM behavior is recognized in organic media including 1) stabilization and immobilization of encapsulated hydrophilic counteranions, identified by Li nuclear magnetic resonance, 2) formation of new cluster species upon phase transfer, 3) extraction of uranyl clusters from different starting materials including simulated spent nuclear fuel, 4) selective phase transfer of one cluster type from a mixture, and 5) phase transfer of clusters from both acidic and alkaline media. The capsule morphology of the uranyl POMs renders accurate characterization by X-ray scattering, including the distinction of geometrically similar clusters. Compositional analysis of the aqueous phase post extraction provided a quantitative determination of the ion exchange process that enables transfer of the clusters into the organic phase. Preferential partitioning of uranyl POMs into organic media presents new frontiers including the metal ion behavior and chemical reactions in the confined space of the cluster capsules in hydrophobic media; and reactivity of clusters at the organic-aqueous interface.

4.2 Introduction

Nuclear energy, a viable carbon-free alternative to fossil fuels, contributes nearly 11% of global energy sources.¹ Ideally, the closed nuclear fuel cycle consists of mining, enrichment, and fuel fabrication, prior to use of the fuel. Post fuel-use involves the recovery of usable spent fuel isotopes, and finally safe encapsulation and storage of radioactive components that cannot be repurposed (i.e. radioactive Cs and Sr). Uranium is the major fuel isotope for most nuclear reactors; and throughout the nuclear fuel life cycle, a variety of chemical systems are exploited for separations. These include vapor phase transport as fluoride complexes, acid dissolution for mining and reprocessing, and extraction into organic media by complexation.^{2,3} Devising new forms and speciation of uranium in both the solution and solid state are of interest for developing and optimizing separation chemistries for current and future anticipated needs. These include separations for the nuclear fuel cycle, for legacy waste treatment and for cleanup of environmental contamination.

A unique form of uranium is the anionic uranyl peroxide capsules discovered in 2005.⁴ Similar to the mineral studtite in both the bridging peroxide ligands and the inherently bent dihedral angle of U-(O-O)-U; uranium polyoxometalates (POM) feature uranyl hexagonal bipyramids that are bridged by peroxide ligands. The two passivating axial 'yl' oxygens of the UO₂ lead to the unique hollow capsule topology. There are over 38 cluster assemblies,⁵ and new topologies are still being discovered. Studies of cluster self-assembly has shown that in alkaline conditions uranyl polyhedra are bridged with peroxo ligands, and oftentimes peroxo plus hydroxyl⁶ ligands. It has also been shown that in more acidic conditions, these capsules form with oxalate or pyrophosphate bridges.⁵ Mechanisms for cluster formation are not yet fully understood, but both 'bottom-up' cluster assembly (monomeric uranyl to cluster),^{7,8} and top-down assembly (studtite mineral to cluster) have been amply demonstrated,⁹ or even an evolutionary approach (formation of a kinetically favored cluster topology followed by slow conversion into a different topology).^{9,10} Here we also investigated cluster self-assembly in tandem with oxidation of U(IV) to U(VI). These studies are of fundamental interest because the peroxide serves as both an oxidant¹¹ and cluster component. Nonetheless, the counteraction, reaction time, and pH certainly affect formation and stabilization of cluster geometries.⁵

Extensive studies of the aqueous behavior of the uranyl capsules have included formation kinetics and mechanisms,^{7,9,12} templating by alkalis and oxoanions,^{13,14} supramolecular

assembly,¹⁵ and exchange of alkalis between the capsules and solution. Meanwhile, studies outside of aqueous media have not yet been addressed. On the other hand, ligation, hydrophobic counterion exchange, and surfactant encapsulation of transition metal POMs have allowed transfer of these clusters into organic solvents,^{16–20} followed by many studies in non-aqueous media. Most recently, surfactant-POMs arrays have been exploited for ionic liquids,²¹ supramolecular assembly to create hydrophobic reaction vesicles,²² functional surface coatings,²³ formation of nanoparticle-POM hybrid materials,^{24,25} and biocompatibility.²⁶ Additionally, coordination of transuranic metals to POMs followed by transfer into organic media has been demonstrated.²⁷ Selective solvent extraction of metal complexes has likewise been developed and exploited for industrial applications including metal recovery and waste stream decontamination.^{28–30}

Here, we show that uranyl peroxide capsules are readily isolated as surfactant salts, or directly extracted into organic media with dissolved cationic surfactants. We have demonstrated liquid phase transfer with two alkaline phase clusters: an ammonium salt of $[(\text{UO}_2)_{32}(\text{O}_2)_{40}(\text{OH})_{24}]^{40-}$ (**U₃₂**) that assembles instantaneously,³¹ and a lithium salt of $[\text{UO}_2(\text{O}_2)(\text{OH})]_{24}^{24-}$ (**U₂₄**). The former allowed demonstration of assembly followed by rapid solvent extraction, while the latter provided an opportunity to probe the behavior of the encapsulated species using ⁷Li nuclear magnetic resonance (NMR) spectroscopy. With the combination of small-angle X-ray scattering (SAXS) and compositional analysis of the solution phase, we can estimate the number of surfactant molecules required to extract a single cluster and it agrees well with analogous transition metal POM systems and demonstrates the importance of the encapsulated species in the extraction process. In the hydrophobic medium, the encapsulated species exhibit much different behavior than in aqueous solution and even the solid state, and this inspires future investigations of reactions in confined spaces. We have also demonstrated cluster assembly from UO₂ starting material (along with other metal impurities that are found in spent nuclear fuel) that involves simultaneous oxidation and self-assembly and realized 1) the metal impurities are largely left in the aqueous phase, 2) the different cluster formation pathway leads to different cluster species, and 3) the organic phase selectively extracts one cluster type. Finally, extraction of aqueous acidic clusters was also demonstrated, and formation of larger cluster forms upon phase transfer was recognized under certain conditions.

4.3 Results and Discussion

Quantification of ion-exchange upon phase transfer. Initially, aqueous solutions of Li-U₂₄^{32,7} and NH₄-U₃₂³¹ were prepared. Comparison of the X-ray scattering curves to those simulated from the solid-state structures³³ show excellent agreement out to three oscillations, indicating absolute monodispersity (**Figure 4.1**). The distinct oscillations arise from the core-shell structure,³⁴ and both the simulated and experimental data were fit with core-shell parameters (**Table S4.1**).³⁵ Small differences in intensity in the oscillatory region ($q > 0.4 \text{ \AA}^{-1}$) arises from solvent scattering effects that are dominant in this region. Nonetheless, this detail of agreement between the experimental and theoretical scattering curves is unprecedented in systems of small, discrete clusters. The organic solutions were prepared (**Table S4.2**) by suspending cetyltrimethylammonium bromide (CTAB) in a mixture of kerosene and hexanol. The organic solutions were introduced to aqueous Li-U₂₄ and NH₄-U₃₂ by shaking, transfer of the uranyl clusters from the lower aqueous layer to the upper organic layer was visible by the distinct yellow color (**Figure 4.2**). SAXS analysis of the organic phase was utilized to confirm the persistence of clusters in organic media. We systematically varied the ratio of surfactant concentration to cluster concentration. In the case of NH₄U₃₂, cluster concentration was varied while keeping the surfactant concentration constant (**Figure 4.2a**). In the case of LiU₂₄, surfactant concentration is varied while keeping the cluster concentration constant (**Figure 2.2b**), this is due to the synthetic control required to form LiU₂₄ optimized at a specific uranium concentration. However, both approaches provided a bracketed range of surfactant:cluster ratios (**Table S4.2**) to determine the optimal ratio for complete phase transfer. The two series produced similar trends in the scattering data and transfer efficacy, helping to elucidate the role and behavior of the encapsulated counterions in the phase transfer process.

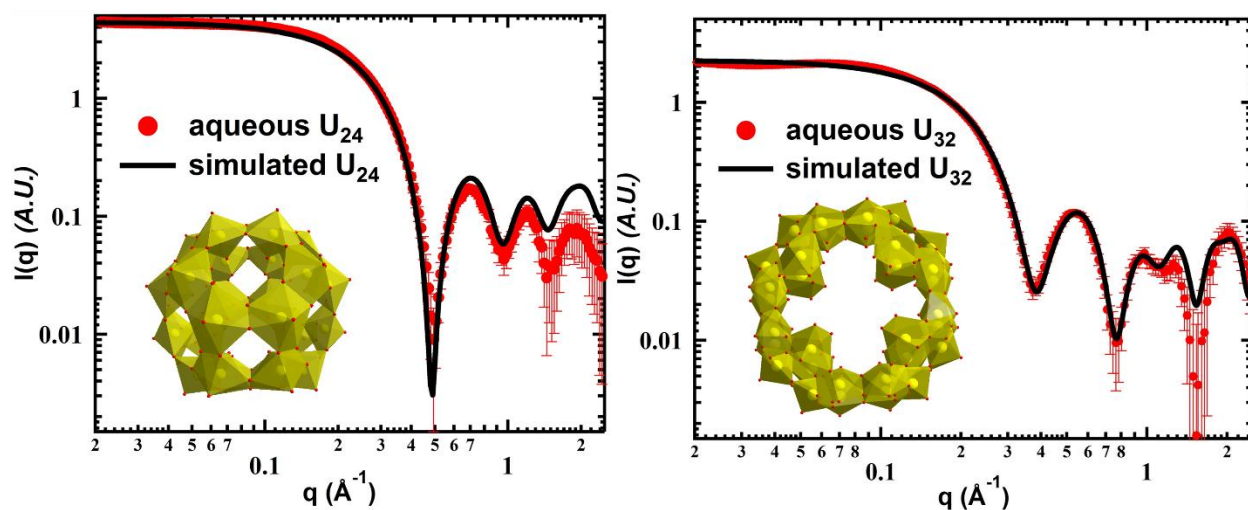


Figure 4.1 Comparing simulated and experimental SAXS data for aqueous uranyl peroxide clusters. Li- U_{24} (left) and NH_4 - U_{32} (right): In cluster representations, yellow polyhedra are $UO_2(O_2)_3$ and $UO_2(O_2)_2(OH)_2$

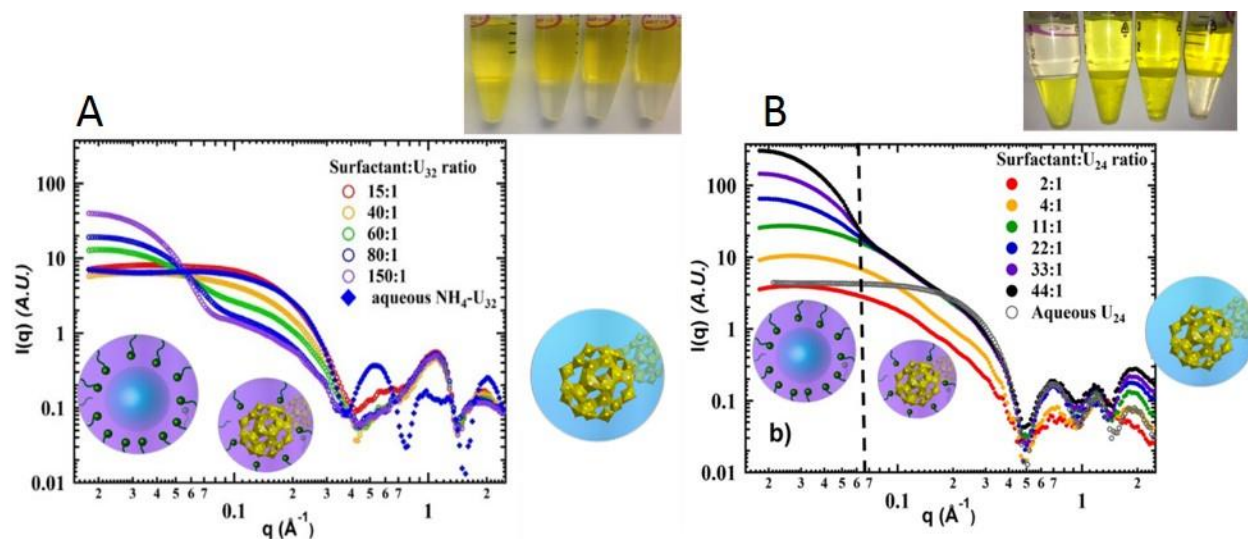


Figure 4.2 Extraction of uranyl peroxide clusters into the nonaqueous phase. (a) X-ray scattering data of U_{32} extracted into kerosene with constant surfactant concentration (0.075 M) and variable uranium concentration (0.021-0.165 M aq. solution). Also shown is U_{32} extracted from a 0.7 M NH_4-U_{32} aqueous solution with tetramethylammonium (TMA) hydroxide added for improved solubility. (black triangles). (b) X-ray scattering data of U_{24} extracted into octadecene with constant uranium concentration (0.165 M aq. solution) and variable surfactant concentration. Photo of transfer of U_{24} from the lower aqueous phase to the upper organic phase with increasing surfactant: U_{24} ratio (from left to right): 2:1, 4:1, 11:1, 22:1, corresponding to the scattering curves in (b) are also shown at the top right.

In the $\text{NH}_4\text{-U}_{32}$ series, maximum cluster distribution ratio ($D = [\text{U}]_{\text{org}} / [\text{U}]_{\text{aq}} = 2.1 \times 10^4$) was obtained from a 15:1 surfactant: U_{32} ratio, and decreases with increasing surfactant: U_{32} ratio. (**Table 4.1**, compositional analysis of aqueous phase, post-extraction). The SAXS curve of the 15:1 surfactant: U_{32} extraction in kerosene is nearly identical between $q=0.2\text{-}0.4 \text{ \AA}^{-1}$ to the aqueous clusters (**Figure 4.2a**), indicating complete transfer of U_{32} , intact. In finer detail than shown in **Figure 4.2a**, the 15:1, 20:1, 30:1 and 40:1 ratios all gave similar scattering profiles (**Figure S4.3**), but with decreasing intensity, reflecting lower concentration of U_{32} transferred to the organic phase. This is a result of low CTAB concentration, preventing full encapsulation of cluster species for phase transfer. For SAXS curves of 60:1, 80:1 and 150:1 ratio (**Figure 4.2a**), the decreasing cluster scattering intensity trend continues ($q=0.1\text{-}0.4 \text{ \AA}^{-1}$), but this is accompanied by a steady rise in scattering intensity below $q=0.6 \text{ \AA}^{-1}$. Guinier analysis of U_{32} scattering gives a relatively invariant ($8.4 \pm 0.5 \text{ \AA}$) radius of gyration (R_g , shape independent measure of size) with varying surfactant: U_{32} ratio, also consistent with the R_g of the aqueous U_{32} (**Table A4.4**), meaning the U_{32} geometry is retained in the organic phase. The increasing scattering at low- q arises from reverse micelles that form when surfactant is in excess of that necessary to charge-balance the clusters. This is confirmed by SAXS characterization of the organic phase contacted with water only (**Figure S4.4**). The optimal surfactant: U_{32} ratio for maximum U_{32} transfer under these solution conditions (15:1) is considerably less than 40:1, where -40 is the charge of the uranyl polyanion shell. This suggests there is co-extraction of NH_4^+ or H^+ cations to maintain charge balance in the organic phase, and these can reside inside the U_{32} capsules, in the aqueous reverse micelles, or in the organic phase. These species were not identified in the original structure of U_{32} ,³¹ but a rough calculation of the capsule volume suggests up to 20 hydronium, ammonium or water molecules could reside inside.

X-ray scattering of Li-U_{24} transferred into octadecene presented similar trends (**Figure 4.2b**) of increasing micelle scattering with increased surfactant: U_{24} ratio. The scattering between $q=0.2 - 1 \text{ \AA}^{-1}$ can be fit with a core-shell model in good agreement with aqueous U_{24} , indicating the clusters transfer to the organic phase intact. (**Figure S4.5**), and the R_g is consistent with the aqueous Li-U_{24} (**Table S4.4**) for all data of different surfactant: U_{24} ratios. Upon further studies, we found that these extraction techniques were only viable with the cluster form of uranium. Simple uranyl ions and monomeric uranyl peroxide species did not extract under the same conditions and thus purification of uranyl cluster species can be attained using this method. The

surfactant:U₂₄ ratio of 11:1 and greater gives the distinct rise in the low-q region: as described for U₃₂, implying formation of aqueous reverse micelles. The most efficient extraction of U₂₄ is obtained between a 11:1 and 22:1 surfactant:cluster ratio, with D=135 (**Table 4.1**), two orders of magnitude lower than the most effective extraction of U₃₂.

In view of the -24 charge of U₂₄, this suggested that Li was either encapsulated during the extraction or coextracted^{36,37} in the aqueous micelles to maintain charge balance in the organic phase. We investigated further utilizing ⁷Li NMR of the organic phase. **Figure 4.3** shows a broad ⁷Li peak that shifts from -10 ppm towards 0 with increasing surfactant:U₂₄; and very low surfactant:cluster (4:1) ratio indicates no lithium transferred into the organic phase. Prior ⁷Li NMR characterization studies in water and the solid-state showed that Li exchanges very rapidly from inside U₂₄ to the surrounding medium. Even in the solid-state, the encapsulated Li (-13 ppm) and the hydrated external Li (0 ppm) can only be distinguished by cooling to slow the exchange.³⁸ Similarly, the broad peak observed here is interpreted as Li that enters the organic phase inside the aqueous micelles, and exchange occurs between U₂₄ and the micelles. Increasing the size and number of the reverse micelles, by increasing surfactant:cluster ratio, shifts the averaged peak towards the non-encapsulated 0 ppm position. This is different from Li-U₂₄ dissolved in water: in prior experiments, where only a single sharp peak of hydrated Li is observed at 0 ppm.³⁸ This result indicates the clusters probably do not reside inside the large aqueous reverse micelles observed by SAXS, contrary to prior studies of vanadium-POMs in reverse micelles.³⁹ We also obtained a Li-U₂₄-surfactant precipitate by adding aqueous CTAB to aqueous Li-U₂₄ and collecting the floc (see experimental). ⁷Li NMR of this precipitate in kerosene benchmarks the encapsulated Li with minimal exchange with solution, deterred by the hydrophobic surroundings (**Figure 4.3**). This chemical environment provides an unprecedented non-mobile state, as evidence by three distinct peaks of encapsulated Li at roughly -10 (15 %), -11 (56 %) and -12 ppm (29 %). The different coordination environments will be elucidated by future experimental studies corroborated with theory.

Table 4.1

Composition Analysis (U, Br) of Aqueous Phase Post-extraction

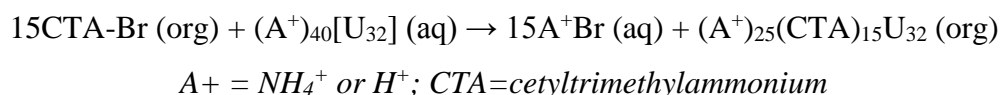
Specie	Number of surfactant per cluster	[U] U ₂₄ -mM U ₃₂ - μ M	Std. error (mM)	Uranium distribution ratio ¹	[Br]M ³	[Br] _{aq} /[U] _{org}
LiU ₂₄ samples	2	58.333	3.22	2.83	0.166	1.6
	4	3.212	0.017	51.4	0.412	2.5
	11	1.246	0.013	132	1.437	8.8
	22	1.186	0.011	139	1.415	8.6
	33	3.656	0.032	45.1	2.469	15.3
NH ₄ U ₃₂ samples	15	7.977	N/A ²	2.1 x 10 ⁴	2.407	14.6
	30	29.642	N/A ²	2.8 x 10 ⁴	1.639	10.3

1- distribution ratios ($D = [U]_{org} / [U]_{aq}$, following extraction calculated by quotient of initial uranium concentration over final uranium concentration measured by ICP)

2- concentration too low to accurately determine standard error

3- the Br analyses have an instrumental uncertainty of +/- 2.4% (1 sigma) as determined by triplicate analyses of known standards.

The 15:1 (U₃₂) surfactant:cluster ratio represents the optimal conditions in which 1) U₃₂ is completely extracted, and 2) X-ray scattering of the organic phase is dominated by the monodisperse cluster, without micelle scattering. As phase transfer of clusters from the aqueous to organic phase is driven by electrostatic association and ion-exchange at the water-organic emulsion interface, we can write a simplified balanced equation for the transfer of U₃₂ with a 15:1 surfactant:U₃₂ ratio:



Consistent with this, Br concentration increases in the aqueous phase with increasing transfer of U₃₂ into the organic phase. (**Table 4.1**) The surfactant:cluster ratios of 15:1 for optimal U₃₂ extraction may be controlled by the number of trimethylammonium surfactant heads that can associate with the cluster surface. The surface area of the cluster, determined from the solid-state structure is 1257 Å², providing 84 Å² per surfactant, exactly coincident with that reported for surfactant-encapsulated molybdenum keplerate.⁴⁰ Further confirmation that (A⁺)₂₅(CTA)₁₅U₃₂ precisely describes this specie in the organic solvent comes from the 15:1 ratio of Br(aq):U₃₂(org) determined from compositional analysis of the aqueous phase before and after extraction(**Table 4.1**).

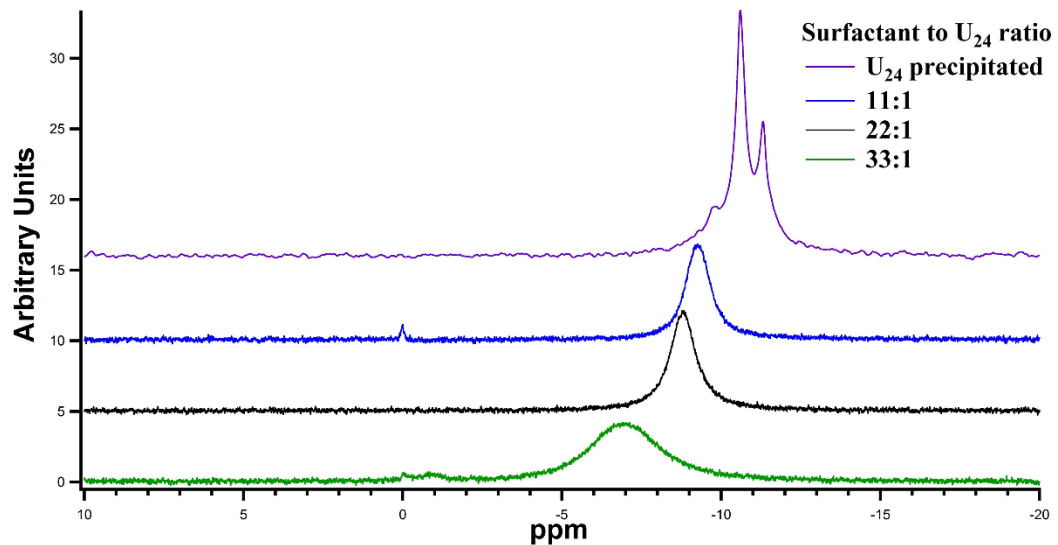


Figure 4.3 ^7Li NMR data of U_{24} in octadecene. The top spectrum (purple) is Li-U_{24} precipitated with CTAB, and the precipitate is redissolved in octadecene. This benchmarks lithium encapsulated in U_{24} in a hydrophobic medium. The additional spectra are Li-U_{24} extracted into octadecene. The broad peak shifted towards 0 ppm (free hydrated lithium) indicates exchange of lithium between U_{24} and reverse micelles.

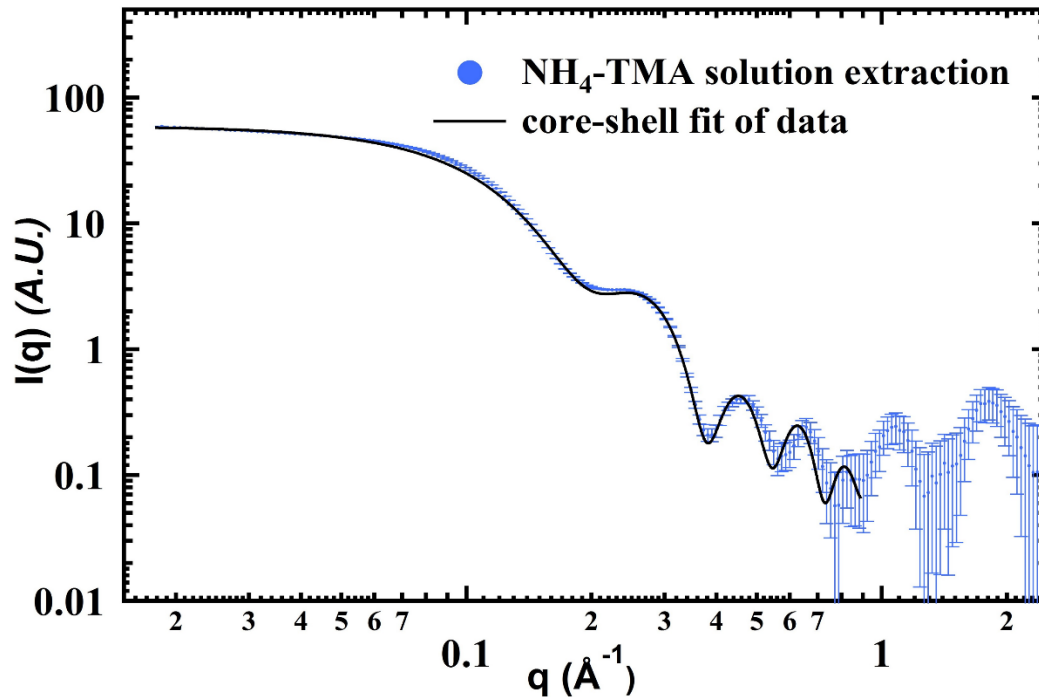


Figure 4.4 Log q-log I(q) scattering curve for 0.75 M U (NH₄-U₃₂) extraction with TMAOH. Two core-shell model provided the fit between $q= 0.02 - 0.9 \text{ \AA}^{-1}$. Parameters of the core-shell fit include two phases: Phase I (larger unknown cluster) – cluster radius = 19.1 \AA , Phase II (U₃₂) – cluster radius = 9.1 \AA . Ratio of U₃₂:larger cluster is 2.5:1, based on the two-phase fit of the scattering data.

Because $\text{NH}_4\text{-U}_{32}$ is poorly soluble and tends to precipitate at the aqueous-organic interface, we added a small amount of tetramethylammonium hydroxide TMAOH; (1/10th of NH_4OH by mole) to obtain higher concentration of $\text{NH}_4\text{-U}_{32}$ (0.75 molar uranium). Interestingly, in these conditions, the capsules extracted into kerosene are different (**Figure 4.4**) than pure U_{32} . Some U_{32} persists, but the narrower oscillations ($q=0.3\text{-}0.8 \text{ \AA}^{-1}$) and the 0-slope in the low- q region indicate the formation of a larger, but still discrete cluster. Using a two-phase model³⁵ of U_{32} plus the unknown phase, we determined the larger cluster is slightly more than twice the size of U_{32} . A reasonable explanation is dimerization of U_{32} clusters upon addition of base. This seems very plausible because 1) the open end of the cluster has four terminal peroxide ligands that could be eliminated or replaced by hydroxide and bridge to a second cluster, forming a hypothetical U_{64} ; and 2) non-polar solvents generally drive ions together, providing opportunity for linking. This large cluster is not detected in the aqueous phase from which it was extracted meaning that the organic phase enables formation and stabilization of a prior unrecognized cluster species. This knowledge presents an opportunity to expand the library of uranyl peroxide clusters by exploiting entirely different solution conditions and investigating the chemistry that transpires at the aqueous-organic interface. The challenge is crystallizing these species from the organic media, and these investigations are also underway.

To test the broad utility of the role of uranyl peroxide clusters in aqueous-to-organic phase transfer, we also dissolved SIMFUEL, largely consisting of U(IV)O_2 (but also includes common isotope decay products of ^{235}U),⁴¹ in ammonium hydroxide-peroxide solutions and proceeded with solvent extraction and characterization, per our developed protocol of study (**Figure 4.5**). As observed in the photograph, not all of the SIMFUEL dissolved in the alkaline solution, evidenced by the black solid that collected at the emulsion interface between the aqueous and organic solutions. **Figure 4.5** also shows SAXS analysis of the aqueous phase, the clusters extracted into the organic phase, and simulated U_{32} . While clusters likewise form from SIMFUEL (as observed prior),⁴² and they transfer to the kerosene layer, there are some differences between the aqueous and organic phase clusters, discussed and elucidated below.

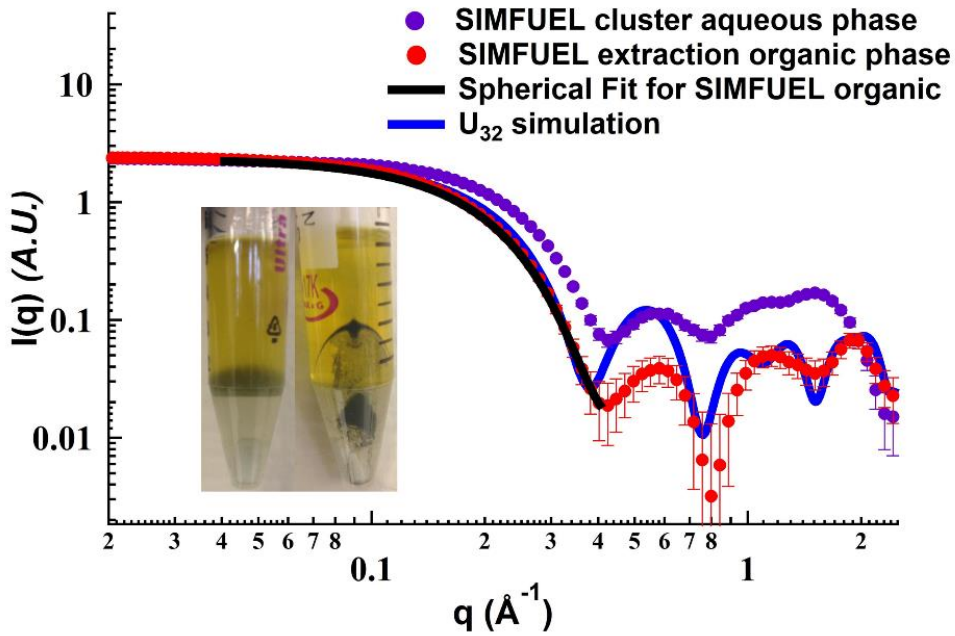


Figure 4.5 Extraction of uranium from SIMFUEL. The above SAXS curve (red) is the organic phase post-extraction of uranium. The curve was fit using Modeling II, a spherical model to give the (black) fit curve. The fit yields a particle diameter of 21.88\AA which agrees with the simulated (blue) curve for U_{32} with a particle diameter of 21.50\AA

First, the descent in scattering intensity in the Guinier region for the organic phase occurs at lower q than for the aqueous phase, suggesting larger clusters exist in the organic phase. Roughly, the R_g of the clusters in the organic phase is 9.51 \AA and the R_g of the clusters in the aqueous phase is 7.96 \AA . Second, the aforementioned slope of the aqueous phase is shallower than that of the organic phase, possibly indicating polydispersity (i.e. a mixture of cluster sizes). Additionally, the simulated U_{32} scattering curve matches that of organic phase experimental scattering data, up to $q=0.4 \text{ \AA}^{-1}$, at the point of the scattering minimum and prior to the first oscillation. This suggests that there is a mixture of cluster species in the aqueous phase, but U_{32} preferentially partitions into the organic phase. In a prior study, we noted dissolution of studtite in NH_4OH produced a mixture of U_{28} ($R_g \sim 7.5 \text{ \AA}$) and U_{32} ($R_g \sim 8.4 \text{ \AA}$), rather than pure phase U_{32} , as is the product from uranyl nitrate.³¹ We suggest a similar mixture forms upon dissolution of the SIMFUEL, followed by preferential extraction of U_{32} . Neither the formation of a mixture of clusters in this process or preferential extraction of the larger cluster (tentatively U_{32}) from the mixture is well-understood, and both phenomena represent opportunity for further investigation.

The first oscillation of both the aqueous phase and the extracted clusters, although distinct, is clearly diminished compared to that of simulated $\text{NH}_4\text{-}U_{32}$. We tentatively attribute this to encapsulation of heavy atoms. In a prior study, we have synthesized U_{24} capsules that contain heavy p-block metal-oxo clusters, $[\text{Bi}_6\text{O}_8]$ and $[\text{Pb}_8\text{O}_6]$.⁴³ The SAXS curves of these clusters likewise exhibit a very similar suppression of the first oscillation, that is also observed in the simulated data from their crystal structures. This is because the capsule-like character that yields very distinctive oscillations is altered when atoms of higher electron density are located in the core, decreasing the electron scattering contrast between the shell and the core. However, as discussed below, few non-uranium elements are co-extracted with the uranium. Therefore, we suspect there are uranium ions encapsulated. This has been observed in several single-crystal structural studies.^{4,9,32}

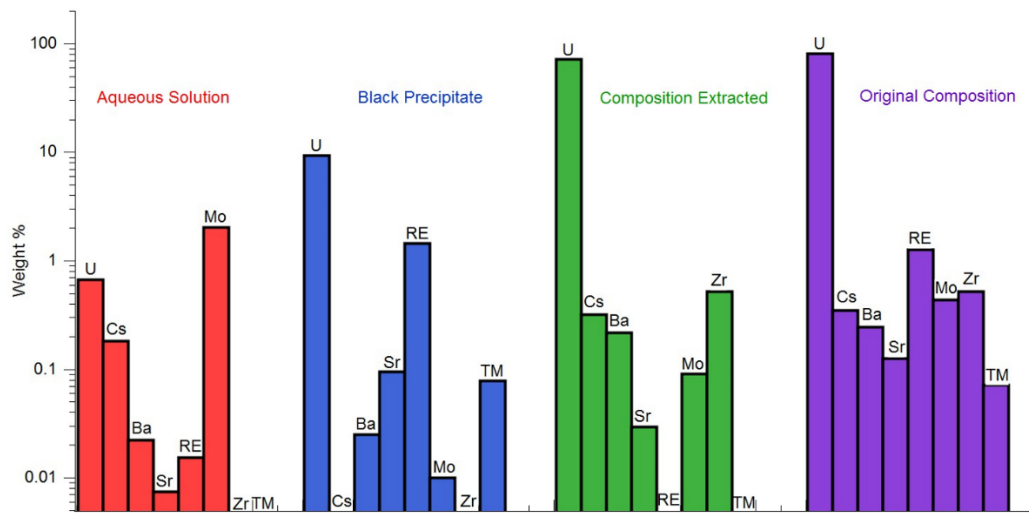


Figure 4.6 Composition analysis of SIMFUEL extraction. Visual representation of the metal composition (log scale of weight %) after the SIMFUEL extraction process has taken place in the aqueous phase (red), black insoluble precipitate in the aqueous phase (blue), calculated extraction composition (green, original compositional minus extracted and precipitated components) and the original SIMFUEL composition (purple).

ICP-OES and ICP-MS compositional analysis of the aqueous phase and black solid (post-SIMFUEL extraction) provides an estimate of the major species remaining after extraction vs. the extracted fraction (**Figure 4.6**). The major species shown to be extracted (**Figure 4.6**, green bars) is uranium with over 88% of the original uranium composition extracted into the organic phase, also including minor species Zr, Cs, and Ba (all less than 0.4%). We might expect the inclusion of Zr, Cs, and Ba as counterions contained within the hollow cluster core. U_{32} has been shown to readily undergo ion exchange, associating with different counterions in solution⁴⁴ making it an “ion sponge” and from the standpoint of cluster extractions, possibly an ion shuttle to organic media. Under further investigation of the composition data, we extrapolated that only ~1.1 total fission product elements were extracted per U_{32} cluster. During the extraction process, a black precipitate remains (composition described in blue bars in **Figure 4.6**), composed mainly of uranium and rare earth metals (RE) with minor species including Sr and other transition metals (TM) (all less than 0.1%). The black color indicates that not all the uranium was oxidized during the *in-situ* extraction process, where oxidation is necessary for formation of the capsules. Because we targeted the same uranium concentration as the U_{32} synthesis/extraction process described above, the issue with complete dissolution is likely kinetic, and also suggests opportunity to isolate intermediate mixed valent uranium species,^{45,46} clusters in particular.⁴⁷ Other rare earth metals Gd, Eu, Pr, La, Ce, and Nd), transition metals (Y, Ru and Pd) and Sr were present in the precipitate as expected due to poor solubility in alkaline pH. Mo is the only element of significant composition in the aqueous solution (red) after the extraction with minor species including U and Cs (<0.7%) as these are the only metal oxides that have a notable solubility in alkaline pH.

Finally, as a proof of concept, we demonstrated that solvent extraction is also possible for transfer of clusters from mildly acidic environments to organic media. Starting with the synthesis of $[(UO_2)_{60}(O_2)_{60}(C_2O_4)_{30}]^{36-}$ ($U_{60}Ox_{30}$) ($Ox=oxalate$) per literature procedure,⁴⁸ the same solvent extraction method was utilized for this solution at around pH 4. From the SAXS analysis of the organic phase (kerosene/hexanol 8.4:1) post-extraction (**Figure S4.7**), it can be seen that the acidic $U_{60}Ox_{30}$ cluster persists through the extraction. With these results, we believe that the extraction of any uranyl capsule species is achievable, where the relatively low charge-density of the clusters is the driving force for phase transfer. This suggests counterions are amply present in the encapsulated clusters, as indicated by the Li-NMR study on LiU_{24} extraction. Current and

future studies investigate the role of these counterions and charge in the transfer process.

4.4 Conclusions

Here we have demonstrated that uranyl POMs selectively partition into organic solvent from water by simple ion-exchange; and the unique capsule form persists, identified by X-ray scattering. Surfactant extraction of uranium is only possible with uranyl clusters, as monomeric complexes are too charge-dense, and remain in the aqueous phase. Currently exemplified, the surfactant/organic medium offers opportunity to study uranyl clusters for the first time outside of aqueous solution, bringing forth recognition of stabilization of larger and lower charge-density cluster forms, prior unrecognized phenomena of encapsulated species, and understanding cluster behavior at aqueous-organic interfaces that drives phase transfer.

4.5 Experimental Section

Caution: Although isotopically depleted uranium was used in this study, precautions for handling toxic and radioactive materials should be followed.

Preparation of **LiU₂₄** was described prior.^{32,7} Briefly, the lithium salt of the monomeric uranyl triperoxide is prepared by combining aqueous uranyl nitrate (0.5g in 6mL of water), 3mL of 30% hydrogen peroxide, and 4mL of 4M LiOH, followed by rapid precipitation with ethanol addition. The precipitate is filtered, washed with more ethanol and dried. This monomer powder is redissolved in water and 100 μ m Cu(NO₃)₂ is added to catalyze peroxide decomposition and promote self-assembly of U₂₄. With the addition of Cu²⁺ catalysts to assist in cluster self-assembly, the process from Li₄UO₂(O₂)₃ monomer to U₂₄ cluster takes around 36 hours and is monitored by Raman spectroscopy.

For the preparation of **NH₄-U₃₂**, we combine uranyl nitrate (0.5g in 6mL of water), 3mL of 30% hydrogen peroxide, and 4mL of 25% ammonium hydroxide solution. Ethanol is added to the reaction mixture and the precipitate is isolated as described above. However, this isolated product is the U₃₂ cluster, as it self-assembles rapidly. Extraction experiments were also performed without prior isolation and re-dissolution of the cluster.

Preparation of aqueous **U₆₀Ox₃₀** was described prior.^{31,44} Briefly, a one-pot reaction mixture containing uranyl nitrate (0.5M), hydrogen peroxide (30%), lithium hydroxide (2.4M), potassium chloride (0.5M) and oxalic acid (0.5M) was prepared yielding an initial pH of ~4. This

solution is intended for $U_{36}O_{x6}$ crystallization but clusters in solution were identified as $U_{60}O_{x30}$ by X-ray scattering. The solution was filtered and used “as is” with no additional purification or crystallization steps.

For solvent extraction of these cluster species, we use a solution of 25 mM cetyltrimethylammonium bromide (CTAB) in a mixture of kerosene and hexanol (kerosene:hexanol = 8.7:1). We replace kerosene with octadecene in some experiments to exploit lower solvent scattering in the high-q region (**Figure S2.2**), providing better resolution of cluster scattering oscillations. The aqueous uranium cluster solution is then added to the CTAB organic solution for solvent extraction, shaken briefly by hand, then left to equilibrate. Both cluster concentration and surfactant concentration was varied to bracket optimal surfactant:cluster ratios for extraction (**Table S2.2**) and to determine the number of surfactant molecules that associate with a single capsule.

For the preparation of Li- U_{24} -surfactant precipitate for benchmarking encapsulated Li via ^7Li NMR, non-quantitatively, a solution of U_{24} (synthesis described above) and a solution of 0.1M aqueous CTAB in excess were combined to form a yellow precipitate and colorless aqueous solution. The precipitate is collected by centrifugation and decantation of the liquid. The solid CTA-Li- U_{24} is then dried in a vacuum between 30-50°C. The dry solid is dissolved in a mixture of 8.7:1 kerosene to hexanol.

For experiments done using SIMFUEL as a starting material, we suspended 50 mg of the SIMFUEL powder in 0.6 mL of water, 0.4mL of ammonium hydroxide (4M) and 0.3mL of hydrogen peroxide (30%), adapting from the prior study of Burns who demonstrated filtration separation of uranium from the minor oxides in SIMFUEL.⁴² The majority of the UO_2 is rapidly oxidized, yielding a light brown (black and yellow mixed) suspension. The optimized surfactant:cluster ratio for extracting U_{32} (15:1 from above) is introduced to the system in 3.9mL of kerosene and was contacted with the aqueous phase with shaking. The extraction process went to completion within 2 hours giving a distinct yellow organic phase and a colorless aqueous phase.

Solutions were analyzed by Small Angle X-ray Scattering, (SAXS) Data was collected on an Anton Paar SAXSess instrument utilizing Cu- $K\alpha$ radiation (1.54 Å) and line collimation. Samples and appropriate background solutions were sealed in 1.5 mm diameter glass capillaries

and measured with 30 minute exposure times on a scale from $q = 0.018 - 2.5 \text{ \AA}^{-1}$. All analyses and fits to determine R_g , size, shape, size distribution, core-shell modeling, and PDDF (pair distance distribution function) were carried out utilizing the IRENA³⁵ macros within IgorPro 6.3 (Wavemetrics) software. SolX^{50,51} software was used to simulate x-ray scattering data from solid-state crystal structure files.

Compositional analysis (U and Br)

U Analysis: Final aqueous separation product samples were initially diluted in 18 M Ω water to contain approximately 0.06M of base (LiOH or NH₄OH). These samples were diluted with 5% (v/v) HNO₃ to produce 10 mL samples containing ~20 ppm U and ~5 ppm Li. These solutions were introduced into a PerkinElmer Optima 8000 inductively coupled plasma optical emission spectrometer (ICP-OES) for chemical analysis. U was analyzed using a GemCone cyclonic nebulizer/spray chamber and alumina torch set up. Standard manufacturer flow and power rates were used during analysis. Wavelengths used for quantification were 385 and 610nm for U and Li, respectively. Winlab 32 software was the software interface.

Br Analysis: Final aqueous separation product samples were diluted in 18 M Ω water to contain approximately ~20ppm Br. These solutions were introduced into a Dionex ICS-500 ion chromatography (IC) system equipped with AS-23/AG-23 column set, ERAS suppressor, and conductivity detector for quantification. The Dionex ICS-5000 system used a 4.5mM NaCO₃/0.1mM NaHCO₃ mobile phase and 25 μ L injection loop. The system was equipped with an AS-23/AG-23 column set for separation, ERAS suppressor, and conductivity detector for quantification. Chromeleon 6.8 was the software interface.

⁷Li Nuclear Magnetic Resonance (NMR) Spectroscopy ⁷Li NMR spectra were collected on a Bruker 400 MHz DPX 400 spectrometer with a 5 mm probe, tuned to a frequency of 155.5 MHz for ⁷Li. A saturated LiCl 10% D₂O/H₂O solution was used as an external reference. Organic solutions were run with a 10% benzene-d₆ lock solvent with 2000 scans and a spectral width of 7763.98 Hz (-25 - +25 ppm).

For a more detail and a full description of materials and methods, see supplemental information provided in Appendix Chapter 9.2.

4.6 Acknowledgements

This material is based upon work supported as part of the Materials Sciences of Actinides Center, an Energy Frontier Research Center funded by the U.S. Department of Energy, Office of Science, Office of Basic Energy Sciences under Award Number DE-SC0001089. The aqueous analyses were conducted at the Center for Environmental Science and Technology at University of Notre Dame, and we thank Jon Loftus for technical support. Homepage: msa-efrc.com

Chapter 5

Resolving Confined ^7Li Dynamics of Uranyl Peroxide Capsule

U_{24}

Jing Xie, Harrison A. Neal, Jennifer Szymanowski, Peter C. Burns, Todd M. Alam,
May Nyman, and Laura Gagliardi

Inorg. Chem. **2018**, DOI:10.1021/acs.inorgchem.8b00474

5.1 Abstract

We obtained a kerosene-soluble form of the lithium salt $[\text{UO}_2(\text{O}_2)(\text{OH})_2]_{24}$ phase (Li- U_{24}), by adding cetyltrimethylammonium bromide surfactant to aqueous Li- U_{24} . Interestingly, its variable-temperature solution ^7Li NMR spectroscopy resolves two narrowly spaced resonances down to $-10\text{ }^\circ\text{C}$, which shift upfield with increasing temperature, and finally coalesce at temperatures $> 85\text{ }^\circ\text{C}$. Comparison with solid-state NMR demonstrates that the Li dynamics in the Li- U_{24} -CTA phase involves only exchange between different local encapsulated environments. This behavior is distinct from the rapid Li exchange dynamics observed between encapsulated and external Li environments for Li- U_{24} in both the aqueous and the solid-state phases. Density functional theory calculations suggest that the two experimental ^7Li NMR chemical shifts are due to Li cations coordinated within the square and hexagonal faces of the U_{24} cage, and they can undergo exchange within the confined environment, as the solution is heated. Very different than U_{24} in aqueous media, there is no evidence that the Li cations exit the cage, and therefore, this represents a truly confined space.

5.2 Introduction

Uranyl peroxide capsules¹ have received considerable attention since their discovery in 2005,² as a new family of polyoxometalates (POMs) that are aesthetically beautiful with rich topological diversity. Moreover, they provide opportunities to understand uranyl speciation in alkali peroxide solutions and solids, which are exploited in cradle to grave processes of the nuclear fuel cycle (e.g., separation, enrichment and fuel fabrication).³⁻⁶ In aqueous solution, uranyl UO_2^{2+} , with its two trans “yl” oxygen atoms, can self-assemble into unique hollow capsule topologies through peroxide and hydroxide bridges, in the presence of proper counterions (mainly alkali metal cations) and in certain pH environments.⁷⁻⁸ Within the past decade, more than 60 capsule topologies containing up to 124 uranyl units have been characterized.⁷ Most studies focused on the aqueous behaviors of uranyl capsules, including growth mechanism,⁹⁻¹⁰ supramolecular assembly,¹¹⁻¹² alkali cation templating,¹³⁻¹⁴ and exchange of encapsulated species between solution and capsules.¹⁵ Only recently uranyl POMs were extracted into an organic solution from water by ion exchange,¹⁶ enabling new solution studies beyond the aqueous media.

When dissolved in water, uranyl POMs exchange encapsulated alkali cations, which pass through the square, pentagonal and hexagonal faces of the cage between the capsule and the surrounding medium.¹⁷ Moreover, recent magic-angle-spinning nuclear magnetic resonance (MAS NMR) studies revealed a high-rate solid-state exchange of Li^+ and aqua species between the uranyl capsule of solid U_{24} ($[\text{UO}_2(\text{O}_2)(\text{OH})]_{24}^{24-}$),^{15,18} and U_{60} ($[\text{UO}_2(\text{O}_2)(\text{OH})]_{60}^{60-}$)¹⁹ clusters, and the external lattice containing hydrated alkalis. In a prior study,¹⁶ we obtained a Li-U_{24} -surfactant precipitate by adding aqueous cetyltrimethylammonium bromide (CTAB) to aqueous Li-U_{24} , where the positively-charged CTA^+ cation becomes an exterior counterion to the anionic capsule. We denoted this surfactant precipitate as **Li-U₂₄-CTA**. Surprisingly, solution ⁷Li NMR spectroscopy of this precipitate dissolved in kerosene suggested an unprecedented reduction in cation mobility, featuring two distinct encapsulated Li resonances with chemical shifts around $\delta = -11$ ppm. This observation provided the opportunity to probe the coordination environment of Li cations within the U_{24} capsule, and to achieve a better understanding of the Li dynamics in a confined space.

U₂₄ is one of the most studied uranyl POMs, because its synthesis is well-documented and reproducible, and it is readily soluble in water, as a lithium salt.^{2,9} The capsule has six square faces, formed of four uranyl units bridged by peroxide, and eight hexagonal faces, formed of six uranyl units that are alternatively bridged by peroxide and hydroxide units (Figure 1). Each hydroxide edge is shared by two hexagonal faces and each peroxide edge is shared by one square and one hexagonal face. X-ray structures have shown that alkalis tend to bind under the faces, coordinated to the yl-oxygens that point inwards toward the center of the capsule; not unlike the coordination of alkalis in crown ethers.^{2, 18, 20-24} This has inspired computational studies¹³ that confirmed the preferred coordination environment of alkali cations is commensurate with the size of the capsule face. While smaller alkali species like Li⁺ and Na⁺ prefer to coordinate to the square faces, K⁺ favors the pentagonal faces, and larger alkali cations like Rb⁺ and Cs⁺ prefer to coordinate to the hexagonal faces.

Herein, we performed a combined quantum chemical and experimental study to investigate the encapsulated Li species within **Li-U₂₄-CTA** in the solid-state, and dissolved in nonpolar solvent. We explore the dynamics of encapsulated Li, utilizing variable temperature (VT) liquid phase NMR experiments, while we employ solid-state ⁷Li NMR to probe the interactions of the cationic CTA headgroups with the encapsulated Li through the capsule faces. Computationally we employed cluster fragment models and full U₂₄ cage models to explore different Li binding sites, which offered insights into the Li coordination and dynamics, when it is confined within the capsule.

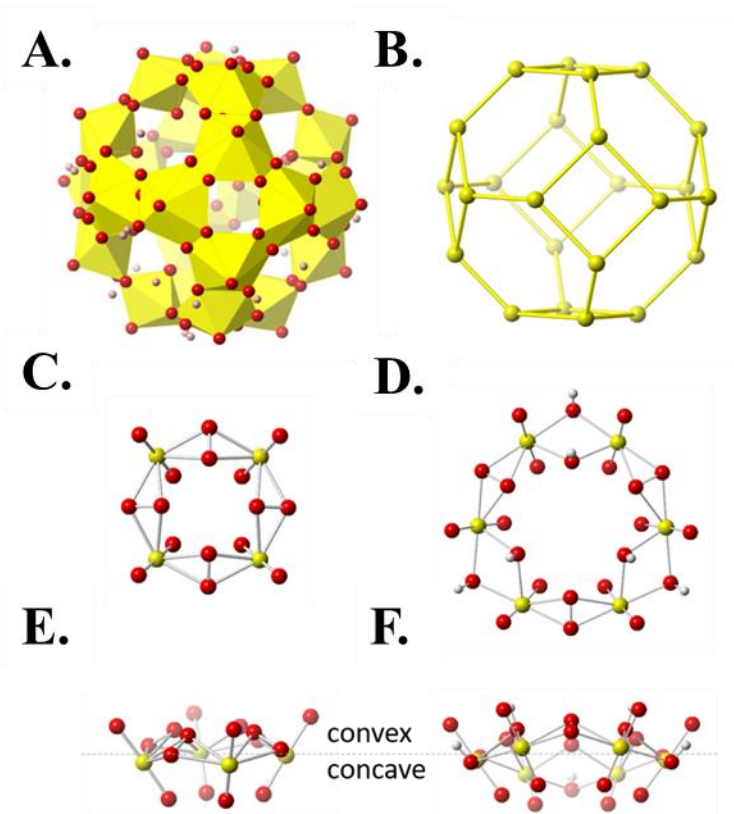


Figure 5.1 Polyhedral (A), graph (B), and ball-and-stick (C-F) representations of the topology of U_{24} , and fragments thereof. The cluster is composed of six square (C) and eight hexagon (D) building blocks. The side view of square (E) and hexagon (F) motif shows the convex (external) and concave (internal) side. Color scheme: U, yellow; O, red; H, white.

5.3 Methods

5.3.1 Experimental Methods

Caution: Although isotopically depleted uranium was used in this study, precautions for handling toxic and radioactive materials should be followed.

Preparation of **LiU₂₄** was described previously.²¹ Briefly, the lithium salt of the uranyl triperoxide monomer unit is prepared by combining aqueous uranyl nitrate (0.5 g in 6 mL of water), 3 mL of 30% hydrogen peroxide, and 4 mL of 4M LiOH. The monomer is isolated by rapid precipitation using excess ethanol, vacuum filtration and drying. The monomer powder is redissolved in water and 100 μ M Cu(NO₃)₂ is added to catalyze the self-assembly of U₂₄ within 36 hours. The cluster self-assembly process is monitored by Raman spectroscopy and Small Angle X-ray Scattering (SAXS).

Li-U₂₄-CTA is synthesized by the addition of aqueous 25 mM cetyltrimethylammonium bromide surfactant in excess to the Li-U₂₄ solution and then dried. The resulting solid is washed with water to remove remaining surfactant and non-encapsulated Li, and then air-dried. Purification by washing was required for accurate compositional analysis measurements. All measurements are phase separate. There is no contact between water/organic phases, merely precipitation of solid with surfactant then redissolution of solid into organic solvent.

Solutions of Li-U₂₄-CTA (approximate concentrations of 50mM by uranium) were analyzed by Small Angle X-ray Scattering (SAXS), collected on an Anton Paar SAXSess instrument utilizing Cu-K α radiation (1.54 Å) and line collimation. Samples and appropriate background solutions were sealed in 1.5 mm diameter glass capillaries and measured using a 30-minute exposure time over a $q = 0.018$ - 2.5 \AA^{-1} range. All SAXS analyses to determine radius of gyration (R_g), size, shape, size distribution, core-shell modeling, and PDDF (pair distance distribution function) were carried out utilizing the IRENA²⁵ macros within IgorPro 6.3 (Wavemetrics) software. SolX²⁶ software was used to simulate x-ray scattering data from solid-state crystal structure files. Samples described as aqueous were prepared in and referenced to background of 18M Ω water. **Li-U₂₄-CTA** samples were prepared in and referenced to background of a kerosene/hexanol co-solvent system in 9:1 volume ratio respectively.

Compositional chemical analysis (U and Li) of were obtained on **Li-U₂₄-CTA** that was digested in 5% (v/v) HNO₃ and diluted in 18 MΩ water to contain approximately 0.06M of Li followed by an additional dilution with 5% (v/v) HNO₃ to produce 10 mL samples containing ~20 ppm U and ~5 ppm Li, the optimal concentrations for quantitative detection. The resulting solutions were introduced into a PerkinElmer Optima 8000 inductively coupled plasma optical emission spectrometer (ICP-OES) for chemical analysis. Elemental uranium was analyzed using a GemCone cyclonic nebulizer/spray chamber and alumina torch set up. Standard manufacturer-suggested flow and power rates were used during analysis. Wavelengths used for quantification were 385 and 610 nm for U and Li, respectively, with Winlab 32 software being used for data acquisition and processing.

Solution ⁷Li NMR spectra were collected on a Bruker 500 MHz DPX 500 spectrometer with a 5 mm probe, tuned to a frequency of 194.4 MHz for ⁷Li using a secondary saturated LiCl 10% D₂O/H₂O external standard for chemical shift reference ($\delta = 0.0$ ppm). Organic solutions were run in a 9:1 kerosene/hexanol co-solvent system with a 10% (vol) benzene-d⁶ lock solvent utilizing 512 scan averages and a spectral width of 7764 Hz (50 ppm). The VTNMR spectra were simulated with WINDNMR²⁷ to estimate coalescence temperature and exchange rate. The solid-state MAS NMR spectra were obtained on a Bruker Avance-III 600 at 233.2 and 600.1 MHz for ⁷Li and ¹H, respectively, using a 2.5 mm probe spinning between 20 and 25 kHz. A rotor synchronized Hahn echo was used for the ¹H NMR, while a single pulse Bloch decay with high power ¹H decoupling was used to obtain the ⁷Li MAS NMR spectra. For the solid state experiments the ¹H NMR chemical shifts was referenced to the secondary external reference adamantane ($\delta = + 1.63$ ppm) with respect to TMS ($\delta = 0.0$ ppm), while the ⁷Li chemical shifts were referenced to a secondary 1M LiCl ($\delta = 0.0$ ppm) standard.

5.3.2 Computational Methods

We employed both truncated cluster and full-cage models to investigate the interaction between Li⁺ ions and the U₂₄ capsule. We extracted three truncated cluster models from the fully optimized U₂₄ cage, including a square, a hexagon, and a square-hexagon model. Both square and hexagon models are neutral and the square-hexagon model has a total charge of -2. According to experiment, when the Li-U₂₄-CTA precipitate is dissolved in kerosene, an estimated 11 Li⁺ cations and numerous H₂O molecules are encapsulated in each U₂₄ cage. We

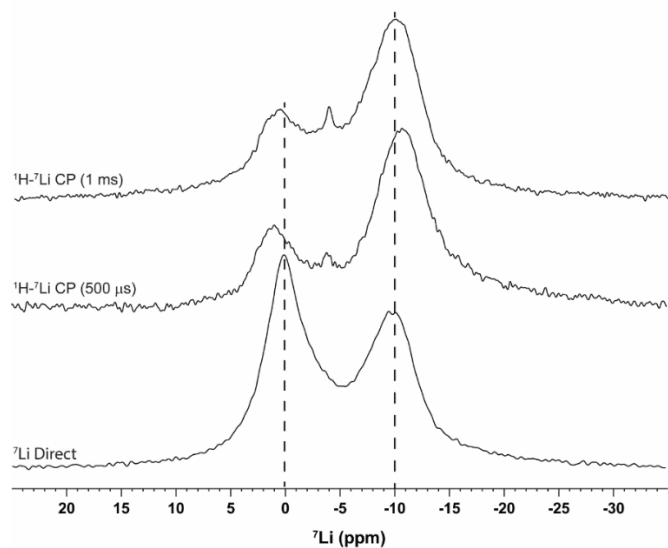
first investigated non-hydrated Li^+ cations interacting with the three cluster models and then hydrated Li^+ ions, by including explicit water molecules in the model, to capture the hydration effect. To maintain the symmetry and the structure of the building blocks, we performed constrained geometry optimizations of the various models. The positions of the U and O atoms of the different building blocks were kept fixed, while the positions of the H on the hexagon, Li atoms and H_2O molecules were allowed to relax. For the truncated clusters we performed density functional theory (DFT) calculations using the hybrid functional B3LYP²⁸⁻²⁹ with the 6-31G(d,p)³⁰⁻³¹ basis sets on H, O, and Li and the Stuttgart/Dresden (SDD)³²⁻³³ basis set and corresponding pseudo potential for U, denoted as the B3LYP/6-31G(d,p)&SDD method. In all the cluster model calculations we employed the implicit solvent model based on density (SMD)³⁴ model to account for the solvent effect by using water as solvent. The full-cage structures were fully optimized without any constraints using the Perdew-Bruke-Ernzerhof (PBE)³⁵ functional in the Amsterdam density functional package (ADF2014).³⁶ Relativistic corrections were introduced by the scalar-relativistic zero-order regular approximation (ZORA).³⁷ A triple- ζ plus one polarization function basis set³⁸ was used on all atoms. For non-hydrogen atoms, a small relativistic frozen-core potential was used. Solvent effects were introduced using the continuous solvent model (COSMO) with Allinger radii and with water as the solvent.³⁹⁻⁴² Vibrational frequencies were calculated to confirm the nature of the optimized stationary points. A different approach was used for the full cluster optimizations (different code and different density functional) because these calculations are very expensive and the PBE calculations are less computationally demanding than the B3LYP calculations.

⁷Li NMR chemical shift calculations were performed on both the optimized truncated clusters and the full cage models, using the B3LYP/6-31G(d,p)&SDD method with SMD water solvent model, using the Gaussian 09 software,⁴³ and the Gauge-Independent Atomic Orbital (GIAO) method.⁴⁴ The chemical shift δ is calculated by taking the difference of the chemical shielding of a reference sample (σ_{ref}) and the shielding of the cluster under study (σ). For these calculations, the reference chemical shielding (σ_{ref}) of 91.0 ppm is used for Li^+ in water solution, as computed with *ab initio* molecular dynamics by Alam *et. al.*⁴⁵

5.4 Experimental Results

Solid-state ^7Li MAS NMR spectra of the Li- U_{24} -CTA (Figure 2A) show both a resonance close to $\delta = 0$ ppm consistent with hydrated lattice lithium, and a resonance near $\delta = -10$ ppm, consistent with encapsulated Li environment.¹⁸ The appearance of both internal and external Li environments for these Li-CTA precipitates suggests that during the precipitation process, there is incomplete exchange of Li for the surfactants. However, this Li was removed by extensive washing, prior to compositional analysis and solution NMR studies. The ^1H - ^7Li CP (cross polarization) NMR spectra (Figure 2A) selectively enhances the encapsulated Li environment ($\delta \sim -10$ ppm) as expected for a Li inside the U_{24} capsule with reduced mobility and correspondingly increased dipolar coupling to nearby protons. While subtle, differences in the CP contact time resulted in chemical shifts of the broad resonance for the encapsulated species shifting from $\delta \sim -12$ ppm at shorter contact times to ~ -10 ppm at CP > 1 ms. This result reveals that the encapsulated ^7Li NMR resonance is produced by a distribution of different unresolved Li environments, and supports the NMR computational results described below (Section 3.2). There is a very minor ($\sim 2\%$) unidentified Li environment at $\delta = -5$ ppm, and it is enhanced during CP. This -5 ppm peak suggests there remains a more hydrated impurity phase. In fact, -5 ppm is a similar chemical shift as the average of lattice Li exchanging with encapsulated lithium in the previously reported solid state ^7Li MAS NMR of Li- U_{24} .¹⁸ The 2D ^1H - ^7Li NMR heteronuclear (HETCOR) correlation spectrum (Figure 2B) shows a small correlation (due to the reduced dipolar coupling from dynamic averaging the external ^7Li ~ 0 ppm) associated with bridging hydroxyls ($^1\text{H} \sim +9.8$ ppm) of the U_{24} capsule. This is expected, because the hydroxyls point outside the capsules, per computational studies.¹⁰ Additionally, in the ^1H - ^7Li 2D HETCOR experiment the low frequency encapsulated Li resonance is actually the overlap of two different Li environments; one in contact with the $\text{N}(\text{CH}_3)_3^+$ headgroup of the surfactant ($\delta(^7\text{Li}) = -9.8$ ppm, $\delta(^1\text{H}) = 4.1$ ppm) and the Li coordinated with encapsulated water ($\delta(^7\text{Li}) = -9.4$ ppm, $\delta(^1\text{H}) = 9.5$ ppm). The hydrated Li environment at $\delta(^7\text{Li}) \sim 0$ ppm does not reveal any correlation peaks in the 2D HETCOR consistent with the reduced ^1H - ^7Li dipolar coupling as previously noted.¹⁸

A.



B.

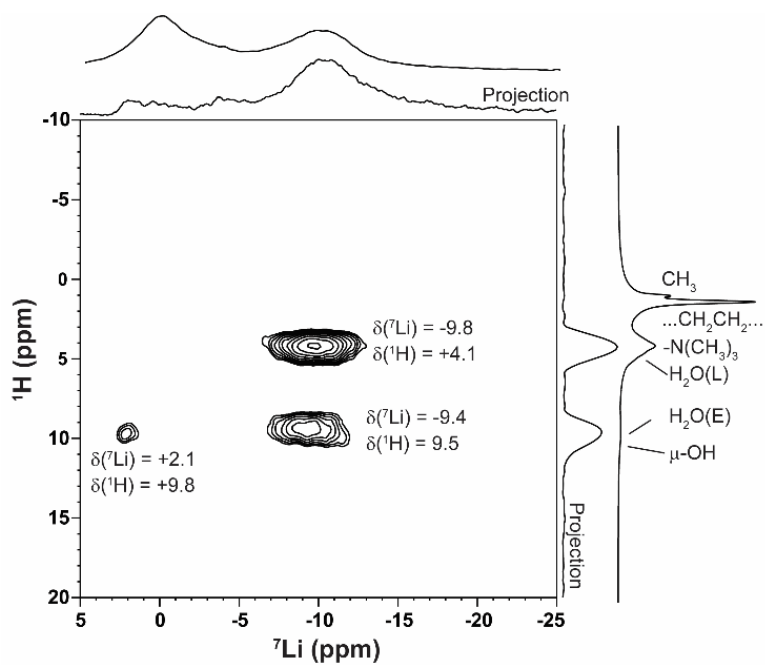


Figure 5.2 A. Solid state ^7Li MAS and CPMAS NMR spectra for the U_{24} -CTA precipitate. **B.** 2D ^1H - ^7Li HETCOR correlation experiment.

Recent computational and experimental studies of interactions of alkylammoniums with Mo-keplerates (also with a capsule topology) showed that alkylammoniums ‘plug’ the pores of the capsule by sitting in the middle of the face.⁴⁶ We expect the cationic surfactants (CTA⁺) to associate in a similar way for U₂₄, creating a hydrophobic shell and preventing Li from escaping the capsule. Compositional analysis (ICP-OES) of digested **Li-U₂₄-CTA** following extensive washing with water, gave concentrations of [Li] mM = 358.146 mM +/- 3.820 (as standard error); and [U] mM = 1553.796 mM +/- 36.062 (as standard error). Comparing results we find a U:Li ratio of 4.338 or about 11 Li ions per U₂₄ cluster. Reported U₂₄ cluster structures with all alkalis located are rare; Li₁₈[K₈Li₄(OH)₆][UO₂(O₂)(OH)]₂₄·76H₂O¹⁸ is one such example containing twelve encapsulated alkalis and a total of 18 encapsulated species (including the hydroxyls). Therefore, 11 Li-cations plus 5-10 water molecules encapsulated in U₂₄ is consistent with prior structural information. We would expect the Li-cations that show correlation with ammonium methyl groups of the surfactant molecules in the HETCOR experiment are closest to the square and/or hexagonal windows, almost exiting the capsule. Conversely, we expect the Li-cations that correlate with encapsulated water are further inside the capsule, with some bonded water molecules. As an initial approximation based on the HETCOR experiments, we argue that the two different, approximately equal concentration, solid state ⁷Li MAS NMR resonances observed can be assigned to Li environments associated with the square face ($\delta = -9.4$ ppm) and the hexagonal face with CTA⁺ plugging the pore ($\delta = -9.8$ ppm). We also note that two distinct resonances in the solid state ⁷Li MAS NMR (encapsulated and external lattice) at room temperature differs from previously reported analysis of the inorganic Li-U₂₄.¹⁸ In the inorganic phase, the encapsulated Li could only be distinguished from the lattice Li below 308K with a reduced exchange rate (<8000 kHz). In the current **Li-U₂₄-CTA** phase, we can conclude the following: 1) There remains a hydrated Li environment, exterior to the U₂₄ capsule, suggesting that replacement by cationic surfactants was not complete during this rapid precipitation method. 2) The exchange rate between encapsulated and free lithium in **Li-U₂₄-CTA** is significant slowed in comparison to the inorganic Li-U₂₄, likely due to the trimethyl ammonium surfactant heads blocking the capsule faces, as suggested by the HETCOR experiment.

We exploit the cluster’s open cage geometry and strong uranium scattering with small-angle X-ray scattering (SAXS) to determine size and shape information of clusters in various solvent media. Comparison of X-ray scattering curves of the aqueous solution to those simulated

from the solid-state structures show excellent agreement out to three oscillations, indicating monospecific solutions (Figure S1). The distinct oscillations arise from the core-shell structure, small differences in intensity in the oscillatory region ($q > 1.0 \text{ \AA}^{-1}$) arises from imperfect scaling and background subtraction of solvent scattering that is dominant in this region. Figure 3 shows the SAXS of Li-U₂₄ clusters in aqueous solution and **Li-U₂₄-CTA** in kerosene-hexanol solution, before and after excess washing. Comparing experimental SAXS data, it is shown that the Li-U₂₄ is retained in the precipitated CTA-encapsulated species when dissolved in organic solvents. Size distribution analysis (Figure S1) of the various Li-U₂₄ species shows Gaussian curves representing specific particle sizes, attributed to the scattering profiles of each SAXS curve. From the initial scattering data and size distribution analysis, we can see the crude Li-U₂₄-CTA has some polydispersity, showing multiple-sized species in the solution. These populations probably represent dimers and trimers of surfactant encapsulated capsules, associated by interdigitation of the surfactant tails. The presence of larger species is visually evident in the scattering curve (Figure 3) by the shift of the Guinier region to lower- q , relative to the pristine aqueous solution. With washing with water, these aggregates are no longer obvious. This suggests it is the presence of excess surfactant that promotes aggregation. Pair distance distribution function (PDDF) model fits of Li-U₂₄ and Li-U₂₄-CTA after the washing steps (Figure 3) both are consistent with a core-shell geometry with lower electron density in the core, indicated by the shoulder on the left. Notably, this shoulder is more prominent for the aqueous phase, indicating a less dense core. This is consistent with the high mobility of the Li and aqua species that exchange between the solvent and capsule in the aqueous solution. The aqueous Li-U₂₄ is modeled to fit a radius of gyration (r_g) of 6.541 Å with a maximum linear extent (max_{ext}) of 16.250 Å, matching the solid-state structure of a U₂₄ capsule with a diameter of 16.2 Å.² The Li-U₂₄-CTA washed sample is modeled to fit a radius of gyration (r_g) of 7.187 Å with a maximum linear extent (max_{ext}) of 22.167 Å. Moreover, there is a shoulder to the right, indicating a shell of lesser density. This shell, as well as the expanded size is due to surfactant heads associated closely with the uranyl capsule. On the other hand, we do not distinctly observe surfactant tails in the SAXS analysis, because they have poorer contrast with the solvent, and are less densely packed, further from the capsule.

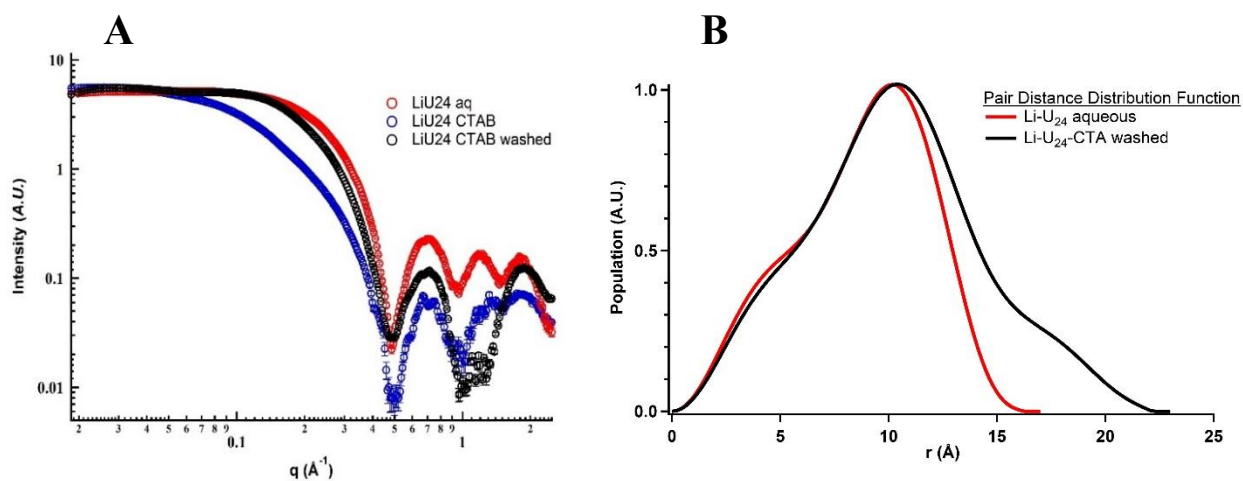


Figure 5.3 Comparing experimental SAXS data of aqueous Li-U₂₄ and Li-U₂₄-CTA (A). Pair distance distribution function (B) of the SAXS data shows the average radius of gyration (r_g) of (Li-U₂₄ aqueous (red) $r_g = 6.541 \text{\AA}$; Li-U₂₄-CTA washed (black) $r_g = 7.817 \text{\AA}$) and maximum linear extent (max_{ext}) in solution (Li-U₂₄ aqueous (red) $\text{max}_{\text{ext}} = 16.250 \text{\AA}$; Li-U₂₄-CTA washed (black) $\text{max}_{\text{ext}} = 22.167 \text{\AA}$) of particles. The obliteration of the second oscillation for Li-U₂₄-CTA-washed is owed to interference by a peak from the surfactant molecules, and the imperfect background subtraction that results from this.

In contrast to the solid-state NMR, the solution ^7Li NMR spectrum of Li-U₂₄-CTA dissolved in kerosene-hexanol (Figure 4A) shows no evidence for the resonance for a hydrated Li environment ($\delta \sim 0$ ppm), or the Li in exchange between encapsulation and an un-encapsulated hydration sphere ($\delta \sim -5$ ppm). Instead, two distinct sharp resonances at $\delta = -10.7$ and -11.5 ppm are observed, and are both assigned to U₂₄-encapsulated Li environments, consistent with the solid state ^1H - ^7Li NMR HETCOR experiments described above. The narrow (FWHM = 40.60 Hz) and well-resolved peaks was a surprising result, unprecedented for encapsulated alkalis that are usually broadened due to exchange with free species in solution, and/or reduced dynamics in the confined capsule space. Prior studies⁴⁷ of surfactant-encapsulated polyoxometalates or clusters suggest their state in solution is as represented in Figure 4B with the cationic surfactant heads surrounding the anionic clusters.

Assessing these data described above, we tentatively offer the following explanations for the origin of the two narrow solution ^7Li NMR resonances. First, the trimethylammonium headgroups and hydrophobic-surrounding organic media keep the Li from escaping the U₂₄ capsule. Since there are ~ 11 Li⁺ inside each cage, inter-cation electrostatic repulsion probably reduces the exchange rate between these different encapsulated environments which was found to be < 150 Hz (*i.e.* the NMR time scale of the resonance separation). Finally, we do not expect the entire **Li-U₂₄-CTA** assembly to undergo rapid tumbling in solution that would lead to the line narrowing. However, we can envision the U₂₄ capsule with its encapsulated species rotating rapidly within the hydrophobic shell. Moreover, electrostatic repulsion between Li⁺ and CTA⁺ might drive this rotational motion.

Variable temperature solution ^7Li NMR experiments of **Li-U₂₄-CTA** dissolved in kerosene (Figure 4B) confirmed that one origin of the extremely narrow peaks at room temperature is the lack of exchange between the two observed Li-positions within the capsule that leads to exchange broadening. Increasing the sample temperature increases the exchange rate between these two Li environments leading to dynamic averaging and peak coalescence at 85°C. Upon further inspection of the data, peak integration at temperatures below coalescence shows a consistent 1:1 ratio of Li ions at each peak position. Plotting the averaged peak position along the temperature range (Figure S2) shows a linear trend consistent with a pure dynamic change coalescence system with no preferred binding site. Simulated ^7Li NMR data and Eyring

plots (Figure S2) reveal an exchange rate of ~ 250 Hz and a ΔG_{298K} of exchange equal to 64.9 (kJ mol⁻¹).

Further experimentation was done by contacting the **Li-U₂₄-CTA** organic solution with pure water and aqueous LiCl solutions (0.05M and 0.1M) to see the effect on the NMR spectra (Figure S3). Pure water contact is a way to remove/wash Li ions out of the system, resulting in a single narrow peak at $\delta = -11.4$ ppm, suggesting experimentally that the most shielded Li-peak corresponds to a more sterically isolated environment similar to a Li-U₂₄ cluster square face. Introduction of excess Li into the system with LiCl solution contact reveals a single broadened Li-peak shifted downfield, increasing LiCl concentration shifts further downfield ($\delta_{0.05M} = -10.6$ ppm and $\delta_{0.1M} = -9.75$ ppm) towards the standard exterior/aqueous Li-peak at $\delta = 0$. This suggests encapsulated Li⁺ is exchanging with external hydrated Li⁺, as was observed in aqueous solution.

Solid-state structures of uranyl capsules that identify encapsulated Li sites and coordination geometries provide a valuable starting point for the computational studies. Because Li is both disordered and has low X-ray scattering power, not many coordination sites have been identified in reported structures. In the original **Li-U₂₄** structure,² Burns located Li below the square face, bonded to the four inward-pointing yloxos of this face, and this continues to be the most frequently observed coordination environment in many unpublished structures.⁴⁹ In the same structure, Li coordinates under the hexagonal face, but offset from the center. This octahedrally coordinated Li is bonded to the cage via a bridging hydroxyl, a bridging peroxo, and two yl-oxos, in addition to two water molecules. Nyman et al. reported Li located in a different position in the square face.¹⁹ In this structure, Li bonds to the bridging peroxides of the square face, and therefore sits further from the center of the capsule. In **U₆₀**, a much larger cage, Burns employed neutron diffraction to identify encapsulated Li, tetrahedrally bound to four water molecules.²⁰ This Li site is not associated with the uranyl cage. However, we do not necessarily expect this coordination environment inside the smaller confines of **U₂₄**.

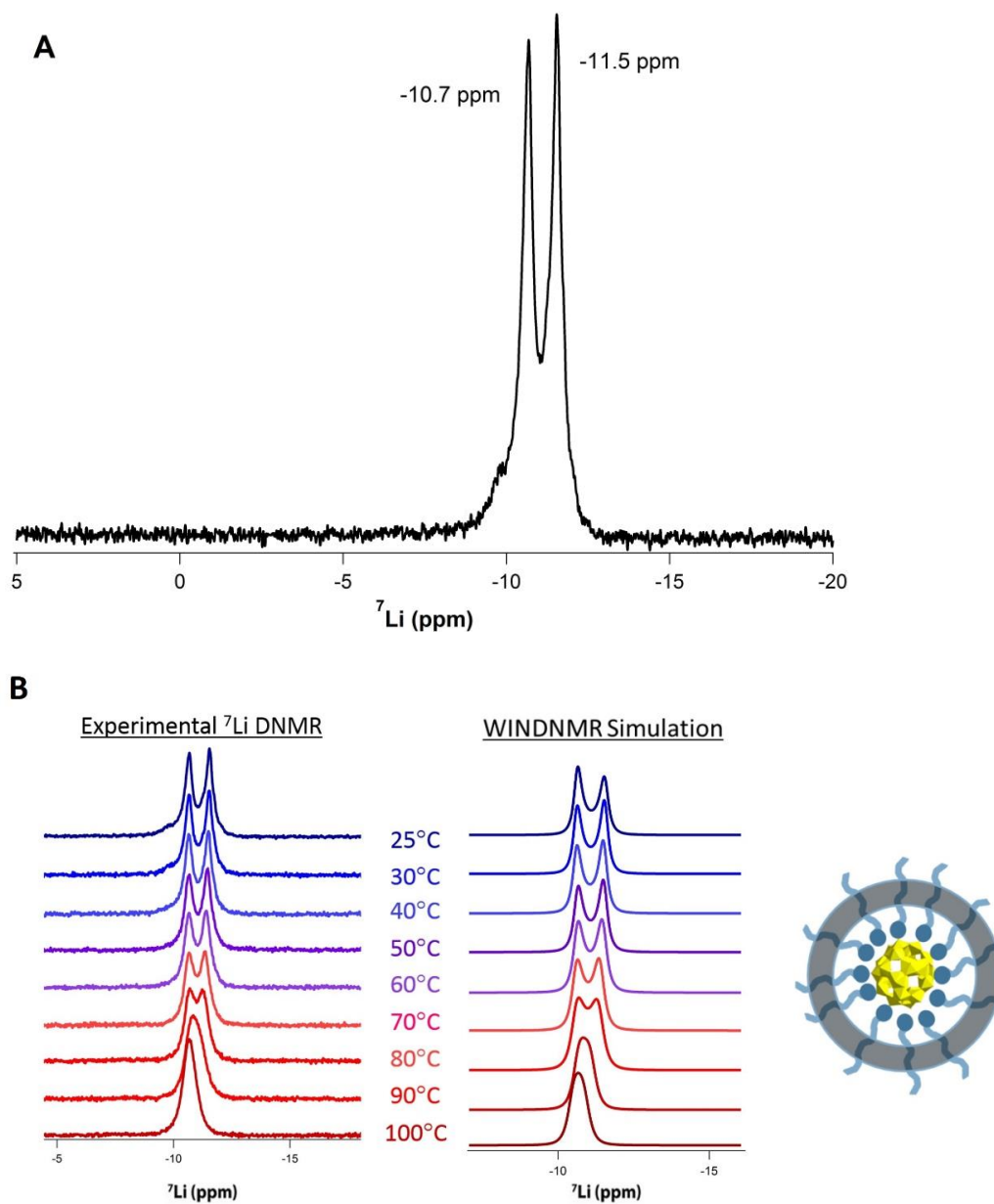


Figure 5.4 Nuclear magnetic resonance (NMR) spectra of Li-U₂₄ surfactant encapsulated species. (A) NMR experiment of Li-U₂₄-CTA at 25°C. The hydrated Li resonance at $\delta = 0$ ppm was not present in **A**, while two distinct encapsulated resonances at -10.7 ppm and -11.5 ppm were observed. (B) Variable Temperature NMR data from 25°C to 100°C shows exchange between the two Li ion environments with a coalescence temperature of 85°C. WINDNMR simulations are included.

5.5 Computational Results

5.5.1 Cluster Model

We initially explored the possible interaction sites by utilizing the square, hexagon, and square-hexagon models, which have been truncated from the optimized U_{24} cluster structure. The concave side of the models is the inside of the cage and the convex side is the outside of the cage (Figure 5.E).

The constrained optimization of the Li^+ -square model resulted in three possible binding sites, Figure 5. In Site 1 (Figure 5.A), the internal Li^+ is below the center of the square face (sq-1, $\delta(Li) = -10.9$ ppm). In Site 2, (Figure 5.B) the external Li^+ is located above the square face center (sq-2, $\delta(Li) = +4.5$ ppm). In Site 3, (Figure 5.C) the external Li^+ is bonded to the bridging peroxides (sq-3, $\delta(Li) = -1.5$ ppm). In the sq-4 structure (Figure 5.D), two Li^+ ions interact with the square model, one above (external) and the other under (internal) the square face, with respective chemical shift of 3.5 ppm and -12.4 ppm. We noticed that, in terms of the square models, when Li^+ coordinates at the concave side of the square building block, (i.e. inside the cage, site 1), the chemical shift of the Li^+ cations $\delta(Li)$ tends to be more negative; however, Li^+ cations at the convex side (outside the cage, site 2 and 3) give more positive chemical shifts. Experimentally the dominant 7Li NMR chemical shifts in both solution and in the solid state are between δ -10 and -12 ppm, such that the square-model calculations support the assignment of these Li environments as encapsulated and not outside or at the surface of the U_{24} cage. The sq-4 structure also suggests that multiple Li interactions can determine the final cluster structures and the corresponding 7Li chemical shifts. By simply adding to our cluster model a second Li ion produced a $\Delta\delta$ of -1.5 ppm for the encapsulated Li and a $\Delta\delta$ of -1.0 for the external Li environment. The complexity of the multiple interactions and structural changes certainly affect the observed 7Li NMR values.

Studies on hexagon models also support that the Li^+ cations are encapsulated inside the U_{24} cage. The constraint optimization of one Li^+ in the hexagon model resulted in five different possible binding sites, shown in Figure 5.E-H. Site 1 and 2 are inside the cage, that is the Li^+ ion binds to the uranyl-O atoms that are under the peroxide bridge (hex-1, $\delta(Li) = -8.5$ ppm, Figure 5.E) and that under the hydroxide bridge (hex-2, $\delta(Li) = -8.7$ ppm, Figure 5.F). Sites 3 and 4 are outside the U_{24} cage, respectively on top of the peroxide bridge (hex-3, $\delta(Li) = -1.6$ ppm, Figure

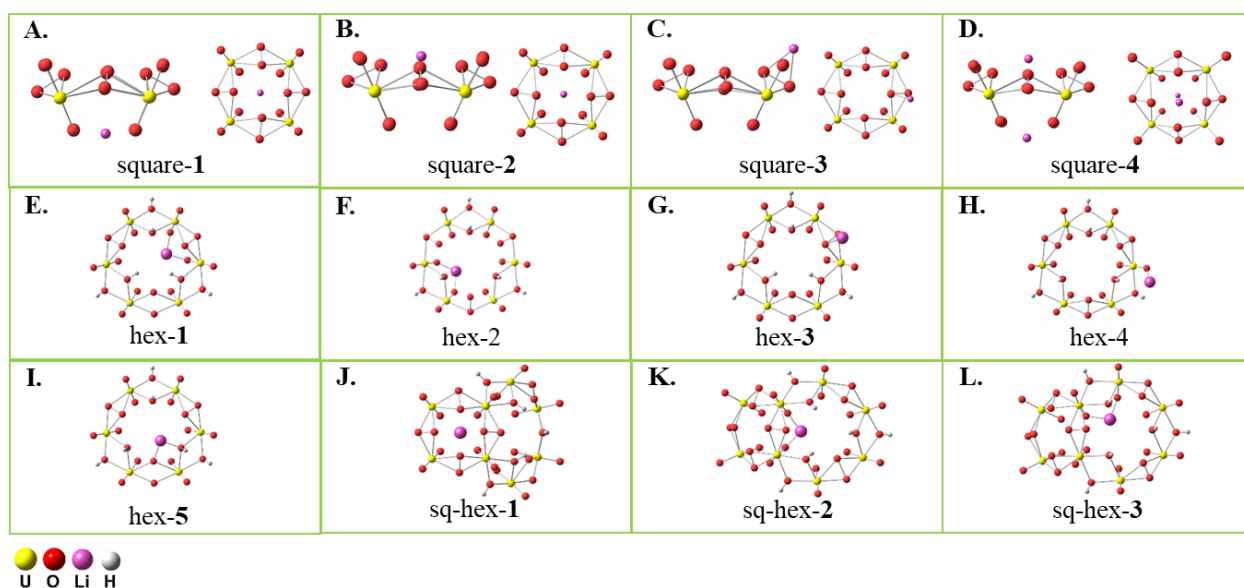


Figure 5.5 Structures of cluster models with different Li^+ cation coordination environments to the square (A-E) to the hexagon (E-I; see also Figure S4 for sideview), and to the square-hexagon model (J-L).

5.G) and on top of the hydroxide bridge (hex-4, $\delta(\text{Li}) = -5.5$ ppm, Figure 5.H). Site 5 is on the surface of the cage, where the Li^+ coordination bridges one peroxide-O atom and one hydroxide-O atom (hex-5, $\delta(\text{Li}) = -2.2$ ppm, Figure 5.I). Among the five binding sites, only the Li^+ ions located inside the cage (site 1 and 2) have ^7Li NMR chemical shifts consistent with the experimentally observed values. Among the possible binding models discussed above, in three cases the Li^+ ion is inside the cage, namely in the Li@sq-1, Li@hex-1, and Li@hex-2 cases. To determine the binding preference among these three sites, we considered a square-hexagon model with Li at the three different sites (Figure 5.J-L), and performed a constrained geometry optimization for the three cases. The sq-hex-1 structure, with a single Li^+ located under the square face center, is the lowest in energy, compared to the sq-hex-2 and sq-hex-3 structures, with Li^+ coordinated under the peroxide- and hydroxide-bridge of the hexagon motif, respectively, which are about 13.4 and 16.4 kcal/mol higher in energy, respectively. This result is consistent with earlier studies that showed that the square is the preferred coordination site for a single Li cation.^{2, 13} In going from the square or hexagon model to the square-hexagon model, the chemical shift of Li^+ changes for each binding site. For example, Li@hex-1 has a chemical shift of -8.5 ppm, in comparison to Li@sq-hex-2, with a chemical shift of -9.3 ppm. Both binding sites are under the peroxide bridge. We attribute the differential chemical shifts to the structural change as well as the differential model size and the differential charge of the models. The bare square building block is neutral, whereas the bare square-hexagon model carries a (-2) charge. Therefore, a full cage model seems necessary. We will discuss it in Section 3.2.2. Table S1 lists the chemical shifts obtained using other functionals besides B3LYP, namely PBE0, M06, M06-2X, HSE, CAM-B3LYP. For all functionals the relative chemical shifts of Li are similar. We also noticed that the δLi values decrease as the percentage of HF exchange in the functional increases (Table S1, Figure S5). Based on these tests and earlier studies,⁴⁵ the B3LYP functional provides sufficient accuracy and is selected for further calculations. In the NMR chemical shifts calculations, the implicit solvent model SMD was used to account for indirect solvent effects. Since the organic solvent kerosene was used in the experiment, we performed NMR calculations using various organic solvents, including hexane, hexanol, cyclohexane, and benzene, on the “SMD=water”-optimized structures, and it showed that all these solvents gave similar chemical shifts as using water as solvent (Table S2, Figure S6).

Table 5.1 ^7Li NMR chemical shift δ (ppm) and relative energy E (kcal/mol) of the different cluster models

Square Model					
Label	sq-1	sq-2	sq-3	sq-4	
δ_{Li}	-10.9	4.5	-1.5	-12.4, 3.5	
$E_{\text{rel}}^{\text{a}}$	0.0	18.2	22.6		
Hexagon Model					
Index	hex-1	hex-2	hex-3	hex-4	hex-5
δ_{Li}	-8.5	-8.7	2.2	-1.6	-5.5
E_{rel}	3.3	3.5	0.0	10.7	15.1
Square-Hexagon Model					
Index	sq-hex-1	sq-hex-2	sq-hex-3		
δ_{Li}	-10.6	-9.3	-8.8		
E_{rel}	0.0	13.4	16.4		

^aThe relative electronic energies are compared among the same type of model.

To further test the effect of different solvent models on the position of the Li cations, we optimized the cluster models in hexane and cyclohexanol and calculated the corresponding Li chemical shifts. Structure comparisons show that in the square-models the solvent type has a minor effect. In the hex-model and sq-hex-model, on the other hand, where both Li and H can relax, the solvent has a larger effect on the Li position and chemical shifts. (Table S3) Considering that when Li-U₂₄-CTA is dissolved in kerosene, the organic solvent molecules are likely outside the cage and the water molecules inside the cage, we decided to use water as a solvent in this study to mimic the solution environment.

5.5.2 Full U₂₄ Cage Model

As discussed above and in early studies,^{2, 13} the initial Li cations prefer the square face, giving a total of six Li⁺ inside the U₂₄ cage, denoted as 6Li@U₂₄ and structure **A**, for the sake of discussion. A single point ⁷Li NMR calculation of 6Li@U₂₄ structure gives a single chemical shift of -13.8 ppm, corresponding with these six identical environments. This is significantly different than the sq-1 partial square cluster model which predicted a ⁷Li shift of $\delta = -10.9$ ppm. This first binding site for 6Li@U₂₄ is the inner side of the square face center, denoted as *in-Sq*. Since the experimental ⁷Li NMR spectrum at room temperature shows two resonances, another binding site is expected besides the square face center. Therefore, we tested four more structures, Figure 6, **B-E**, in addition to the *in-Sq* site (1), namely (2) outer side of square-face-center (*out-Sq*), (3) cage center (Cc), (4) inner side of hexagon-face-center (*in-Hex*), and (5) outer side of hexagon-face-center (*out-Hex*).

In structure **B**, one more Li cation is placed at the center of the U₂₄ cage (Cc) and its chemical shift is -18.9 ppm, whereas the other six *in-Sq* Li cations have a chemical shift of -12.5 ppm. Note that a $\Delta\delta = +1.3$ ppm is predicted for the *in-Sq* Li environments when a single Cc Li is added to the cluster. In structure **C**, six more Li cations bind to the outside surface of the square (*out-Sq*) and their predicted chemical shifts are +2.6 ppm. In comparison, the chemical shift of the six *in-Sq* Li cations is -15.8 ppm, corresponding to a $\Delta\delta = -2.0$ ppm change from the 6Li@U₂₄ structure **A**. In structure **D**, eight more Li cations were initially placed inside the U₂₄ cage and coordinated to the hexagon face and optimized. Instead of remaining inside the U₂₄ cage, the eight Li cations prefer to bind to the outside surface of the hexagon face. In this case, the chemical shift for the eight hexagon-face-coordinated (*out-Hex*) Li⁺ is -1.65 ppm and for the

six *in-Sq* Li⁺ is -16.8 ppm ($\Delta\delta = -3.0$ ppm with respect to 6Li@U₂₄). We noticed that, in structures **B**, **C**, and **D**, the chemical shift differences between the two types of Li⁺ environments are 6.4, 18.5, and 15.1 ppm, respectively, which differ greatly from the small experimental difference of 0.86 ppm. Therefore, the simple Li arrangements proposed in structures **B**, **C** and **D** were not sufficient to explain the experimental ⁷Li NMR results. These results also demonstrate that the inclusion of additional Li cations within the U₂₄ capsule have a significant effect on the predicted ⁷Li NMR ($\Delta\delta +1.5$ to -3.0 ppm), and reflect how subtle differences in the coordination environments are reflected in the chemical shifts. There is a general and consistent correlation of increasingly negative shift as the Li cations move towards the center of the capsule. The calculated δ -values most consistent with the experimental chemical shifts correspond with Li⁺-cations bonded to the inside of the capsule.

In the experiment, the U₂₄ cage is surrounded by cation surfactants, so in structure **D** the eight out-Hex Li⁺ cations may be replaced by the CTA⁺. Then, we placed eight more Li⁺ cations under the hexagon face in addition to the 14 Li⁺ cations in structure **D**, with this new structure denoted as **E**. Optimization of structure **E** gave three δ -values corresponding with three Li coordination environments: *in-Sq* ($\delta_{\text{Li}} = -10.5$ ppm), *in-Hex* ($\delta_{\text{Li}} = -9.2$ ppm), and *out-Hex* ($\delta_{\text{Li}} = -0.2$ ppm), where the last binding site is anticipated to be occupied by surfactant. The remaining two types of binding sites, *in-Sq* and *in-Hex*, give rise to a $\Delta\delta$ of ~ 1.3 ppm, in moderate agreement with the experimental $\Delta\delta$ of 0.86 ppm. In structure **A-E**, we considered five types of binding sites: *in-Sq*, *out-Sq*, *Cc*, *in-Hex*, and *out-Hex*. To estimate the preference of these binding sites, we calculated the average contribution of Li⁺ cations to the formation reaction, *i.e.* ΔE_{ave} , via dividing the formation energy (ΔE) by the number of Li⁺ cations in each structure, with more negative ΔE_{ave} indicating stronger binding. In Table 2, we estimate that the binding preference order is *in-Sq* > *out-Sq* > *out-Hex* > *in-Hex*, and *Cc* < *out-Sq*. Between the *in-Sq* and *in-Hex* binding sites in structure **E**, *in-Sq* is more favored. This suggests that, with increasing temperature, the Li@*in-Sq* environment will be able to gain sufficient energy to exchange with to the Li@*in-Hex* site leading to the coalescence at higher temperatures. In brief, the full-cage-model results suggest that the square-face-center and hexagon-face-center are two possible binding sites inside the U₂₄ cage, and that the differential Li NMR can be attributed to these two types of binding sites. Below, we show how a minor perturbation can affect the Li NMR chemical shifts.

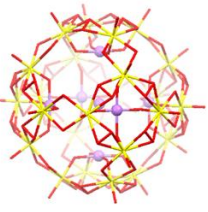
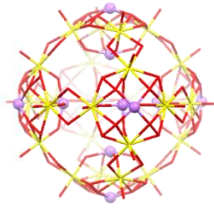
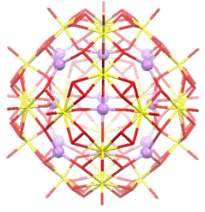
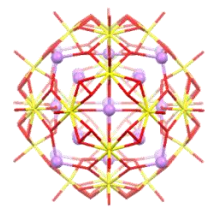
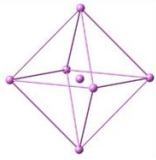
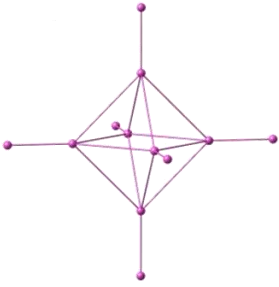
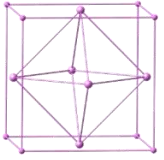
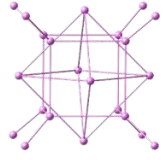
	B	C	D	E
# of Li	7	12	14	22
Full-Cage Structure				
Li cluster structures				
δ_{Li} , ppm ($d_{\text{Li-origin}}$, Å)	Sq: -12.54 (4.07Å) Cc: -18.89 (0.0Å)	Sq: -15.83 (3.80 Å) Sq: 2.65 (7.38 Å)	Sq: -16.79 (3.68 Å) Hex: -1.65 (5.66 Å)	Sq: -10.48 (3.93 Å) Hex: -9.20 (3.90 Å) Hex: -0.22 (6.73 Å)

Figure 5.6 Optimized structures of full-cage models, B – E, and the respective Li cluster structure. Bottom row: chemical shifts of Li cations and their distances from the U_{24} cage origin. Sq is square, Cc is cage center, and Hex is hexagon. Color code: Li, purple; U, yellow; O, red. Hydrogen atoms are omitted for clarity.

Table 5.2 Formation energy (ΔE) and average contribution (ΔE_{ave}) of structure A – E. Energies are in kcal/mol.

	Formation Reactions	ΔE	ΔE_{ave}
A	$6 \text{ Li}^+ + \text{U}_{24}^{24-} \rightarrow [6\text{Li}@U_{24}]^{18-}$	-180.2	-30.0
B	$7 \text{ Li}^+ + \text{U}_{24}^{24-} \rightarrow [7\text{Li}@U_{24}]^{17-}$	-131.0	-18.7
C	$12 \text{ Li}^+ + \text{U}_{24}^{24-} \rightarrow [12\text{Li}@U_{24}]^{12-}$	-241.8	-20.1
D	$14 \text{ Li}^+ + \text{U}_{24}^{24-} \rightarrow [14\text{Li}@U_{24}]^{10-}$	-105.9	-6.6
E	$22 \text{ Li}^+ + \text{U}_{24}^{24-} \rightarrow [22\text{Li}@U_{24}]^{2-}$	-115.0	-5.2

To confirm the hypothesis that ${}^7\text{Li}$ chemical shift is affected by depth of the cation within the capsule, displacement perpendicular to the square face or the hexagon face, (*i.e.* z -direction, Figure.7) was investigated by performing single point NMR calculations as the Li cation moves from the U_{24} cage center to the surface of the square or hexagon. Figure 7.B (blue line) shows the ${}^7\text{Li}$ chemical shift changes as a function of the z -displacement towards the square face. As the Li^+ cation moves from 0 to 3 Å, the Li chemical shift decreases from $\delta = -7.5$ ppm to the minimum at $\delta = -16$ ppm, and then increases to $\delta = +5$ ppm when Li^+ is at 6 Å. The single point energy calculation (Fig. 7.B) shows that a single Li^+ at 4 Å is the energy minimum for the square model, with $\delta = -11.9$ ppm. We noticed that, from the minimum point, if we reduce the displacement of the Li^+ by -0.25 Å, the Li is further shielded by 2 ppm and the relative energy increases by 1 kcal/mol. Meanwhile, if the Li is displaced by $+0.25$ Å, the Li becomes deshielded by 2.5 ppm and the relative energy increases by 1.7 kcal/mol. In short, subtle movement of the Li cation can lead to significant changes in the chemical shift. The trend between the Li chemical shift and the displacement of Li along the z -coordinate is similar for the hexagon as for the square face (Figure 7D). For the hexagon face a minimum $\delta = -12.1$ ppm is found at 2.34 Å, with the Li continue to become deshielded with increasing displacement from the cluster center. The relative energy curve (Figure 7D) for hexagon-face-scan indicates that the energy minimum is at 6.24 Å, which is slightly higher than the plane of six U atoms. This result confirms our earlier finding that Li^+ prefers the *out-Hex* site over the *in-Hex* site, unless the *out-Hex* site is anticipated to be occupied by cation surfactant. A remarkable feature of the relative energy profile of hexagon-face scan is that the energy only changes slightly between 3 and 5 Å from the cage center along the z -direction. Recalling that we determined that the second preferred binding site is the *in-Hex* site at 3.9 Å from the cage center, it is expected that this binding site is more labile than the *in-Sq* site.

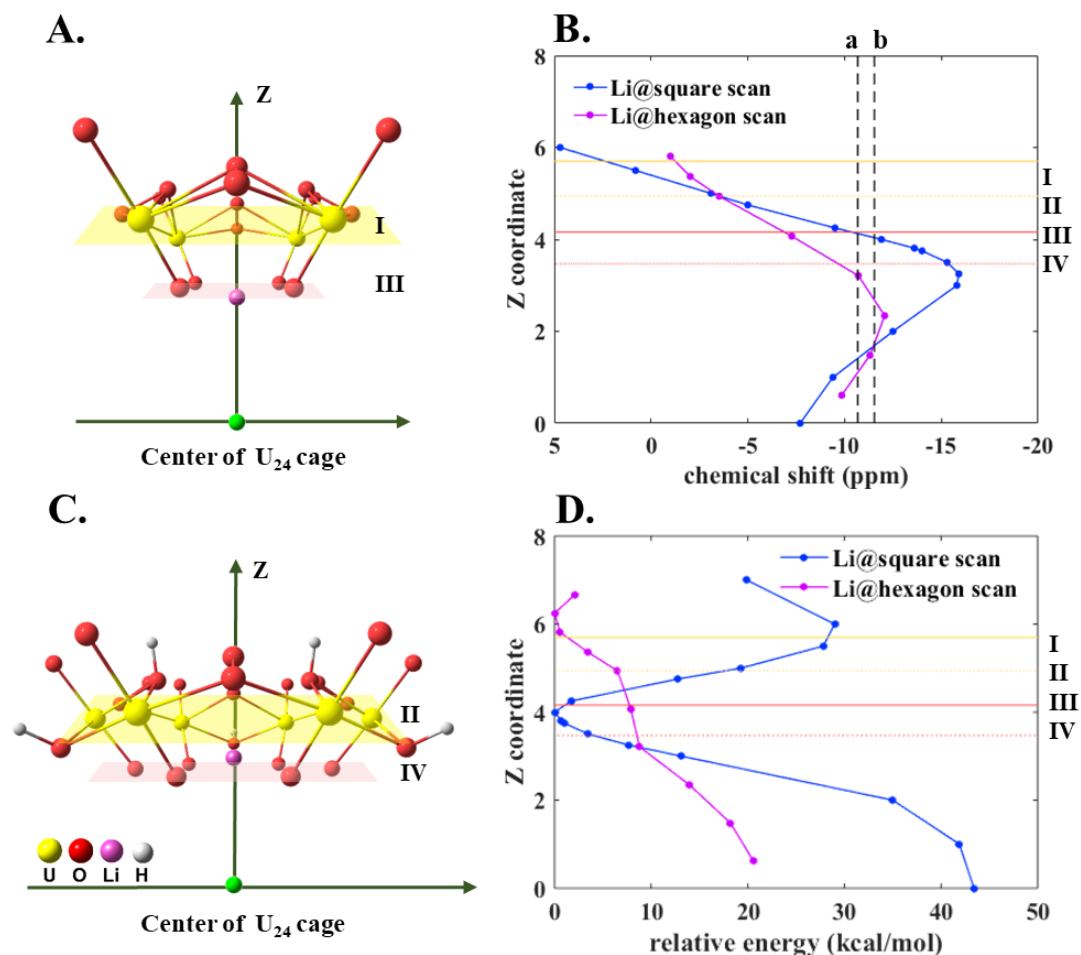


Figure 5.7 Square model (A) and hexagon model (C). The respective Li^+ cation chemical shift as a function of z coordinate and relative single point energy (kcal/mol) as a function of z coordinate for square model (B) and hexagon model (D).

Note: Z-coordinate is in Angstrom. In sub-figure 2 and 4, vertical lines a and b denote the experimental solution 7Li NMR signals of -10.7 and -11.5 ppm, $\Delta\delta = 0.86$ ppm. **I** represents the plane of four U atoms in the square model (5.70 Å). **II** represents the plane of lower layer uranyl O atoms in the square model (4.16 Å). **III** denotes the plane of 6 U in the hexagon model (4.94 Å). **IV** denotes the plane of lower layer uranyl O atom in the hexagon model (3.47 Å). Planes **I** – **IV** are labeled in figure 2 and 4 to guide the eye.

5.5.3 Explicit Water Molecules Studies

The dynamics of the water molecules are also of interest and have been investigated in previous studies of U₂₄ in either aqueous solution or in the solid-state.¹⁸ In the preparation of **Li-U₂₄-CTA**, water molecules are likely trapped in the U₂₄ cage along with the Li cations to complete their coordination sphere. Additionally, the Li cation has the highest hydration energy among alkali cations.⁴⁸ Above we identified association of Li with encapsulated water in the HETCOR experiment. Below, we discuss the effect of including explicit water molecules in the computational models.

The internal cavity has a diameter 9.2 Å and a volume of 408 Å³. We consider each non-hydrogen atom occupies 17 Å³ (an empirical ‘rule of thumb’ from crystallographic studies) then ~24 combined Li-cations and water molecules can fit inside the capsule. For this reason, in addition to the fact that the Li-cations are under-coordinated in all the models described above, we investigated the effect of coordinating water molecules to Li on the calculated chemical shift values. Unfortunately, quantification of water molecules is greatly complicated by the presence of surfactant molecules. Since the inclusion of explicit water molecules adds considerable complexity, we limited our study to square cluster model and five water molecules.

We built two sets of structures, as shown in Figure 8. In the top structures, one water molecule lies above the Li cation and below the plane of four U atoms. In the bottom set, all water molecules lie below the Li cation. Although the top water molecule forms hydrogen bonds with the peroxide-bridge oxygen atoms, due to the steric effect, the top set is about 100 kcal/mol higher in energy than the bottom set (Table S6). The energy differences indicate that when the Li cation binds to the square center, it is more likely that water molecules are coordinated internally (*i.e.* closer to the cage center) rather than from the top. Therefore, we will consider the coordination motif of the bottom set (Figure 8) in the following discussion.

In the square model, with coordination by different numbers of water molecules, the optimal position of Li⁺ persists in the center of square face, with the water molecules pulling the Li towards the cage center. (The only exception is 2b where the Li cation is below one peroxide bridge.) The distance between the Li cation and the cage center slightly decreases from 4.0 to ~3.6 Å as the number of water molecules (n) changes from 0 to 5. Correspondingly, the ⁷Li NMR chemical shift changes from -10.9 ppm ($n = 0$) to -12.5 ($n = 1$), -12.3 ($n = 3$), and -12.1 (n

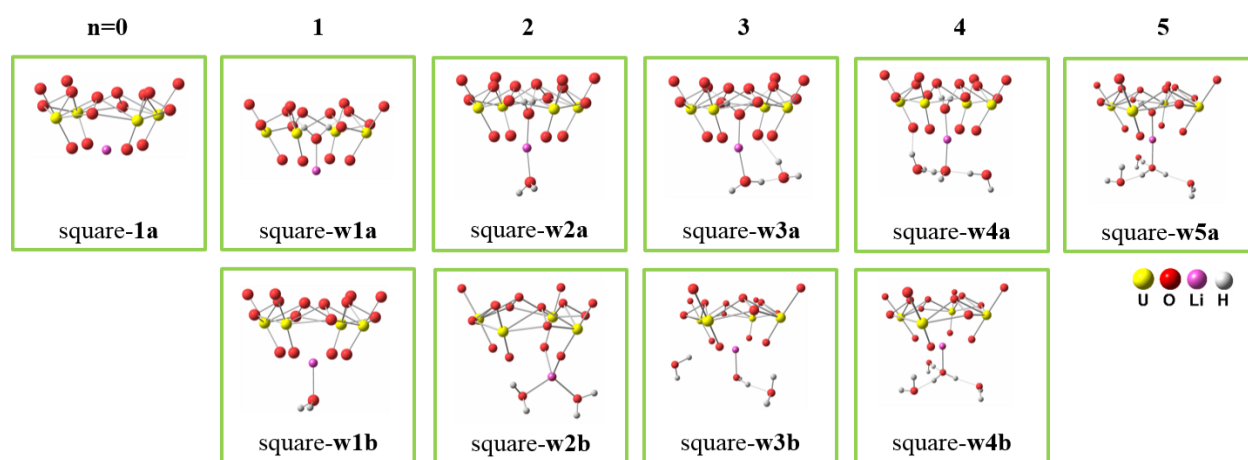


Figure 5.8 Structures of square model with solvated Li^+ ion.

= 4) ppm, respectively. The effects of H₂O molecules are two-fold: they change the position of Li⁺ within the cluster, and they also impact the Li chemical shift directly. For these different models, the Li chemical shift difference between non-hydrated ($n = 0$) and hydrated ($n > 1$) Li⁺ ranges from 1.2 to 1.6 ppm, which is comparable to the experimentally observed solution ⁷Li NMR chemical shift difference of 0.86 ppm at room temperature. Changes in the Li hydration with temperature may also help explain the dynamics observed in the VT NMR experiments (see earlier discussion).

5.6 Conclusion

The surfactant-encapsulated uranyl capsules prepared here provide opportunity to study the behavior of spatially-confined hydrophilic species such as lithium and water, surrounded by a hydrophobic medium. Two distinct coordination environments for lithium inside of the 16 Å diameter U₂₄ cage are observed by both solid-state and solution ⁷Li NMR. The barrier for exchange of these sites is quite high, as indicated by the large, positive exchange energy. We hypothesize the cations have minimal space to move within the capsule, and there is likely great repulsion between the ~11 encapsulated Li-cations per cage. Computation of possible Li-coordination sites within the capsule and their corresponding ⁷Li chemical shifts all showed that the chemical shift becomes more negative as the Li-cation moves from the edge to center of the uranyl capsule. The chemical shift calculations and calculated energies of the possible coordination sites indicated the Li-cations preferably bond to the inwardly-pointing capsule oxo ligands; and coordination under the square face is favored over coordination under the hexagonal face. Finally, we still do not understand the origin of the unusually sharp ⁷Li NMR peaks, which will be probed by future computational studies. One plausible explanation that we will explore is rapid rotation of the entire capsule within the surfactant shell, which may be driven by repulsion between the surfactant cationic-heads and the Li⁺ cations in the open faces of the capsule.

5.6 Acknowledgements

The synthesis, solution NMR and SAXS characterization, compositional analysis, and computational studies performed at OSU, NDU and UMN were performed as a part of the Materials Science of Actinides, an Energy Frontier Research Center, funded by the Department of Energy, under award number DE-SC0001089. The solid-state NMR was performed at Sandia

National Laboratories, which is a multi-mission laboratory managed and operated by National Technology and Engineering Solutions of Sandia, LLC., a wholly owned subsidiary of Honeywell International, Inc., for the U.S. Department of Energy's National Nuclear Security Administration under contract DE-NA0003525. Jing Xie thanks Pere Miró and Bess Vlaisavljevich for helpful discussion.

Chapter 6

Synthetic Pathways and Exfoliation of Uranyl Phosphate Layered Materials

Harrison A. Neal, Karoly Kozma, and May Nyman

Publication to be submitted

6.1 Abstract

Studies on uranium mineral chemistry is imperative to understand how uranium compounds interact in nature and on the back end of the nuclear fuel cycle. With a focus on layered uranyl phosphate minerals, a reliable and updated synthetic pathway is outlined and intercalation of organic molecules into the structure is described. Precipitate of uranyl phosphate mineral chernikovite is obtained by the combination of aqueous uranyl nitrate and ammonium phosphate dibasic and confirmed using Powder X-ray Diffraction (PXRD) and EDX composition analysis. This opposes literature methods of using phosphoric acid as the phosphate source as the synthesis is poorly described and chernikovite was found to be soluble in acidic pH. Chernikovite has a 2-D sheet-like layered structure of uranyl phosphate with interlayer spacing in the (001) plane. Suspension of chernikovite in a solution of octylamine and DMSO allows for the intercalation of octylamine molecules into the structure, resulting in successful delamination of the structure. Infrared and Raman peak shifts allow for monitoring the intercalation of octylamine while PXRD and PDF investigate the structural changes that take place in the material. Electron microscopy imaging shows the powder morphology and visual structural changes that occur before and after intercalation. Studies of intercalation in uranyl mineral systems sheds light on how these sheet-like structures are held together and comparisons can be made to transition metal chalcogenide (TMC) systems with similar behavior.

6.2 Introduction

Uranium compounds are commonly known for natural radioactive properties and application in the nuclear fuel cycle in the form of a fissionable oxide fuel. While UO_2 , UO_3 , and mixed oxide fuels are interesting from a nuclear perspective, the chemistry and structure of oxides of uranium are well understood for industrial application. In contrast, chemistry of spent fuel, legacy waste, and naturally occurring uranium minerals are of interest for study. The introduction of phosphate as tributyl phosphate (TBP) ligands for back-end uranium extraction provides an important consideration in understanding chemistry of uranium compounds in the nuclear fuel cycle.¹

Naturally occurring minerals of uranium with an array of compositions, structures and material properties²⁻⁴ have implications for phases of back-end spent nuclear fuel and legacy wastes. Common structures consist of phosphates, vanadates, silicates, titanates, etc. with combinations of alkali metal ions, all present within the nuclear fuel cycle, fission products and the environment.⁵ Specific study of uranyl minerals such as studtite, a naturally occurring peroxide containing uranyl compound, have led to a new field of research on aqueous uranyl peroxide cluster.^{6,7} Structural properties of the studtite mineral are still present in the uranyl peroxide cluster motif. Bent uranyl-peroxo-uranyl bridging throughout the studtite structure (a zig-zag feature) is exhibited in the sphere-like curvature of the cluster cages and passivated 'yl' oxygens in both axial positions about the uranium atoms are exhibited in the hollow cluster core.

Taking advantage of weak interlayer dispersion interactions allows for intercalation of molecules to delaminate/exfoliate single sheets of a uranium mineral. Exfoliation of 2D layered sheet-like material allows for exploration of possible chemistries left unstudied within uranium minerals such as metaschoepite⁸ $[(\text{UO}_2)_4\text{O}(\text{OH})_6]$ and chernikovite⁹ $[(\text{H}_3\text{O})_2(\text{UO}_2)_2(\text{PO}_4)_2]$ (2D sheet-like structure).

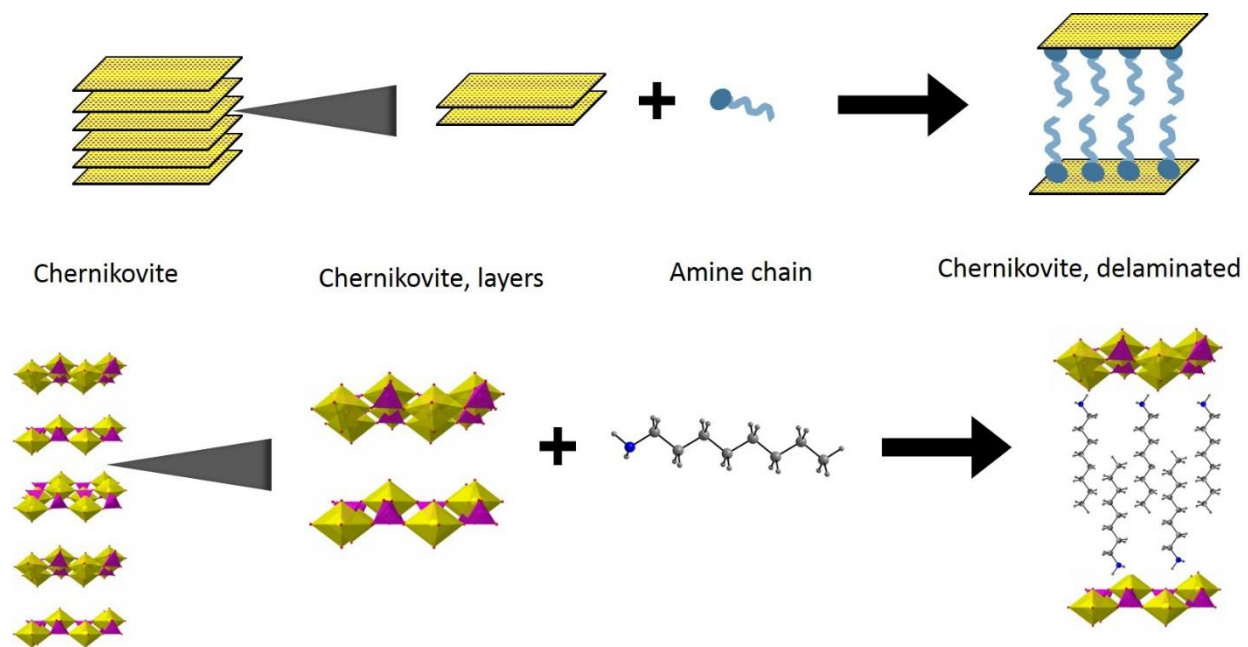


Figure 6.1 Graphical representation of delamination mechanism for the layered chernikovite structure. Intercalation of amine chains into the structure would expand the (001) plane.

A similar approach has been previously established for transition metal chalcogenide (TMC) systems.¹⁰ Amine intercalation in the TiS system shows an interlayer distance dependence on amine chain length and the time the layered material is exposed to the amine solution.¹⁰ **Figure 6.1** shows a visual representation of the successful delamination method with the compatible uranyl phosphate layered material using Lewis base intercalates described in this work.

6.3 Experimental

Caution: Although isotopically depleted uranium was used in this study, precautions for handling toxic and radioactive materials should be followed.

Chernikovite $[(\text{H}_3\text{O})_2(\text{UO}_2)_2(\text{PO}_4)_2 \cdot 6\text{H}_2\text{O}]$ was prepared by combining a 0.166M solution of uranyl nitrate (0.5g in 6mL) and a 0.166M solution of ammonium phosphate dibasic $[(\text{NH}_4)_2\text{HPO}_4]$, forming a 1:1 ratio as described in the chemical formula. Precipitate forms immediately but the solutions were stirred to ensure complete reaction. The solid was collected by centrifugation and dried in a vacuum oven overnight. The chernikovite solid was suspended in water and heated at 180°C for 3 days under hydrothermal conditions. The dry product was characterized using Raman (**Figure S3.1**) spectroscopy and powder X-ray diffraction.

Chernikovite was delaminated by combining dry solid chernikovite (500 mg) to a mixture of octylamine (3.02 M) in DMSO (10.0mL). The solid chernikovite does not dissolve but the suspension is stirred overnight to ensure complete intercalation of octylamine into the layered chernikovite structure. The sample was centrifuged to separate out solid product. Residual DMSO solution is decanted and the solid delaminated chernikovite is dried in the vacuum oven. The dry product was characterized using Raman spectroscopy (**Figure S3.1& Figure S3.2**), infrared spectroscopy, and powder X-ray diffraction.

6.4 Results and Discussion

Previous synthetic methods^{9,11} report chernikovite was precipitated by combining uranyl nitrate and phosphoric acid in a 1:1 ratio of unknown concentrations of reagents. From experimental determination uranyl phosphates are soluble in most concentrations as the solution is at a pH below 1.0. The addition of base (LiOH or NaOH) yields a precipitate analog of the chernikovite structure (**Figure S3.3**) at pH 5.0. To try minimizing impurities we utilized ammonium phosphate dibasic $[(\text{NH}_4)_2\text{HPO}_4]$ as the phosphate source to synthesis chernikovite. XRD characterization reveals a pattern matching with that of literature chernikovite. The Bragg peak at $2\theta = 9.78^\circ$ ($d = 9.03\text{\AA}$) corresponds to the (001) lattice plane, or the interlayer distance of the 2D uranyl phosphate sheets (**Figure 6.2**). Solubility studies of synthesized chernikovite in acid showed that pristine chernikovite dissolved in phosphoric acid and nitric acid concentrations above 50mM.

Intercalation experiments consisted of contact with nitrate salts of Li^+ , Na^+ , TBA^+ , etc., surfactant molecules (nonyltrimethylammonium bromide) and neutrally charge amines (butylamine, hexylamine, octylamine, etc.). Initial results suggests that protonation of the phosphate ligand is what drives interaction between the mineral layers and the amine head group. Analogs were synthesized of chernikovite containing these ions using bases so lack of intercalation capability was surprising (**Figure S3.3**). Further investigation showed that neutrally charged amines significantly influenced the interlayer distance suggesting that uranyl phosphate sheets are held together with weak interlayer van der Waals interactions. Previous studies on transition metal chalcogenide (TMC) systems report the interaction between the amine and TMC layers is a Lewis acid/base complexation¹⁰. This suggests that the uranyl phosphate sheet has Lewis acid character, due to the protonated phosphate ligands. XRD analysis allows for investigation of the (001) interlayer distance given by peak 1 of the pattern (**Figure 6.2**). Shift of the (001) to lower 2θ is representative of delamination and layer separation. Shifts were seen with hexylamine and octylamine samples, the octylamine being the most significant change. Infrared spectra of the solid chernikovite samples shows the presence of C-H, N-H, and C-N stretches consistent with an amine present in the delaminated sample (**Figure 6.3**).

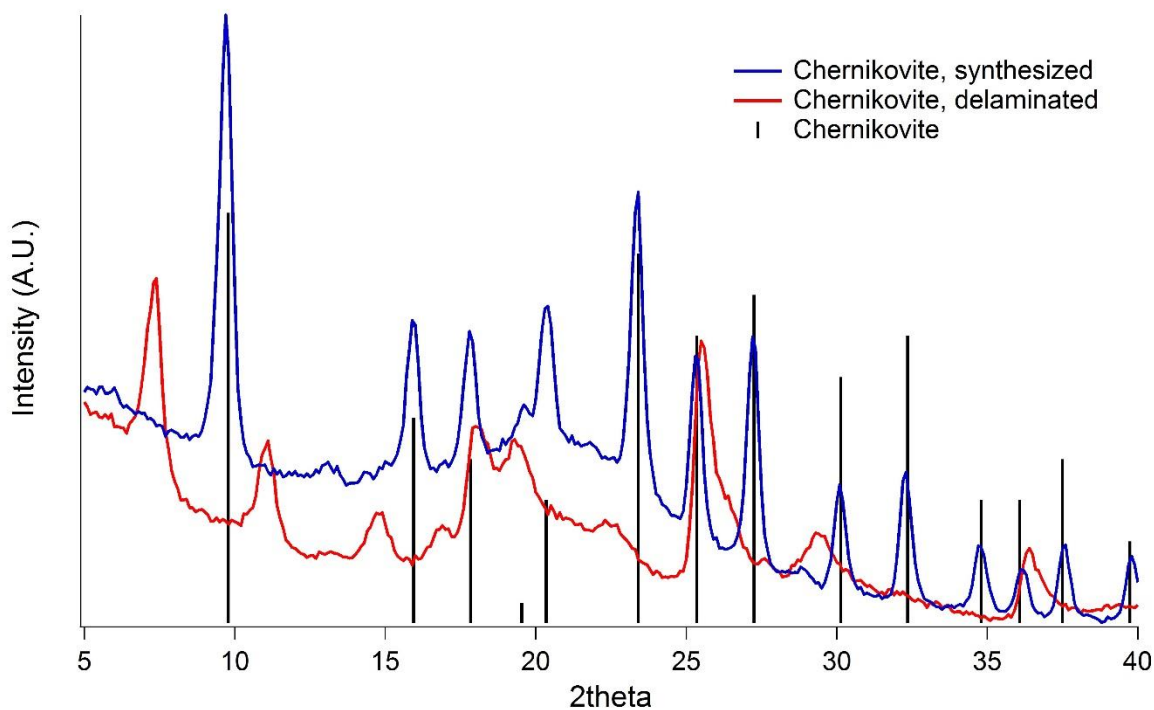


Figure 6.2 Powder X-ray Diffraction data on synthetic chernikovite (blue), chernikovite delaminated with octylamine in DMSO (red), and literature chernikovite¹¹ (black). The first peak seen in the patterns can be attributed to the (001) interlayer distance. Synthetic chernikovite matches with literature peaks with a (001) peak at $2\theta = 9.78^\circ$ ($d = 9.03\text{\AA}$) and post delamination gives a (001) peak at $2\theta = 7.40^\circ$ ($d = 11.93\text{\AA}$).

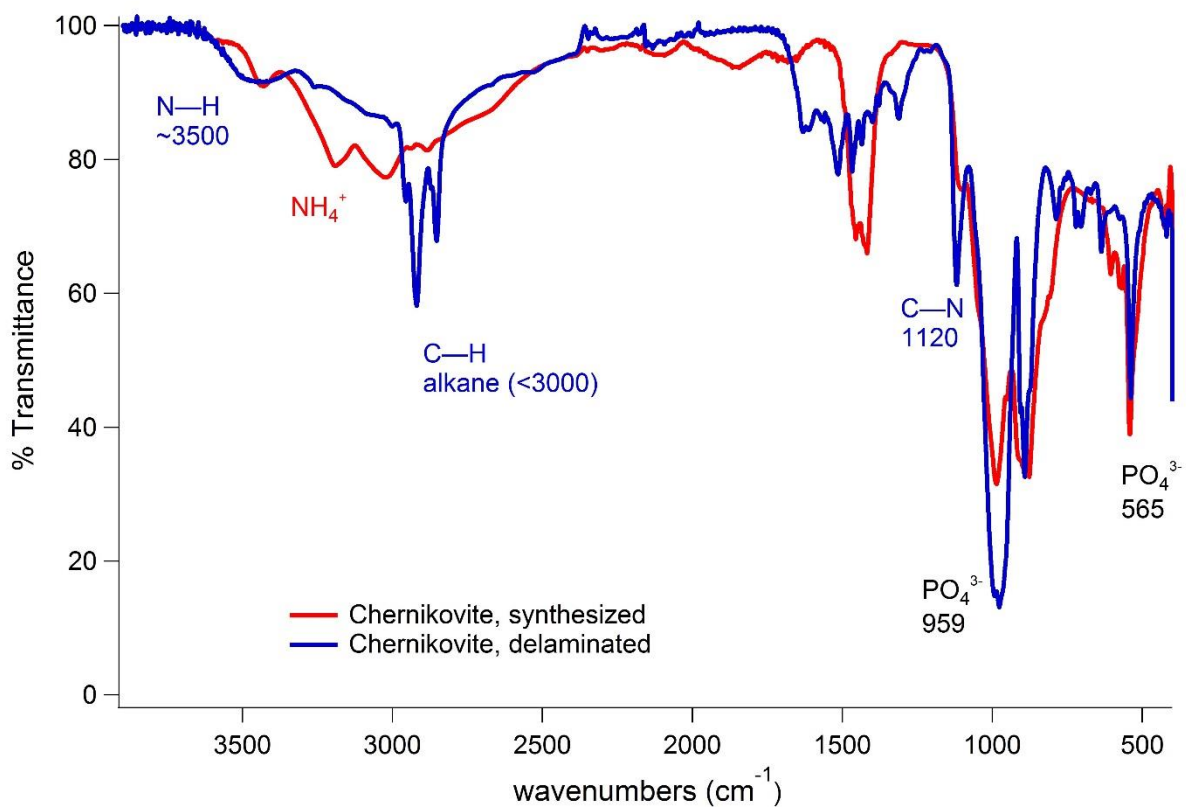


Figure 6.3 Inferred spectra of chernikovite samples, showing the addition of C-H and C-N peaks from the octylamine intercalation in the delaminated sample (blue) which is not seen in the pristine chernikovite sample (red).

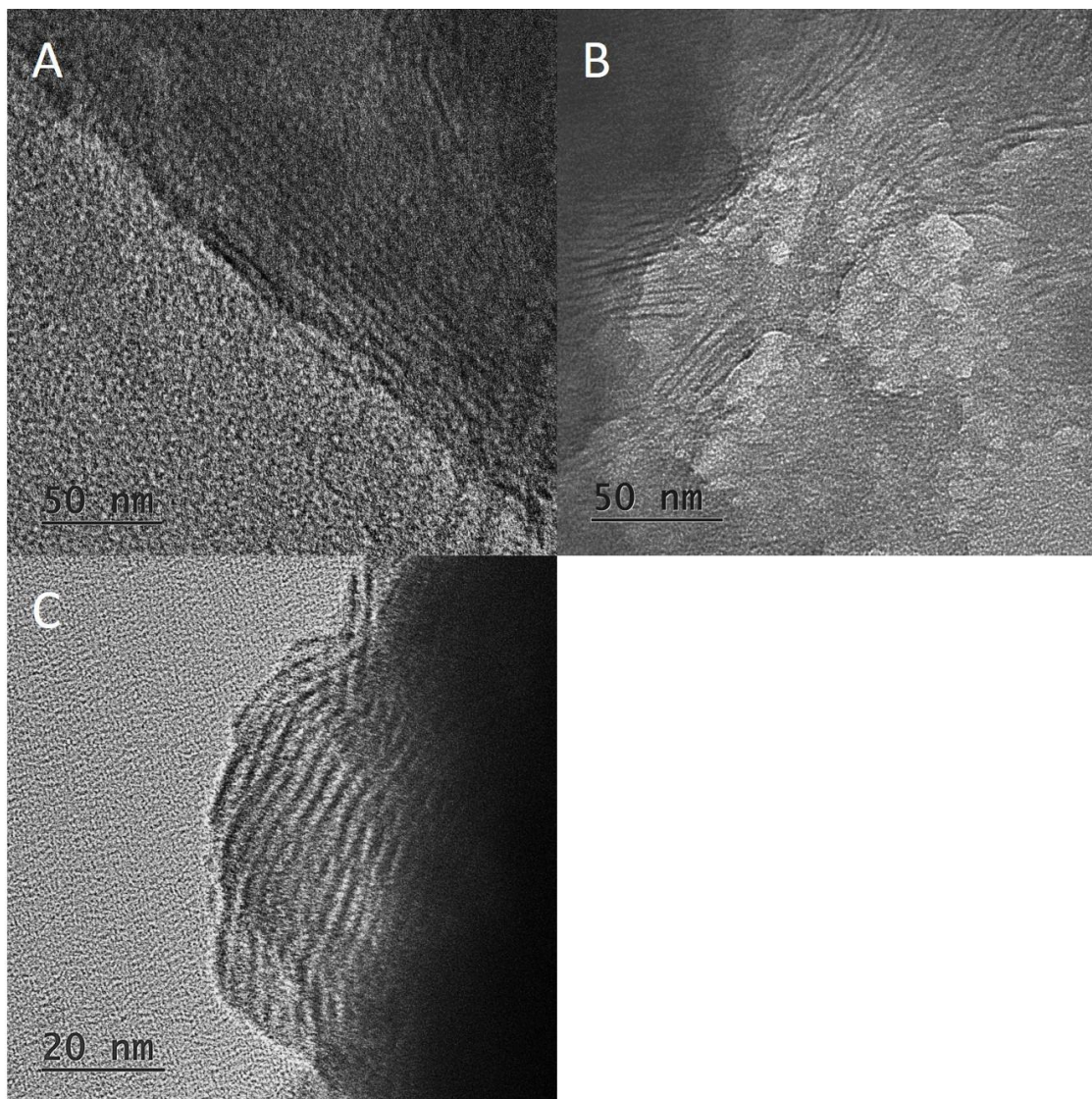


Figure 6.4 TEM images of uranyl phosphate samples. A&C are images of pristine chernikovite samples, showing an average interlayer distance of 2.43nm and 2.58nm respectively. B is an image of a chernikovite sample after octylamine/DMSO exfoliation, showing an average interlayer distance of 4.21nm. Layer-layer distances are larger than values from the powder XRD likely due to uneven sample surface and the presence of DMSO.

Imaging of the uranyl phosphate samples gives a visual representation of the layered structures we are expecting. SEM-EDX imaging (**Figure S3.4**) shows that the powder morphology changes with delamination. Pristine chernikovite the powder shows defined granules throughout the sample but with added amines, the powder loses shape definition with amine intercalation at the magnification shown. Composition analysis confirms the average U to P element ratio is consistent between the starting material and after delamination. Investigation using TEM shows pristine chernikovite has tight groupings of the material layers pointed out in **Figure 6.4**. The ordering of these layers is consistent with what we would expect from an ordered layered material. After intercalation of octylamine the observed atomic layers are positioned randomly throughout the material with expanded layer spacing.

PDF analysis of pristine chernikovite agrees well with simulated PDF.¹¹ PDF analysis of total X-ray scattering gives atom-atom distances of the local structure of a sample. **Figure S3.5** shows a breakdown of peak labels from simulated PDF. Pristine and delaminated samples of chernikovite are compared in **Figure 6.5**, showing similar peaks corresponding to in-plane U-P distances of 3.60Å. In-plane U-U peaks are shifted to lower distances (diagonal U-U peak from 5.25Å to 4.65Å; adjacent U-U peak from 7.00Å to 6.35Å) suggesting the uranyl phosphate sheets are changing from a linear to curved sheet. Curvature of the layers can also be seen in the TEM images (**Figure 6.4**). Signal for the delaminated chernikovite sample is lost at distances above 7.5 Å, limiting further data comparison.

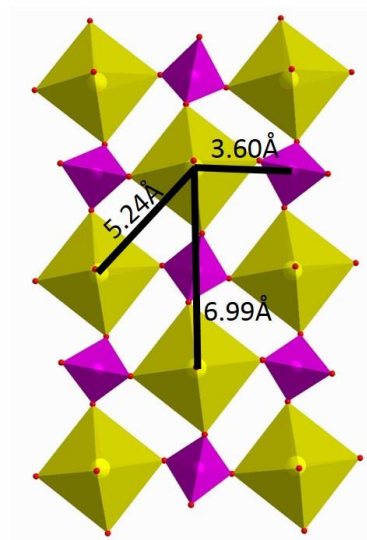
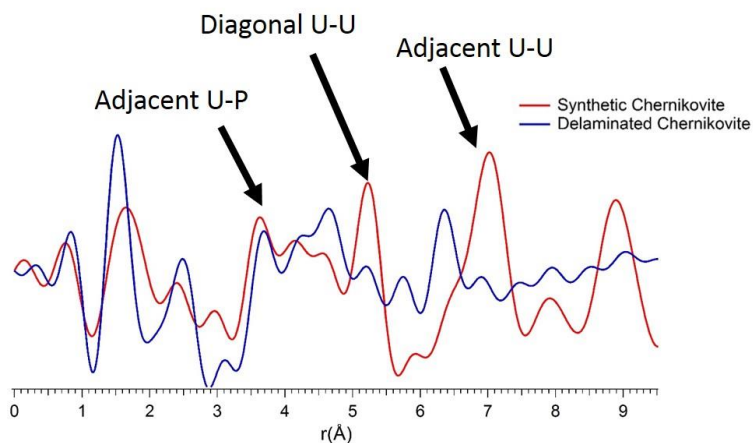


Figure 6.5 PDF analysis (left) of total x-ray scattering data from pristine chernikovite (red) and delaminated chernikovite (blue). Examining the local structure of the two shows that the in-plane U-P peak at 3.60\AA is consistent but there are shifts in the diagonal U-U peak (5.25\AA) and adjacent U-U peak (7.00\AA). The structure of a single chernikovite sheet is shown (right) with labeled atom-atom distances corresponding with the PDF data.

6.5 Conclusion

Synthesis and delamination studies of chernikovite has been demonstrated to provide insight into the structural and chemical properties of layered uranyl minerals. Development of a reproducible synthetic method for chernikovite was shown using ammonium phosphate dibasic as a phosphate source. pH control is key to solubility properties of chernikovite mineral formation for further experimentation. Other derivative structures were reported using similar methodology, with the combination of uranyl, phosphoric acid and corresponding alkali base in derivative composition. Intercalation and delamination using amine intercalates, namely octylamine were successful. Comparison to previously reported mild exfoliation methods for transition metal chalcogenide (TMC) systems¹⁰ like TiS_2 were validated. Understanding the chemistries of uranyl phosphate mineral structures has implications to the nuclear fuel cycle and further experimentation on uranyl surface interactions.

6.6 Acknowledgments

This material is based upon work supported as part of the Materials Sciences of Actinides Center, an Energy Frontier Research Center funded by the U.S. Department of Energy, Office of Science, Office of Basic Energy Sciences under Award Number DE-SC0001089. Homepage: msa-efrc.com

7 Conclusions

Frontier research of hybrid organic/inorganic uranium materials contributes to the chemical understanding of uranium species on the back-end of the nuclear fuel cycle. The relatively new discovery of aqueous uranyl peroxide clusters has motivated this research for developing novel extraction pathways of uranium from spent nuclear fuel. Extraction of uranyl clusters have been developed by taking advantage of the counterions associated to the cluster, undergoing ion exchange with surfactant molecules to affect cluster solubility, and transport of surfactant-cluster hybrids to organic media. Synthesis of most uranyl clusters are long and unpredictable so the reliable U_{24} and U_{32} were key in extraction development. U_{32} rapid self-assembly allowed for cluster synthesis in situ during extraction. Characterization methods such as SAXS and composition analysis reveal that a high concentration of uranium has been transferred to the organic phase as intact clusters. Concentrations remaining in the aqueous phase are on the order of μM , showing distribution ratios above 1×10^4 . Extractions of U_{32} were explored with alternative uranium stocks like simulated spent nuclear fuel (SIMFUEL), precipitating other metal oxide fission products while forming clusters from uranium oxide starting material with similar distribution ratio results.

Clusters in organic solvents retain ions and water molecules within the hollow capsules. CTA-Li- U_{24} characterized by ^7Li NMR techniques shows encapsulated Li ions in two distinct environments. Variable temperature studies show that the Li sites undergo dynamic exchange between encapsulated environments. Though the Li ions are confined to the limited space within the cluster cage, ^7Li peaks are surprisingly narrow suggesting rapid movement. There is no clear reason for the narrow peak widths observed. Collaboration with computational studies show the ^7Li peaks corresponding to coordination to the axial “yl” oxygens under the square face and hexagonal face.

Experimentation with uranium phosphate mineral exfoliation was motivated by the extensive family of uranyl peroxide clusters established from speciation of studtite mineral and the possible applications for uranium surface chemistries experienced in the nuclear fuel cycle. Improved synthetic methods were established for the uranium phosphate mineral, chernikovite,

whereas literature synthesis explanations are incomplete and yield soluble species. Intercalation of organic molecules within the layered chernikovite structure revealed unexpected results. Only uncharged amine molecules successfully intercalate and delaminate the uranyl phosphate layers as opposed to charged surfactant species or alkali ions. Characterization by XRD, IR, and TEM reveal expansion of the interlayer distances and the presence of the octylamine intercalate. PDF analysis was done to show how the intercalate effects the local structure of chernikovite. Delamination of chernikovite directly compares to the delamination of TiS_2 and other layered transition metal chalcogenides. By studying hybrid organic/inorganic systems of uranium, we can gain in site into unique solubility characteristics, ion association, dynamic structure information and solids state structure manipulation. The topics discussed in this thesis work have direct ties into processes of the nuclear fuel cycle, scientific understanding of uranium chemistry, fundamental ion association, and interactions between organic and inorganic materials.

8 Bibliography

Introductory Chapters (1-3):

1. Johnson, E. R. & Best, R. E. Systems Analysis of An Advanced Nuclear Fuel Cycle Based on a Modified UREX + 3c Process. 1–311 (2009).
2. Barker, F. B., Johnson, J. O., Edwards, K. W. & Robinson, B. P. Radiochemical Analysis of Water: Determination of Uranium in Natural Waters. *U.S. Geol. Survey study* 1–33 (1965).
3. Zavodska, L., Kosorinova, E., Scerbakova, L. & Lesny, J. *Environmental chemistry of uranium*.
4. Simpson, M. F. & Law, J. D. Nuclear Fuel Reprocessing. (2010).
5. Wylie, E. M. Crystal Chemistry and Application Development of Uranyl Extended Structure and Nanoscale Materials and Actinyl Ion-substituted Mineral Phases. (University of Notre Dame, 2014).
6. Gelis, a. V. *et al.* Extraction behaviour of actinides and lanthanides in TALSPEAK, TRUEX and NPEX processes of UREX+. *Radiochim. Acta* **97**, 231–232 (2009).
7. Schroeder, N. C., Attrep, M. & Marrero, T. *Los Alamos Technetium and Iodine Separations in the UREX Process*. **836**, (2001).
8. Vandegrift, G. F. Transformation of UREX Effluents to Solid Oxides by Concentration, Denitration, and Calcination. (2000).
9. Rudisill, T. S. *et al.* Demonstration of the UREX Solvent Extraction Process with Dresden Reactor Fuel. 1–4 (2003).
10. Veliscek-Carolan, J. Separation of actinides from spent nuclear fuel: A review. *Journal of Hazardous Materials* **318**, (2016).
11. Mincher, B. J., Peterman, D. R., McDowell, R. G. & Olson, L. G. Radiation Chemistry of Advanced TALSPEAK Flowsheet. (2013).

12. Starks, J. B. The PUREX Process. 1–41 (1977).
13. Kaltsoyannis, N. Computational Study of Analogues of the Uranyl Ion Containing the $-N=U=N-$ Unit. *Inorg. Chem.* **39**, 6009–6017 (2000).
14. Yatsimirskii, K. B. Relativistic effects in chemistry. *Theor. Exp. Chem.* **31**, 153–168 (1995).
15. Lefort, M. & Tarrago, X. Radiolysis of water by particles of high linear energy transfer. The primary chemical yields in aqueous acid solutions of ferrous sulfate, and in mixtures of thallos and ceric ions. *J. Phys. Chem.* **63**, 833–836 (1959).
16. Vaes, F. & Gand, D. Six nouveaux minéraux d'urane provenant de Shinkolobwe (Katanga). 212–225 (1944).
17. Lindqvist, I. No Title. *Ark. Kemi* **5**, (1953).
18. Keggin, J. F. The Structure and Formula of 12-Phosphotungstic Acid. *Proc. R. Soc. A Math. Phys. Eng. Sci.* **144**, 75–100 (1934).
19. Hill, C. L. Progress and challenges in polyoxometalate-based catalysis and catalytic materials chemistry. *J. Mol. Catal. A Chem.* **262**, 2–6 (2007).
20. Bijelic, A. & Rompel, A. The use of polyoxometalates in protein crystallography – An attempt to widen a well-known bottleneck. *Coord. Chem. Rev.* **299**, 22–38 (2015).
21. Sharpless, K. B. & Flood, T. C. Oxotransition metal oxidants as mimics for the action of mixed-function oxygenases. 'NIH shift' with chromyl reagents. *J. Am. Chem. Soc.* **93**, 2316–2318 (1971).
22. Kubatko, K. A., Helean, K. B., Navrotsky, A. & Burns, P. C. Stability of Peroxide-Containing Uranyl Minerals. *Science (80-.)*. **302**, 1191–1193 (2003).
23. Goberna-Ferrón, S., Park, D.-H., Amador, J. M., Keszler, D. A. & Nyman, M. Amphoteric Aqueous Hafnium Cluster Chemistry. *Angew. Chemie* **128**, 6329–6332 (2016).
24. Sadeghi, O., Zakharov, L. N. & Nyman, M. Crystal growth. Aqueous formation and manipulation of the iron-oxo Keggin ion. *Science* **347**, 1359–62 (2015).

25. Wang, W., Wentz, K. M., Hayes, S. E., Johnson, D. W. & Keszler, D. A. Synthesis of the Hydroxide Cluster $[Al_{13}(\mu_3-OH)_6(\mu-OH)_{18}(H_2O)_{24}]^{15+}$ from an Aqueous Solution. *Inorg. Chem.* **50**, 4683–4685 (2011).
26. Burns, P. C. *et al.* Actinyl peroxide nanospheres. *Angew. Chem. Int. Ed. Engl.* **44**, 2135–9 (2005).
27. Qiu, J. & Burns, P. C. Clusters of actinides with oxide, peroxide, or hydroxide bridges. *Chem. Rev.* **113**, 1097–120 (2013).
28. Sigmon, G. E., Weaver, B., Kubatko, K.-A. & Burns, P. C. Crown and bowl-shaped clusters of uranyl polyhedra. *Inorg. Chem.* **48**, 10907–9 (2009).
29. Liao, Z., Deb, T. & Nyman, M. Elucidating Self-Assembly Mechanisms of Uranyl–Peroxide Capsules from Monomers. *Inorg. Chem.* **53**, 10506–10513 (2014).
30. Ling, J., Wallace, C. M., Szymanowski, J. E. S. & Burns, P. C. Hybrid uranium-oxalate fullerene topology cage clusters. *Angew. Chem. Int. Ed. Engl.* **49**, 7271–3 (2010).
31. Unruh, D. K. *et al.* Complex nanoscale cage clusters built from uranyl polyhedra and phosphate tetrahedra. *Inorg. Chem.* **50**, 5509–16 (2011).
32. Miro, P. *et al.* Uranyl-peroxide Nanocapsules in Aqueous Solution : Force Field Development and First Applications Uranyl-peroxide Nanocapsules in Aqueous Solution : Force Field Development and First Applications. (2014).
33. Miró, P., Pierrefixe, S., Gicquel, M., Gil, A. & Bo, C. On the origin of the cation templated self-assembly of uranyl-peroxide nanoclusters. *J. Am. Chem. Soc.* **132**, 17787–94 (2010).
34. Falaise, C. & Nyman, M. The Key Role of U₂₈ in the Aqueous Self-Assembly of Uranyl Peroxide Nanocages. *Chem. - A Eur. J.* 14678–14687 (2016).
doi:10.1002/chem.201602130
35. Schnablegger, H. & Singh, Y. *The SAXS Guide*. (2011).
36. Kikhney, A. SAXS man - Data reduction and processing.
37. Manual, I. SAXSquant 3.x.

38. Ilavsky, J., Jemian, P. R., Ilavsky, J. & Jemian, P. R. Irena : tool suite for modeling and analysis of small-angle scattering Irena : tool suite for modeling and analysis of small-angle scattering. *J. Appl. Crystallogr.* **42**, 347–353 (2009).
39. Skoog, D. A., Holler, F. J. & Crouch, S. R. *Principles of Instrumental Analysis 6th.* (2006).
40. Silverstein, R. M., Webster, F. X. & Kiemle, D. J. *Spectrometric Identification of Organic Compounds 7th.* (2005).
41. Thomas Andrews, J., Sen, P. & Sen, P. K. Optical free induction decay. *Indian J. Pure Appl. Phys.* **36**, 655–660 (1998).
42. Andrew, E. R., Bradbury, A. & Eades, R. G. Nuclear Magnetic Resonance Spectra from a Crystal rotated at High Speed. *Nature* **182**, 1659–1659 (1958).
43. Hennel, J. W. & Klinowski, J. in 1–14 (2005). doi:10.1007/b98646
44. Yannoni, C. S. High-resolution NMR in solids: the CPMAS experiment. *Acc. Chem. Res.* **15**, 201–208 (1982).
45. Reich, H. J. WinDNMR: Dynamic NMR Spectra for Windows. *J. Chem. Educ.* **72**, 1086 (1995).
46. Nyman, M. & Alam, T. M. Dynamics of uranyl peroxide nanocapsules. *J. Am. Chem. Soc.* **134**, 20131–8 (2012).

Chapter 4:

1. International Energy Agency. *Key World Energy Statistics 2016.* (2016). doi:10.1787/9789264039537-en
2. Starks, J. B. *The PUREX Process.* (1977).
3. Beltrami, D. *et al.* Recovery of Uranium from Wet Phosphoric Acid by Solvent Extraction Processes. *Chem. Rev.* (2014). doi:10.1021/cr5001546
4. Burns, P. C. *et al.* Actinyl peroxide nanospheres. *Angew. Chem. Int. Ed. Engl.* **44**, 2135–9 (2005).

5. Qiu, J. & Burns, P. C. Clusters of actinides with oxide, peroxide, or hydroxide bridges. *Chem. Rev.* **113**, 1097–120 (2013).
6. Knope, K. E. & Soderholm, L. Solution and solid-state structural chemistry of actinide hydrates and their hydrolysis and condensation products. *Chem. Rev.* **113**, 944–94 (2013).
7. Liao, Z., Deb, T. & Nyman, M. Elucidating Self-Assembly Mechanisms of Uranyl Peroxide Capsules from Monomers. *Inorg. Chem.* **53**, 10506–10513 (2014).
8. Zanonato, P. L., Di Bernardo, P., Fischer, A. & Grenthe, I. Chemical equilibria in the UO_2^{2+} - H_2O_2 - F^-/OH^- systems and $\text{UO}_2(\text{O}_2)\text{F}$ and $\text{UO}_2(\text{O}_2)\text{OH}^-$ as possible solution precursors for the formation of $[\text{Na}_6(\text{OH}_2)_8]@[\text{UO}_2(\text{O}_2)\text{F}]_{24}^{18-}$ and $[\text{Na}_6(\text{OH}_2)_8]@[\text{UO}_2(\text{O}_2)\text{OH}]_{24}^{18-}$ clusters. *Dalt. Trans.* **In Press**, 10129–10137 (2013).
9. Falaise, C. & Nyman, M. The Key Role of U_{28} in Aqueous Self-Assembly of Uranyl Peroxide Nanocages. *Chem. - A Eur. J.* Accepted (2016).
10. Zanonato, P. L., Szabó, Z., Vallet, V., Di Bernardo, P. & Grenthe, I. Alkali-metal ion coordination in uranyl(vi) poly-peroxo complexes in solution, inorganic analogues to crown-ethers. Part 2. Complex formation in the tetramethyl ammonium-, Li^+ -, Na^+ - and K^+ -uranyl(vi)-peroxide-carbonate systems. *Dalton Trans.* **44**, 16565–72 (2015).
11. Caë, S. Le. Water Radiolysis: Influence of Oxide Surfaces on H_2 Production under Ionizing Radiation. *Water* **3**, 235–253 (2011).
12. Grenthe, I. *et al.* Chemical Thermodynamics of Uranium. 1992 1–735 (1992).
13. Miró, P., Pierrefixe, S., Gicquel, M., Gil, A. & Bo, C. On the origin of the cation templated self-assembly of uranyl-peroxide nanoclusters. *J. Am. Chem. Soc.* **132**, 17787–94 (2010).
14. Nyman, M. & Alam, T. M. Dynamics of uranyl peroxide nanocapsules. *J. Am. Chem. Soc.* **134**, 20131–8 (2012).
15. Li, D., Simotwo, S., Nyman, M. & Liu, T. Evolution of actinyl peroxide clusters U_{28} in dilute electrolyte solution: Exploring the transition from simple ions to macroionic assemblies. *Chem. - A Eur. J.* **20**, 1683–1690 (2014).
16. Li, H., Sun, H., Qi, W., Xu, M. & Wu, L. Onionlike hybrid assemblies based on surfactant-encapsulated polyoxometalates. *Angew. Chem. Int. Ed. Engl.* **46**, 1300–3 (2007).
17. Volkmer, D. *et al.* Toward Nanodevices : Synthesis and Characterization of the

Nanoporous Surfactant-Encapsulated Keplerate

- (DODA)₄₀(NH₄)₂[(H₂O)_nMo₁₃₂O₃₇₂(CH₃COO)₃₀(H₂O)₇₂]. *J. Am. Chem. Soc.* **40**, 1995–1998 (2000).
18. Hill, C. L. & Brown, R. B. Sustained epoxidation of olefins by oxygen donors catalyzed by transition metal-substituted polyoxometalates, oxidatively resistant inorganic analogs of metalloporphyrins. *J. Am. Chem. Soc.* **108**, 536–538 (1986).
 19. Katsoulis, D. E., Tausch, V. S. & Pope, M. T. Interaction of sulfur dioxide with heteropolyanions in nonpolar solvents. Evidence for complex formation. *Inorg. Chem.* **26**, 215–216 (1987).
 20. Lyon, D. K. *et al.* Highly Oxidation Resistant Inorganic-Porphyrin Analogue Polyoxometalate Oxidation Catalysts . 1 . The Synthesis and Characterization of Aqueous-Soluble Potassium Salts of a₂-P₂W₁₇O₆₁(Mn⁺.OH₂)(n-10) and Organic Solvent Soluble Tetra-n-butylammonium Salts o. *Am. Chem. Soc.* **113**, 7209–7221 (1991).
 21. Jiang, Y. *et al.* Anisotropic ionic liquids built from nonmesogenic cation surfactants and Keggin-type polyoxoanions. *Chem. Commun. (Camb)*. **47**, 10287–9 (2011).
 22. Zhang, J., Song, Y. F., Cronin, L. & Liu, T. Self-assembly of organic-inorganic hybrid amphiphilic surfactants with large polyoxometalates as polar head groups. *J. Am. Chem. Soc.* **130**, 14408–14409 (2008).
 23. Liu, S. & Tang, Z. Polyoxometalate-based functional nanostructured films: Current progress and future prospects. *Nano Today* **5**, 267–281 (2010).
 24. Breitwieser, R. *et al.* Binary Superlattices from {Mo₁₃₂} Polyoxometalates and Maghemite Nanocrystals: Long-Range Ordering and Fine-Tuning of Dipole Interactions. *Small* **12**, 220–228 (2016).
 25. Li, H. *et al.* A highly transparent and luminescent hybrid based on the copolymerization of surfactant-encapsulated polyoxometalate and methyl methacrylate. *Adv. Mater.* **17**, 2688–2692 (2005).
 26. Blazevic, A. & Rompel, A. The Anderson-Evans polyoxometalate: From inorganic building blocks via hybrid organic-inorganic structures to tomorrows ‘Bio-POM’. *Coord. Chem. Rev.* **307**, 42–64 (2016).
 27. Gaunt, A. J., May, I., Helliwell, M. & Richardson, S. The first structural and

- spectroscopic characterization of a neptunyl polyoxometalate complex. *J. Am. Chem. Soc.* **124**, 13350–13351 (2002).
28. Bu, W. *et al.* X-ray studies of interfacial strontium-extractant complexes in a model solvent extraction system. *J. Phys. Chem. B* **118**, 12486–12500 (2014).
 29. Bu, W. *et al.* Observation of a rare earth ion-extractant complex arrested at the oil-water interface during solvent extraction. *J. Phys. Chem. B* **118**, 10662–10674 (2014).
 30. Gannaz, B., Antonio, M. ., Chiarizia, R., Hill, C. & Cote, G. Structural study of trivalent lanthanide and actinide complexes formed upon solvent extraction. *Dalt. Transactions* 4553–62 (2006). doi:10.1039/b609492a
 31. Sigmon, G. E. & Burns, P. C. Rapid self-assembly of uranyl polyhedra into crown clusters. *J. Am. Chem. Soc.* **133**, 9137–9 (2011).
 32. Nyman, M., Rodriguez, M. a & Alam, T. M. The U28 Nanosphere: What's Inside? *Eur. J. Inorg. Chem.* 2197–2205 (2011).
 33. Zhang, R., Thiagarajan, P. & Tiede, D. M. Probing protein fine structures by wide angle solution X-ray scattering. *J. Appl. Crystallogr.* **33**, 565–568 (2000).
 34. Pedersen, J. S. *Neutrons, X-rays Light Scatt. Methods Appl. to Soft Condens. Matter.* (2002).
 35. Ilavsky, J. & Jemian, P. R. Irena : tool suite for modeling and analysis of small-angle scattering. *J. Appl. Crystallogr.* **42**, 347–353 (2009).
 36. Pileni, M. P. Reverse micelles as microreactors. *J. Phys. Chem.* **97**, 6961–6973 (1993).
 37. Paleologos, E. K., Giokas, D. L. & Karayannis, M. I. Micelle-mediated separation and cloud-point extraction. *TrAC - Trends Anal. Chem.* **24**, 426–436 (2005).
 38. Alam, T. M., Liao, Z., Zakharov, L. N. & Nyman, M. Solid-state dynamics of uranyl polyoxometalates. *Chemistry* **20**, 8302–7 (2014).
 39. Crans, D. C., Rithner, C. D., Baruah, B., Gourley, B. L. & Levinger, N. E. Molecular Probe Location in Reverse Micelles Determined by NMR Dipolar Interactions. *J. Am. Chem. Soc.* 4437–4445 (2006).
 40. Volkmer, D. *et al.* Toward Nanodevices : Synthesis and Characterization of the Nanoporous Surfactant-Encapsulated Keplerate $(\text{DODA})_{40}(\text{NH}_4)_2[(\text{H}_2\text{O})_n\text{Mo}_{132}\text{O}_{372}(\text{CH}_3\text{COO})_{30}(\text{H}_2\text{O})_{72}]$. *J. Am. Chem. Soc.* **40**, 1995–1998 (2000).41.

41. Wylie, E. M. *Crystal Chemistry and Application Development of Uranyl Extended Structure and Nanoscale Materials and Actinyl Ion-substituted Mineral Phases*. (University of Notre Dame, 2014).
42. Wylie, E. M. *et al.* Processing used nuclear fuel with nanoscale control of uranium and ultrafiltration. *J. Nucl. Mater.* **473**, 125–130 (2016).
43. Renier, O., Falaise, C., Neal, H., Kozma, K. & Nyman, M. Closing uranyl polyoxometalate capsules with bismuth and lead polyoxocations. *Angew. Chem. Int. Ed. Engl.* **55**, 13480–13484 (2016).
44. Blanchard, F. *et al.* Role of Ammonium Ions in the Formation of Ammonium Uranyl Peroxides and Uranyl Peroxo-oxalates. *Cryst. Growth Des.* **16**, 200–209 (2016).
45. Diwu, J. & Albrecht-Schmitt, T. E. Mixed-valent uranium(IV,VI) diphosphate: Synthesis, structure, and spectroscopy. *Inorg. Chem.* **51**, 4432–4434 (2012).
46. Read, C. M., Smith, M. D. & zur Loye, H.-C. Single Crystal Growth and Structural Characterization of a Novel Mixed-Valent Ternary Uranium Oxide, $K_8U_7O_{24}$. *J. Chem. Crystallogr.* **44**, 604–608 (2014).
47. Duval, S., Sobanska, S., Roussel, P. & Loiseau, T. $B-\alpha-[AsW_9O_{33}]^{9-}$ polyoxometalates incorporating hexanuclear uranium $\{U_6O_8\}$ -like clusters bearing the U(IV) form or unprecedented mixed valence U(IV)/U(VI) involving direct U(VI)[double bond, length as m-dash]O-U(IV) bonding. *Dalton Trans.* **44**, 19772–6 (2015).
48. Ling, J., Wallace, C. M., Szymanowski, J. E. S. & Burns, P. C. Hybrid uranium-oxalate fullerene topology cage clusters. *Angew. Chem. Int. Ed. Engl.* **49**, 7271–3 (2010).

Chapter 5:

1. Nyman, M.; Burns, P. C. A Comprehensive Comparison of Transition-Metal and Actinyl Polyoxometalates. *Chem. Soc. Rev.* 2012, 41, 7354–7367.
2. Burns, P. C.; Kubatko, K. A.; Sigmon, G.; Fryer, B. J.; Gagnon, J. E.; Antonio, M. R.; Soderholm, L. Actinyl Peroxide Nanospheres. *Angew. Chem., Int. Ed.* 2005, 44, 2135–2139.
3. Wylie, E. M.; Peruski, K. M.; Weidman, J. L.; Phillip, W. A.; Burns, P. C. Ultrafiltration of Uranyl Peroxide Nanoclusters for the Separation of Uranium from Aqueous Solution.

- ACS Appl. Mater. Interfaces 2014, 6, 473–479.
- Blanchard, F.; Ellart, M.; Rivenet, M.; Vigier, N.; Hablot, I.; Morel, B.; Grandjean, S.; Abraham, F. Neodymium Uranyl Peroxide Synthesis by Ion Exchange on Ammonium Uranyl Peroxide Nanoclusters. *Chem. Commun.* 2016, 52, 3947–3950.
 - Wylie, E. M.; Peruski, K. M.; Prizio, S. E.; Bridges, A. N.; Rudisill, T. S.; Hobbs, D. T.; Phillip, W. A.; Burns, P. C. Processing Used Nuclear Fuel with Nanoscale Control of Uranium and Ultrafiltration. *J. Nucl. Mater.* 2016, 473, 125–130.
 - Odoh, S. O.; Shamblin, J.; Colla, C. A.; Hickam, S.; Lobeck, H. L.; Lopez, R. A.; Olds, T.; Szymanowski, J. E.; Sigmon, G. E.; Neufeind, J.; et al. Structure and Reactivity of X-ray Amorphous Uranyl Peroxide, U₂O₇. *Inorg. Chem.* 2016, 55, 3541–3546.
 - Qiu, J.; Burns, P. C. Clusters of Actinides with Oxide, Peroxide, or Hydroxide Bridges. *Chem. Rev.* 2013, 113, 1097–1120.
 - Qiu, J.; Ling, J.; Jouffret, L.; Thomas, R.; Szymanowski, J. E.; Burns, P. C. Water-Soluble Multi-Cage Super Tetrahedral Uranyl Peroxide Phosphate Clusters. *Chem. Sci.* 2014, 5, 303–310.
 - Liao, Z.; Deb, T.; Nyman, M. Elucidating Self-Assembly Mechanisms of Uranyl–Peroxide Capsules from Monomers. *Inorg. Chem.* 2014, 53, 10506–10513.
 - Miró, P.; Vlaisavljevich, B.; Gil, A.; Burns, P. C.; Nyman, M.; Bo, C. Self-Assembly of Uranyl–Peroxide Nanocapsules in Basic Peroxidic Environments. *Chem. - Eur. J.* 2016, 22, 8571–8578.
 - Gao, Y.; Eghtesadi, S. A.; Liu, T. Supramolecular Structures Formation of Polyoxometalates in Solution Driven by Counterion–Macroion Interaction. *Adv. Inorg. Chem.* 2017, 69, 29–65.
 - Li, D.; Simotwo, S.; Nyman, M.; Liu, T. Evolution of Actinyl Peroxide Clusters U₂₈ in Dilute Electrolyte Solution: Exploring the Transition from Simple Ions to Macroionic Assemblies. *Chem. - Eur. J.* 2014, 20, 1683–1690.
 - Miró, P.; Pierrefixe, S.; Gicquel, M. I.; Gil, A.; Bo, C. On the Origin of the Cation

- Templated Self-Assembly of Uranyl-Peroxide Nanoclusters. *J. Am. Chem. Soc.* 2010, 132, 17787–17794.
14. Qiu, J.; Vlaisavljevich, B.; Jouffret, L.; Nguyen, K.; Szymanowski, J. E. S.; Gagliardi, L.; Burns, P. C. Cation Templating and Electronic Structure Effects in Uranyl Cage Clusters Probed by the Isolation of Peroxide-Bridged Uranyl Dimers. *Inorg. Chem.* 2015, 54, 4445–4455.
 15. Nyman, M.; Alam, T. M. Dynamics of Uranyl Peroxide Nanocapsules. *J. Am. Chem. Soc.* 2012, 134, 20131–20138.
 16. Miró, P.; Vlaisavljevich, B.; Dzubak, A. L.; Hu, S.; Burns, P. C.; Cramer, C. J.; Spezia, R.; Gagliardi, L. Uranyl–peroxide nanocapsules in aqueous solution: force field development and first applications. *J. Phys. Chem. C* 2014, 118, 24730–24740.
 17. Neal, H. A.; Szymanowski, J.; Fein, J. B.; Burns, P. C.; Nyman, M. Benchmarking Uranyl Peroxide Capsule Chemistry in Organic Media. *Eur. J. Inorg. Chem.* 2017, 2017, 39–46.
 18. Gao, Y.; Szymanowski, J. E.; Sun, X.; Burns, P. C.; Liu, T. Thermal responsive ion Selectivity of uranyl peroxide nanocages: an inorganic mimic of K⁺ ion channels. *Angew. Chem.* 2016, 128, 7001– 7005.
 19. Alam, T. M.; Liao, Z.; Zakharov, L. N.; Nyman, M. Solid-State Dynamics of Uranyl Polyoxometalates. *Chem. - Eur. J.* 2014, 20, 8302– 8307.
 20. Olds, T. A.; Dembowski, M.; Wang, X.; Hoffman, C.; Alam, T. M.; Hickam, S.; Pellegrini, K. L.; He, J.; Burns, P. C. Single-Crystal Time-of-Flight Neutron Diffraction and Magic-Angle-Spinning NMR Spectroscopy Resolve the Structure and ¹H and ⁷Li Dynamics of the Uranyl Peroxide Nanocluster U60. *Inorg. Chem.* 2017, 56, 9676–9683.
 21. Sigmon, G. E.; Ling, J.; Unruh, D. K.; Moore-Shay, L.; Ward, M.; Weaver, B.; Burns, P. C. Uranyl–Peroxide Interactions Favor Nanocluster Self-Assembly. *J. Am. Chem. Soc.* 2009, 131, 16648–16649.
 22. Sigmon, G. E.; Unruh, D. K.; Ling, J.; Weaver, B.; Ward, M.; Pressprich, L.; Simonetti, A.; Burns, P. C. Symmetry versus Minimal Pentagonal Adjacencies in Uranium-Based Polyoxometalate Fullerene Topologies. *Angew. Chem., Int. Ed.* 2009, 48, 2737–2740.

23. Nyman, M.; Rodriguez, M. A.; Alam, T. M. The U28 Nanosphere: What's Inside? *Eur. J. Inorg. Chem.* 2011, 2011, 2197–2205.
24. Gil, A.; Karhánek, D.; Miró, P.; Antonio, M. R.; Nyman, M.; Bo, C. A Journey Inside the U28 Nanocapsule. *Chem. - Eur. J.* 2012, 18, 8340–8346.
25. Sigmon, G. E.; Weaver, B.; Kubatko, K.-A.; Burns, P. C. Crown and Bowl-Shaped Clusters of Uranyl Polyhedra. *Inorg. Chem.* 2009, 48, 10907–10909.
26. Ilavsky, J.; Jemian, P. R. Irena: Tool Suite for Modeling and Analysis of Small-Angle Scattering. *J. Appl. Crystallogr.* 2009, 42, 347–353.
27. O'Boyle, N. M.; Banck, M.; James, C. A.; Morley, C.; Vandermeersch, T.; Hutchison, G. R. Open Babel: An Open Chemical Toolbox. *J. Cheminform.* 2011, 3, 33.
28. Reich, H. J. WinDNMR: Dynamic NMR Spectra for Windows. *J. Chem. Educ.* 1995, 72, 1086.
29. Becke, A. D. Density Functional Thermochemistry. III. The Role of Exact Exchange. *J. Chem. Phys.* 1993, 98, 5648–5652.
30. Lee, C.; Yang, W.; Parr, R. G. Development of the Colle-Salvetti Correlation-Energy Formula into a Functional of the Electron Density. *Phys. Rev. B: Condens. Matter Mater. Phys.* 1988, 37, 785.
31. Petersson, A.; Bennett, A.; Tensfeldt, T. G.; Al-Laham, M. A.; Shirley, W. A.; Mantzaris, J. A Complete Basis Set Model Chemistry. I. The Total Energies of Closed-Shell Atoms and Hydrides of the First-Row Elements. *J. Chem. Phys.* 1988, 89, 2193–2218.
32. Petersson, G. A.; Al-Laham, M. A. A Complete Basis Set Model Chemistry. II. Open-Shell Systems and the Total Energies of the First-Row Atoms. *J. Chem. Phys.* 1991, 94, 6
33. Küchle, W.; Dolg, M.; Stoll, H.; Preuss, H. Energy-Adjusted Pseudopotentials for the Actinides. Parameter Sets and Test Calculations for Thorium and Thorium Monoxide. *J. Chem. Phys.* 1994, 100, 7535–7542.
34. Cao, X.; Dolg, M. Segmented Contraction Scheme for Small-Core Actinide Pseudopotential Basis Sets. *J. Mol. Struct.: THEOCHEM* 2004, 673, 203–209.

35. Marenich, A. V.; Cramer, C. J.; Truhlar, D. G. Universal Solvation Model Based on Solute Electron Density and on a Continuum Model of the Solvent Defined by the Bulk Dielectric Constant and Atomic Surface Tensions. *J. Phys. Chem. B* 2009, 113, 6378–6396.
36. Perdew, J. P.; Burke, K.; Ernzerhof, M. Generalized Gradient Approximation Made Simple. *Phys. Rev. Lett.* 1996, 77, 3865.
37. ADF2014; SCM, Theoretical Chemistry; Vrije Universiteit: Amsterdam, The Netherlands, <https://www.scm.com/>.
38. van Lenthe, E. v.; Snijders, J.; Baerends, E. The Zero-Order Regular Approximation for Relativistic Effects: The Effect of Spin–Orbit Coupling in Closed Shell Molecules. *J. Chem. Phys.* 1996, 105, 6505–6516.
39. Van Lenthe, E.; Baerends, E. J. Optimized Slater-Type Basis Sets for the Elements 1 – 118. *J. Comput. Chem.* 2003, 24, 1142–1156.
40. Klamt, A. Conductor-Like Screening Model for Real Solvents: A New Approach to the Quantitative Calculation of Solvation Phenomena. *J. Phys. Chem.* 1995, 99, 2224–2235.
41. Klamt, A.; Schüürmann, G. COSMO: A New Approach to Dielectric Screening in Solvents with Explicit Expressions for the Screening Energy and Its Gradient. *J. Chem. Soc., Perkin Trans. 2* 1993, 5, 799–805.
42. Allinger, N. L.; Zhou, X.; Bergsma, J. Molecular Mechanics Parameters. *J. Mol. Struct.: THEOCHEM* 1994, 312, 69–83.
43. Kelly, C. P.; Cramer, C. J.; Truhlar, D. G. Aqueous Solvation Free Energies of Ions and Ion– Water Clusters Based on an Accurate Value for the Absolute Aqueous Solvation Free Energy of the Proton. *J. Phys. Chem. B* 2006, 110, 16066–16081.
44. Frisch, M.; Trucks, G.; Schlegel, H. B.; Scuseria, G.; Robb, M.; Cheeseman, J.; Scalmani, G.; Barone, V.; Mennucci, B.; Petersson, G. Gaussian 09, revision D.01; Gaussian, Inc.: Wallingford, CT, 2009.
45. Cheeseman, J. R.; Trucks, G. W.; Keith, T. A.; Frisch, M. J. A Comparison of Models for

- Calculating Nuclear Magnetic Resonance Shielding Tensors. *J. Chem. Phys.* 1996, 104, 5497–5509.
46. Alam, T. M.; Hart, D.; Rempe, S. L. Computing the ^7Li NMR Chemical Shielding of Hydrated Li^+ Using Cluster Calculations and Time-Averaged Configurations from Ab Initio Molecular Dynamics Simulations. *Phys. Chem. Chem. Phys.* 2011, 13, 13629–13637.
 47. Watfa, N.; Melgar, D.; Haouas, M.; Taulelle, F.; Hijazi, A.; Naoufal, D.; Avalos, J. B.; Floquet, S. b.; Bo, C.; Cadot, E. Hydrophobic Effect as a Driving Force for Host–Guest Chemistry of a Multi-Receptor Keplerate-Type Capsule. *J. Am. Chem. Soc.* 2015, 137, 5845–5851.
 48. Volkmer, D.; Du Chesne, A.; Kurth, D. G.; Schnablegger, H.; Lehmann, P.; Koop, M. J.; Müller, A. Toward Nanodevices: Synthesis and Characterization of the Nanoporous Surfactant-Encapsulated Keplerate $(\text{DODA})_{40}(\text{NH}_4)_2[(\text{H}_2\text{O})_n\text{C}_{60}\text{Mo}_{132}\text{O}_{372}(\text{CH}_3\text{COO})_{30}(\text{H}_2\text{O})_{72}]$. *J. Am. Chem. Soc.* 2000, 122, 1995–1998.
 49. Both the Nyman and Burns laboratories have many unpublished structures of U24 that show Li coordinated in this manner.
 50. Mähler, J.; Persson, I. A Study of the Hydration of the Alkali Metal Ions in Aqueous Solution. *Inorg. Chem.* 2012, 51, 425–438.081–6090.1. Johnson, E. R. & Best, R. E. Systems Analysis of An Advanced Nuclear Fuel Cycle Based on a Modified UREX + 3c Process. 1–311 (2009).
 2. Barker, F. B., Johnson, J. O., Edwards, K. W. & Robinson, B. P. Radiochemical Analysis of Water: Determination of Uranium in Natural Waters. *U.S. Geol. Survay study* 1–33 (1965).
 3. Zavodska, L., Kosorinova, E., Scerbakova, L. & Lesny, J. *Environmental chemistry of uranium*.
 4. Simpson, M. F. & Law, J. D. *Nuclear Fuel Reprocessing*. (2010).
 5. Wylie, E. M. *Crystal Chemistry and Application Development of Uranyl Extended*

- Structure and Nanoscale Materials and Actinyl Ion-substituted Mineral Phases.
(University of Notre Dame, 2014).
6. Gelis, a. V. *et al.* Extraction behaviour of actinides and lanthanides in TALSPEAK, TRUEX and NPEX processes of UREX+. *Radiochim. Acta* **97**, 231–232 (2009).
 7. Schroeder, N. C., Attrep, M. & Marrero, T. *Los Alamos Technetium and Iodine Separations in the UREX Process*. **836**, (2001).
 8. Vandegrift, G. F. Transformation of UREX Effluents to Solid Oxides by Concentration, Denitration, and Calcination. (2000).
 9. Rudisill, T. S. *et al.* Demonstration of the UREX Solvent Extraction Process with Dresden Reactor Fuel. 1–4 (2003).
 10. Veliscek-Carolan, J. Separation of actinides from spent nuclear fuel: A review. *Journal of Hazardous Materials* **318**, (2016).
 11. Mincher, B. J., Peterman, D. R., Mcdowell, R. G. & Olson, L. G. Radiation Chemistry of Advanced TALSPEAK Flowsheet. (2013).
 12. Starks, J. B. The PUREX Process. 1–41 (1977).
 13. Kaltsoyannis, N. Computational Study of Analogues of the Uranyl Ion Containing the $-N=U=N-$ Unit. *Inorg. Chem.* **39**, 6009–6017 (2000).
 14. Yatsimirskii, K. B. Relativistic effects in chemistry. *Theor. Exp. Chem.* **31**, 153–168 (1995).
 15. Lefort, M. & Tarrago, X. Radiolysis of water by particles of high linear energy transfer. The primary chemical yields in aqueous acid solutions of ferrous sulfate, and in mixtures of thallos and ceric ions. *J. Phys. Chem.* **63**, 833–836 (1959).
 16. Vaes, F. & Gand, D. Six nouveaux minéraux d'urane provenant de Shinkolobwe (Katanga). 212–225 (1944).
 17. Lindqvist, I. No Title. *Ark. Kemi* **5**, (1953).
 18. Keggin, J. F. The Structure and Formula of 12-Phosphotungstic Acid. *Proc. R. Soc. A*

- Math. Phys. Eng. Sci.* **144**, 75–100 (1934).
19. Hill, C. L. Progress and challenges in polyoxometalate-based catalysis and catalytic materials chemistry. *J. Mol. Catal. A Chem.* **262**, 2–6 (2007).
 20. Bijelic, A. & Rompel, A. The use of polyoxometalates in protein crystallography – An attempt to widen a well-known bottleneck. *Coord. Chem. Rev.* **299**, 22–38 (2015).
 21. Sharpless, K. B. & Flood, T. C. Oxotransition metal oxidants as mimics for the action of mixed-function oxygenases. ‘NIH shift’ with chromyl reagents. *J. Am. Chem. Soc.* **93**, 2316–2318 (1971).
 22. Kubatko, K. A., Helean, K. B., Navrotsky, A. & Burns, P. C. Stability of Peroxide-Containing Uranyl Minerals. *Science (80-.)*. **302**, 1191–1193 (2003).
 23. Goberna-Ferrón, S., Park, D.-H., Amador, J. M., Keszler, D. A. & Nyman, M. Amphoteric Aqueous Hafnium Cluster Chemistry. *Angew. Chemie* **128**, 6329–6332 (2016).
 24. Sadeghi, O., Zakharov, L. N. & Nyman, M. Crystal growth. Aqueous formation and manipulation of the iron-oxo Keggin ion. *Science* **347**, 1359–62 (2015).
 25. Wang, W., Wentz, K. M., Hayes, S. E., Johnson, D. W. & Keszler, D. A. Synthesis of the Hydroxide Cluster $[Al_{13}(\mu_3-OH)_6(\mu-OH)_{18}(H_2O)_{24}]^{15+}$ from an Aqueous Solution. *Inorg. Chem.* **50**, 4683–4685 (2011).
 26. Burns, P. C. *et al.* Actinyl peroxide nanospheres. *Angew. Chem. Int. Ed. Engl.* **44**, 2135–9 (2005).
 27. Qiu, J. & Burns, P. C. Clusters of actinides with oxide, peroxide, or hydroxide bridges. *Chem. Rev.* **113**, 1097–120 (2013).
 28. Sigmon, G. E., Weaver, B., Kubatko, K.-A. & Burns, P. C. Crown and bowl-shaped clusters of uranyl polyhedra. *Inorg. Chem.* **48**, 10907–9 (2009).
 29. Liao, Z., Deb, T. & Nyman, M. Elucidating Self-Assembly Mechanisms of Uranyl–Peroxide Capsules from Monomers. *Inorg. Chem.* **53**, 10506–10513 (2014).
 30. Ling, J., Wallace, C. M., Szymanowski, J. E. S. & Burns, P. C. Hybrid uranium-oxalate fullerene topology cage clusters. *Angew. Chem. Int. Ed. Engl.* **49**, 7271–3 (2010).

31. Unruh, D. K. *et al.* Complex nanoscale cage clusters built from uranyl polyhedra and phosphate tetrahedra. *Inorg. Chem.* **50**, 5509–16 (2011).
32. Miro, P. *et al.* Uranyl-peroxide Nanocapsules in Aqueous Solution : Force Field Development and First Applications Uranyl-peroxide Nanocapsules in Aqueous Solution : Force Field Development and First Applications. (2014).
33. Miró, P., Pierrefixe, S., Gicquel, M., Gil, A. & Bo, C. On the origin of the cation templated self-assembly of uranyl-peroxide nanoclusters. *J. Am. Chem. Soc.* **132**, 17787–94 (2010).
34. Falaise, C. & Nyman, M. The Key Role of U28 in the Aqueous Self-Assembly of Uranyl Peroxide Nanocages. *Chem. - A Eur. J.* 14678–14687 (2016).
doi:10.1002/chem.201602130
35. Schnablegger, H. & Singh, Y. *The SAXS Guide*. (2011).
36. Kikhney, A. SAXS man - Data reduction and processing.
37. Manual, I. SAXSquant 3.x.
38. Ilavsky, J., Jemian, P. R., Ilavsky, J. & Jemian, P. R. Irena : tool suite for modeling and analysis of small-angle scattering Irena : tool suite for modeling and analysis of small-angle scattering. *J. Appl. Crystallogr.* **42**, 347–353 (2009).
39. Skoog, D. A., Holler, F. J. & Crouch, S. R. *Principles of Instrumental Analysis 6th*. (2006).
40. Silverstein, R. M., Webster, F. X. & Kiemle, D. J. *Spectrometric Identification of Organic Compounds 7th*. (2005).
41. Thomas Andrews, J., Sen, P. & Sen, P. K. Optical free induction decay. *Indian J. Pure Appl. Phys.* **36**, 655–660 (1998).
42. Andrew, E. R., Bradbury, A. & Eades, R. G. Nuclear Magnetic Resonance Spectra from a Crystal rotated at High Speed. *Nature* **182**, 1659–1659 (1958).
43. Hennel, J. W. & Klinowski, J. in 1–14 (2005). doi:10.1007/b98646

44. Yannoni, C. S. High-resolution NMR in solids: the CPMAS experiment. *Acc. Chem. Res.* **15**, 201–208 (1982).
45. Reich, H. J. WinDNMR: Dynamic NMR Spectra for Windows. *J. Chem. Educ.* **72**, 1086 (1995).
46. Nyman, M. & Alam, T. M. Dynamics of uranyl peroxide nanocapsules. *J. Am. Chem. Soc.* **134**, 20131–8 (2012).

Chapter 6:

1. Starks, J. B. The PUREX Process. 1–41 (1977).
2. Goff, G. S. et al. First identification and thermodynamic characterization of the ternary U(VI) species, $\text{UO}_2(\text{O}_2)(\text{CO}_3)_2(4-)$, in $\text{UO}_2\text{-H}_2\text{O}_2\text{-K}_2\text{CO}_3$ solutions. *Inorg. Chem.* **47**, 1984–90 (2008).
3. Data, A. QUT Digital Repository: This is the author version published as : This is the author version published as. *Sport. Med.* **40**, 271–283 (2010).
4. Grenthe, I. et al. Chemical Thermodynamics of Uranium. 1992 1–735 (1992).
5. Burns, P. C. & Finch, R. J. Uranium: Mineralogy, Geochemistry and the Environment. *Mineral. Mag.* **65**, 149–150 (2001).
6. Burns, P. C. et al. Actinyl peroxide nanospheres. *Angew. Chem. Int. Ed. Engl.* **44**, 2135–9 (2005).
7. Burns, P. C. Nanoscale uranium-based cage clusters inspired by uranium mineralogy. *Mineral. Mag.* **75**, 1–25 (2011).
8. Alam, T. M., Liao, Z., Nyman, M. & Yates, J. Insight into Hydrogen Bonding of Uranyl Hydroxide Layers and Capsules by Use of ^1H Magic-Angle Spinning NMR Spectroscopy. **2**, (2016).
9. Haverbeke, L. V. A. N., Vochten, R. & Springel, K. V. A. N. Solubility and spectrochemical characteristics of synthetic chernikovite and meta-ankoleite. **60**, 759–766 (1996).

10. Jeong, S. et al. Tandem intercalation strategy for single-layer nanosheets as an effective alternative to conventional exfoliation processes. *Nat. Commun.* 6, 5763 (2015).
11. Morosin, B. Hydrogen uranyl phosphate tetrahydrate, a hydrogen ion solid electrolyte. *Acta Crystallogr. Sect. B Struct. Crystallogr. Cryst. Chem.* 34, 3732–3734 (1978).
12. Legon, A. C. & Millen, D. J. Angular geometries and other properties of hydrogen-bonded dimers: a simple electrostatic interpretation of the success of the electron-pair model. *Chem. Soc. Rev.* 16, 467 (1987).

9 Appendices

9.1 Supplementary Information for Chapter 4: Benchmarking Uranyl Peroxide Capsule Chemistry in Organic Media

Experimental Descriptions

Additional small-angle X-ray scattering notes

The instrument is equipped with a 2-d image plate for data collection in the $q=0.018\text{-}2.5\text{ \AA}^{-1}$ range. The sample to image-plate distance is 26.1 cm. SAXSQUANT software was used for data collection and treatment (normalization, primary beam removal, background subtraction, desmearing, and smoothing to remove extra noise created by the desmearing routine). Note: differences in scattering intensity in the high q -range ($\sim q > 1\text{ \AA}^{-1}$) from similar solutions is the result of imperfect background subtraction due to slight differences in capillary thicknesses and overlap between solvent scattering (increases at high q) and particle/cluster scattering. The imperfect background subtraction is a universal problem with these relatively small clusters.

Core-shell model fitting procedure

Core-shell modeling and data fitting were carried out in IgorPro 6.3 using the Modeling II macros of IRENA ^[18] for samples in which oscillations were clearly visible with no interference from solvent scattering. Initial “Core-Shell” form factor starting parameters are chosen from the metrics measured directly from the single-crystal structures of U_{24} and U_{32} , and the rho (ρ , X-ray scattering length density, related to electron density of the scattering solvent or particle) was normalized to a fixed rho for the solvent ($7 \times 10^{10}\text{ cm}^{-2}$ for kerosene or octadecene; $10 \times 10^{10}\text{ cm}^{-2}$ for water). From structural parameters, shell thickness is set to 3.5 \AA , and core radius is generally set initially to $5\text{-}7\text{ \AA}$. With these parameters, the shell rho generally refined to $50\text{-}200\text{ cm}^{-2}$, and the core rho tended towards a value lower than the solvent. (see **Table S1** for reference)

Simulated SAXS data procedure

Simulated scattering curves were produced using SolX.^[17] Structural files containing the selected portion of the structure were created as *P1* (no symmetry elements) .xyz files, which were then converted to .pdh files for data import. Scattering curves were simulated, which could also be imported into Irena and treated in the same manner as experimental data for determining R_g and generating PDDFs. R_g values were also given directly from SolX.

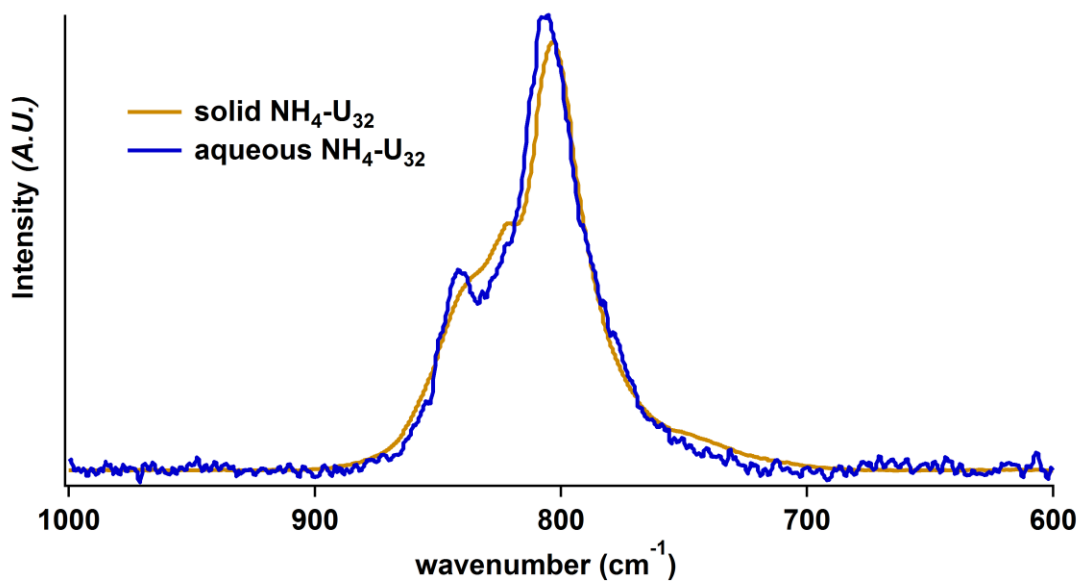


Figure S1.1

Raman spectra of NH₄-U₃₂ ($[(\text{UO}_2)_{32}(\text{O}_2)_{40}(\text{OH})_{24}]^{40-}$) in solution immediately after mixing (blue) and the solid after precipitating with alcohol (brown). The peak at 800 cm⁻¹ is typical of the γ -oxo ligand of the UO₂ unit, and the shoulder region between 820-850 cm⁻¹ is the fingerprint for the hydroxyl and/or bridging peroxide ligands of the cluster.^[11] The absence of the fingerprint terminal peroxide ligand (700 cm⁻¹) that is indicative of the uranyl triperoxide monomer is absent, which provides evidence for the immediate self-assembly of the U₃₂ cluster in the presence of ammonium, upon dissolution.

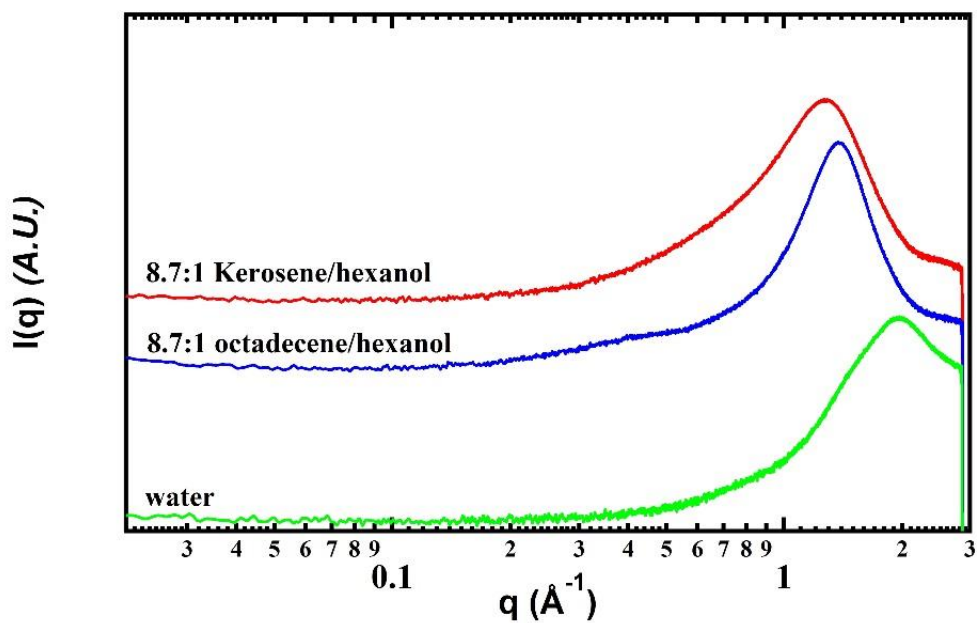


Figure S1.2

Solvent scattering of the organic extractant media and water; showing the narrower and higher- q solvent peak of the octadecene compared to kerosene, which allowed for better observation and fitting of the characteristic core-shell oscillations of the uranyl peroxide clusters. Spectrum of water is also present for comparison.

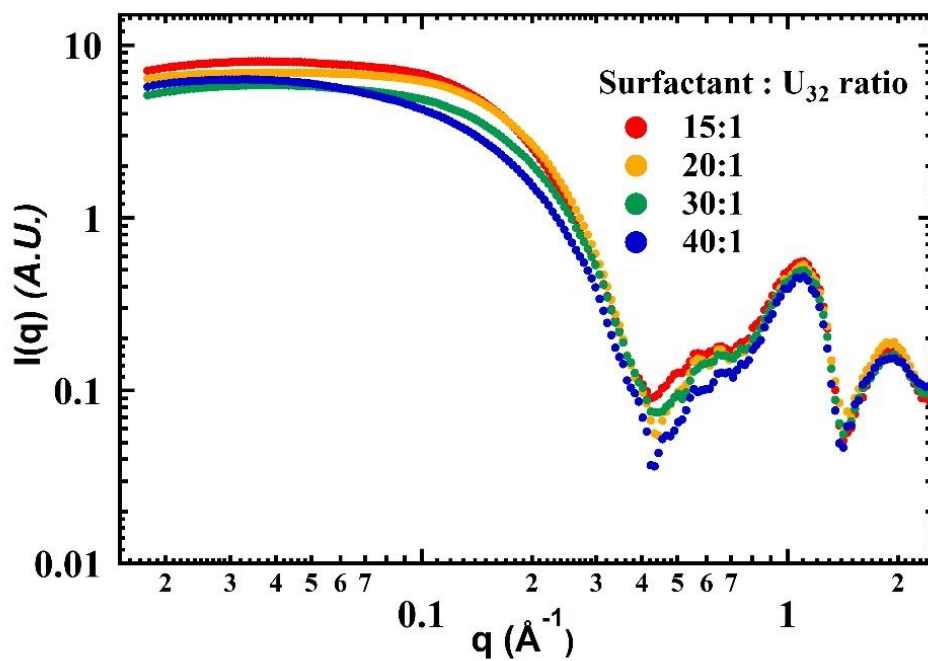


Figure S1.3

Comparison of similar SAXS scattering curves of U₃₂ extracted into kerosene with surfactant:cluster ratios of 15:1, 20:1, 30:1 and 40:1. Surfactant concentration is fixed at 0.075 molar while cluster concentration is decreased.

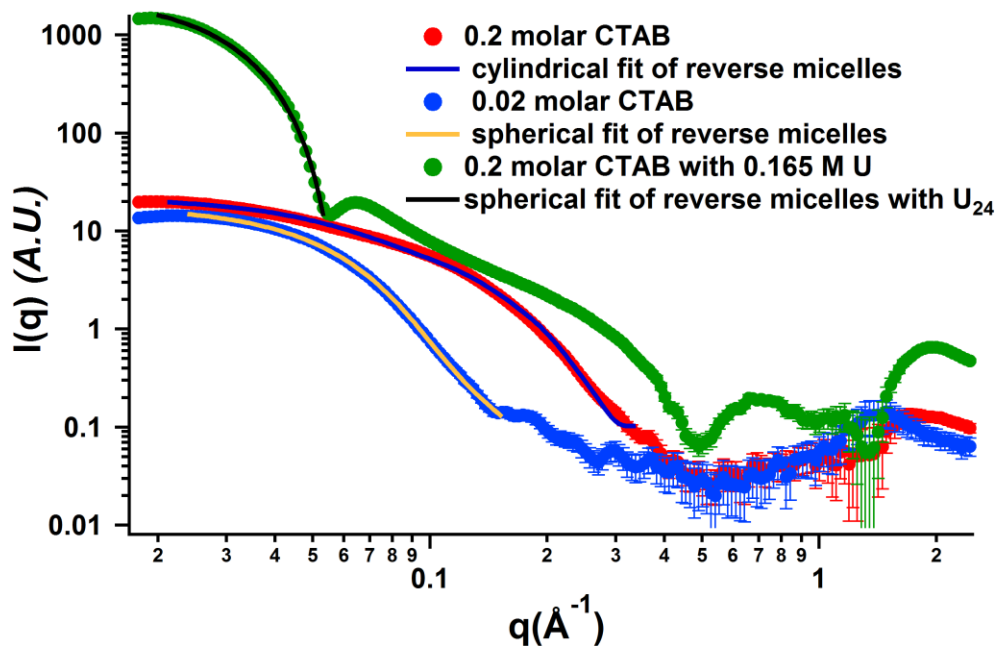


Figure S1.4

Log q -log $I(q)$ scattering curves of two concentrations of cetyltrimethylammonium bromide (CTAB) only in octadecene (blue and red spheres), and with U_{24} extracted (green spheres), along with fitting of the reverse micelle scattering. The 0.2 molar CTAB solution is fit with a cylindrical model with a length of 85 Å and a radius of 11 Å. The lower concentration CTAB micelles (0.02 M) are fit with a spherical model with an average radius of 34 Å. The 0.2 M CTAB micelles containing extracted U_{24} are best fit as spherical species with a 76 Å radius.

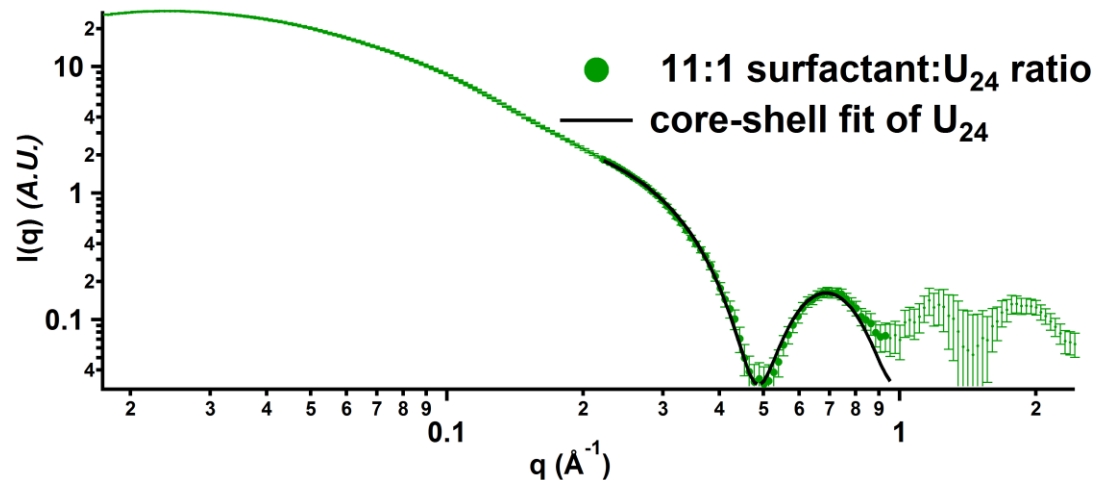


Figure S1.5

Log q -log $I(q)$ scattering curve for 11:1 surfactant:U₂₄ ratio in octadecene. A core-shell model provided the fit between $q=0.2 - 1 \text{ \AA}^{-1}$. Parameters of the core-shell fit include: core radius = 4.6 \AA ; shell thickness = 3.2 \AA ; core $\rho < 1$; shell $\rho = 80$ (10^{10} cm^{-2} ; x-ray scattering length density, normalized to $\rho = 7$ for octadecene) which agrees well with the simulated data. (see **fig. 2, Table S1**)

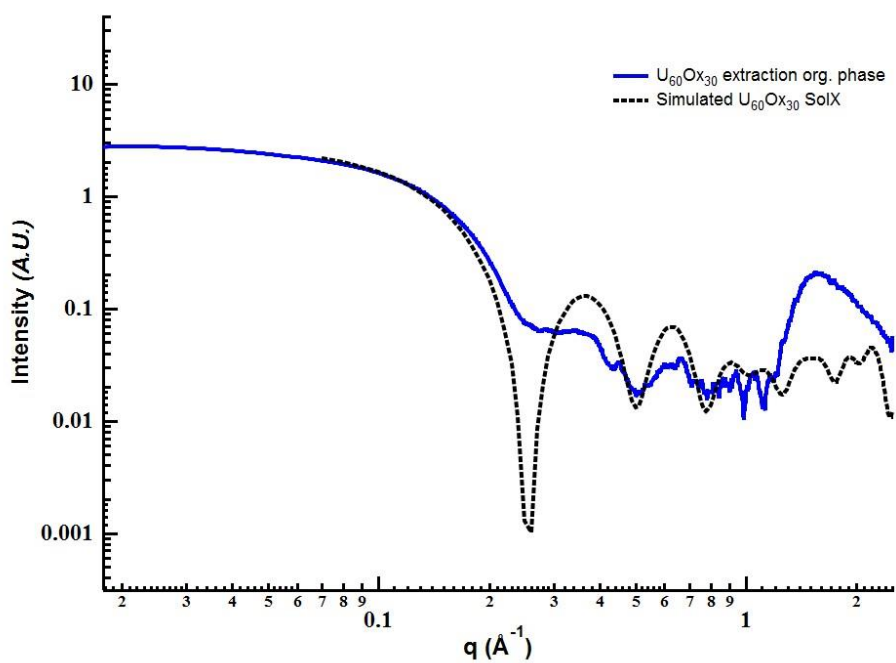


Figure S1.6

Log q -log $I(q)$ scattering curve for $U_{60}O_{x30}$ extraction. Core-shell model provided the fit between $q = 0.02 - 0.4 \text{ \AA}^{-1}$. Parameters of the core-shell fit include experimental cluster radius = 13.43 \AA , and simulated cluster radius = 13.35 \AA .

Table S1.1 Experimental X-ray Scattering Data Compared to Structure Metrics

Core-shell (cylinder) fit						
Specie	Shell thickness (Å)	Core radius (Å)	Height (Å)	Total diameter (Å)	Core ρ^1	Shell ρ^1
	Data from solution scattering					
U₂₄	2.7	4.8	N/A	15.5	0.6	200
U₃₂	2	8.5	14	21	1.3	153
	Metrics directly measured from single-crystal model					
U₂₄	3.6	4.5	N/A	16.2		
U₃₂	3.6	6.5	14	20.2		

¹Normalized to solvent (water) ρ of $10 \times 10^{10} \text{ cm}^{-2}$

Table S1.2

U₃₂ and U₂₄ Extraction Series

moles of uranium (1mL) in aqueous phase	moles of surfactant in kerosene phase (3mL)	Surfactant to cluster ratio in experiment	Surfactant to cluster ratio in experiment, rounded
LiU₂₄ extractions (octadecene & hexanol)			
0.165	0.005	2.18	2
0.165	0.01	4.36	4
0.165	0.025	10.91	11
0.165	0.05	21.82	22
0.165	0.075	32.73	33
0.165	0.1	43.64	44
0.165	0.2	87.27	87
NH₄U₃₂ extractions (precipitated and redissolved clusters)			
0.165	0.01	5.82	6
0.165	0.025	14.55	15
0.165	0.05	29.09	29
0.165	0.075	43.64	44
0.165	0.1	58.18	58
0.165	0.2	116.36	116
NH₄U₃₂ extractions (<i>in-situ</i> cluster formation)			
0.165	0.025	14.55	15
0.124	0.025	19.39	19

0.083	0.025	29.09	29
0.062	0.025	38.79	39
0.041	0.025	58.18	58
0.031	0.025	77.58	78
0.021	0.025	116.36	116

High concentration extraction (containing TMAOH, NH₄OH, uranyl, peroxide)

0.7	0.45	20.57	21
------------	-------------	--------------	-----------

Table S1.3**R_g Values from SAXS Data Analysis**

Surfactant to cluster ratio	R _g (Å)
LiU₂₄ extractions (octadecene & hexanol) – q range = 0.15 – 0.35Å⁻¹	
Simulated U ₂₄	6.6
Aqueous U ₂₄	7.2
2	8.8
4	7.7
11	8.1
22	8.5
33	8.5
44	8.4
87	8.2
NH₄U₃₂ extractions (<i>in-situ</i>) – q range = 0.10 – 0.30Å⁻¹	
Simulated U ₃₂	8.2
Aqueous U ₃₂	8.7
15	10
19	9.3
29	9.3
39	9.8
58	9.3
78	9.5

116	9.3
-----	-----

R_g from simulated data is consistently less than that from experimental data, due to the lack of contrast between the solvent (water) and external oxo ligands in ideal simulated data, generated in SolX.

9.2 Supplementary Information for Chapter 5: Resolving Confined ${}^7\text{Li}$ Dynamics of Uranyl Peroxide Capsule U_{24}

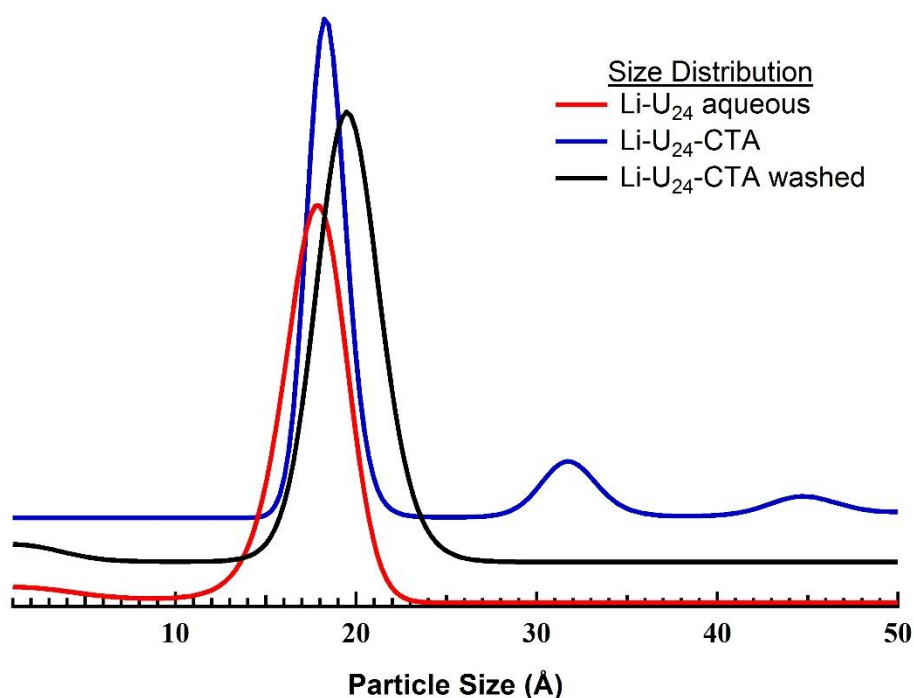


Figure S2.1 Size distribution modeling of the SAXS data shows the average particle size of the particles in solution. The aqueous Li-U_{24} (red) is modeled to fit a 17.7 \AA average cluster diameter, where the measured diameter in the crystal structure is 16.4 \AA . **Li-U₂₄-CTA** (blue) solution in kerosene is dominated by a slightly larger cluster diameter (18.2 \AA), as well as some polydispersity indicated by small populations of 31.8 \AA and 44.6 \AA diameter. Additional washing **Li-U₂₄-CTA** with water (black) eliminates polydispersity features in the SAXS data, showing a slightly larger cluster diameter of 19.5 \AA .

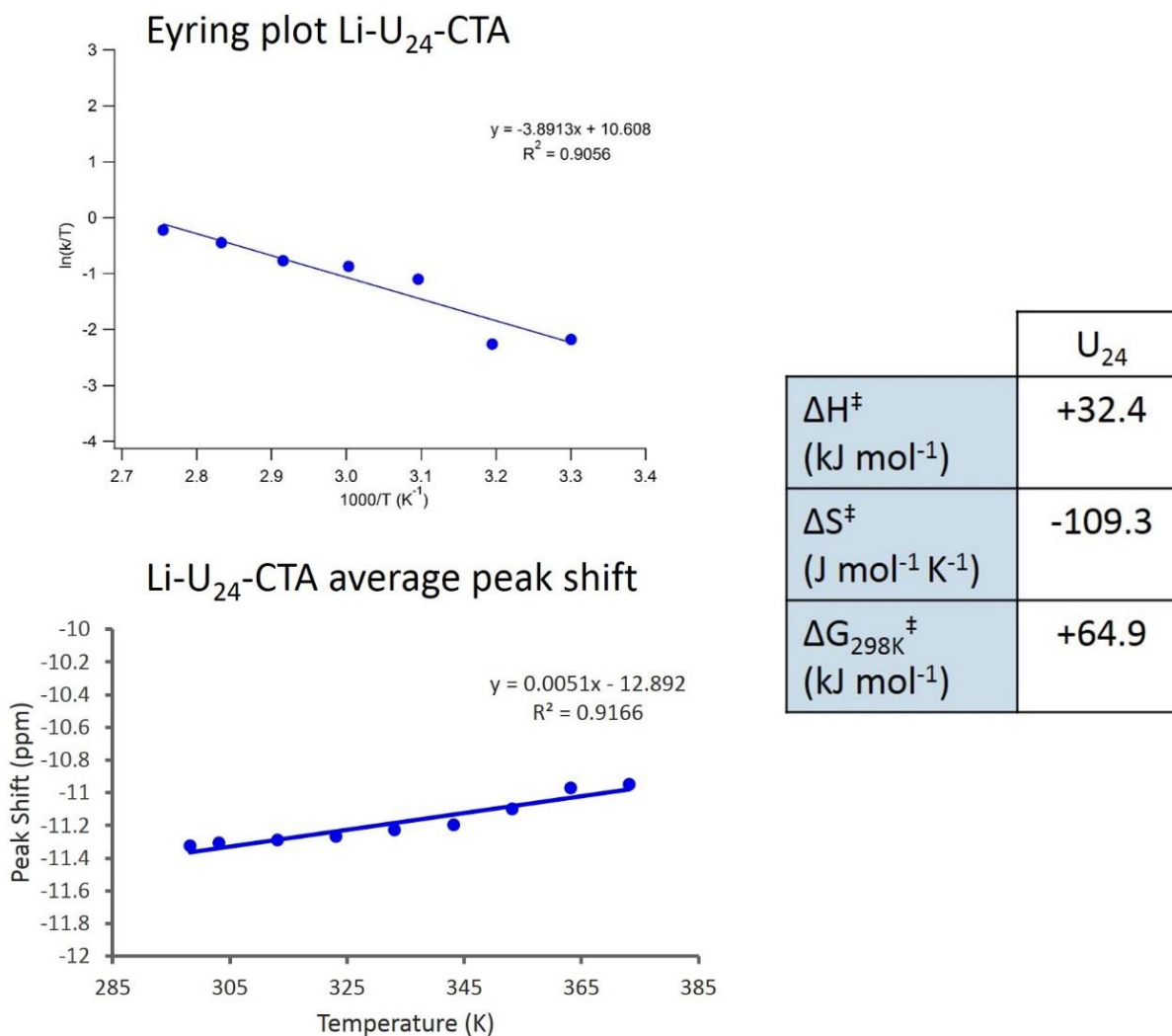


Figure S2.2 Simulated Eyring plot of ⁷Li VT-NMR data (top) acquired from **Li-U₂₄-CTA** precipitate samples. Results show a coalescence temperature (T_c) \approx 85°C, energy of exchange (ΔG_{298K}) \approx +64.9 kJ/mol and exchange rate (k_c) \approx 250 Hz. A plot of the average of the two ⁷Li VT-NMR peak shifts over the temperature range (bottom) shows a linear correlation, meaning that there is no preferred Li environment but merely an exchange of Li between the environments. The two plot points beyond the coalescence temperature were extrapolated from the simulated peak shift data.

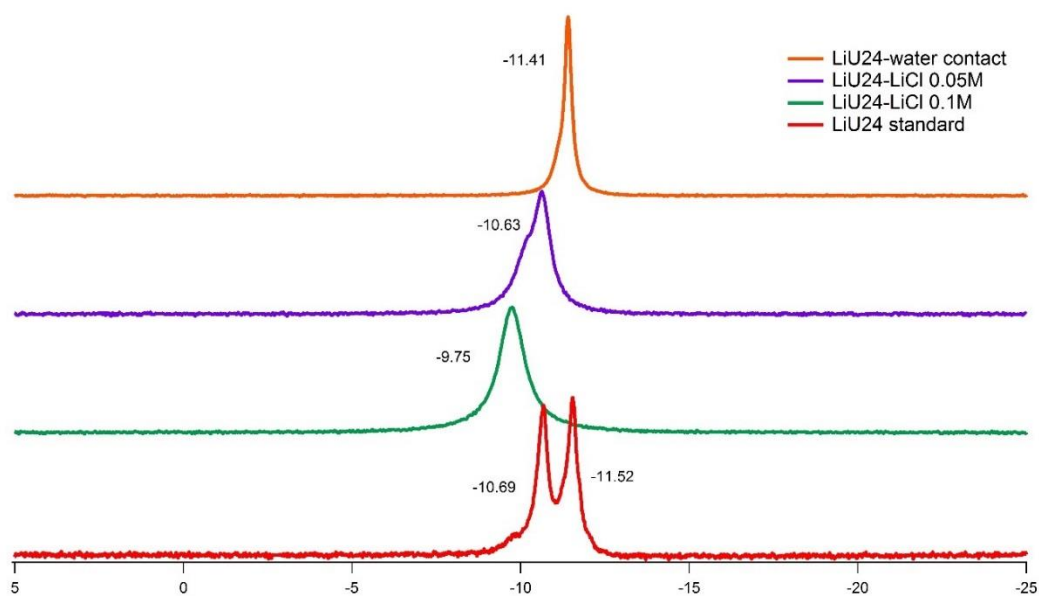


Figure S2.3 ^7Li solution NMR of various Li- U_{24} -CTA samples, contacting organic solutions with DI water (orange), 0.05M LiCl (purple), 0.1M LiCl (green) and a standard Li- U_{24} -CTA sample (red).

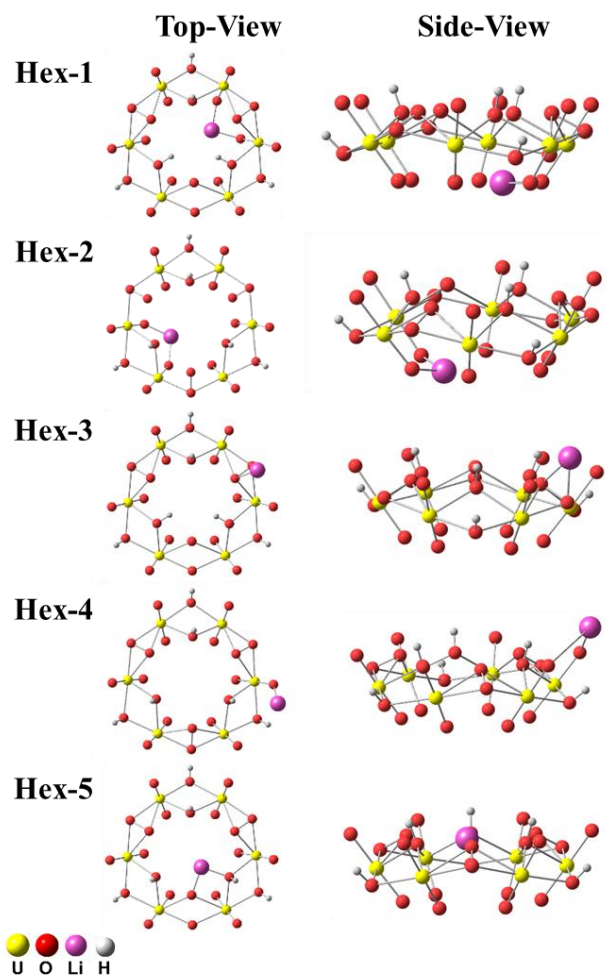


Figure S2.4. Structures of hexagon cluster models with one Li^+ cation.

Table S2.1 Chemical shift of Li cation in cluster models using different functional with SMD(water) solvent model.

Functionals	δ_{Li} (ppm), solvent=water				
Models	sq-1	sq-2	sq-3	sq-4a	sq-4b
B3LYP	-10.9	4.5	-1.5	-12.4	3.5
PBE0	-11.6	4.6	-1.4	-13.1	3.6
M06	-12.1	4.4	-1.6	-13.6	3.4
M06-2X	-16.6	6.4	-0.4	-18.2	5.2
HSE	-11.6	4.6	-1.4	-13.1	3.7
CAM-B3LYP	-11.9	4.1	-1.3	-13.3	3.1
Models	hex-1	hex-2	hex-3	hex-4	hex-5
B3LYP	-8.5	-8.7	2.2	-1.6	-5.5
PBE0	-9.0	-9.3	2.2	-1.5	-5.7
M06	-9.5	-9.8	2.0	-1.7	-5.9
M06-2X	-12.7	-13.4	3.8	-0.4	-6.9
HSE	-9.0	-9.3	2.2	-1.5	-5.7
CAM-B3LYP	-9.1	-9.5	2.2	-1.4	-5.7
Models	sq-hex-1	sq-hex-2	sq-hex-3		
B3LYP	-10.6	-9.3	-8.8		
PBE0	-11.3	-10.0	-9.5		
M06	-12.1	-10.4	-9.9		
M06-2X	-16.4	-14.4	-13.8		
HSE	-11.3	-9.9	-9.4		
CAM-B3LYP	-11.6	-10.2	-9.7		

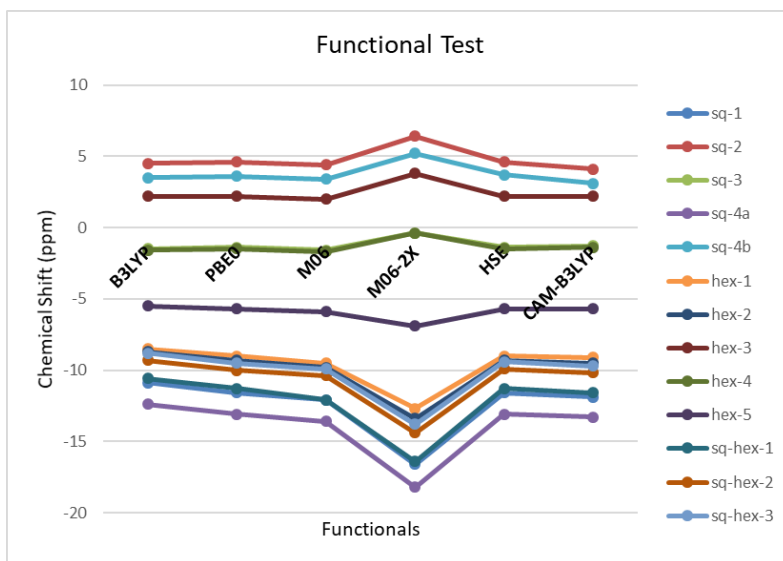


Figure S2.5 Chemical shift of Li cation in cluster models as a function of different functionals. Data are present in Table S1.

Table S2.2 Chemical shift of Li cation in cluster models using different solvents (SMD) with B3LYP. The B3LYP-“SMD=water”-optimized structures were used for all calculations.

Solvent	δ_{Li} (ppm)				
Models	sq-1	sq-2	sq-3	sq-4	
Water	-10.9	4.5	-1.5	-12.4	3.5
Benzene	-10.8	4.3	-1.6	-13.1	3.4
n-Hexane	-10.8	4.3	-1.6	-13.1	3.4
1-Hexanol	-10.9	4.5	-1.5	-12.6	3.6
cyclo-hexane	-10.8	4.3	-1.6	-13.1	3.4
Models	hex-1	hex-2	hex-3	hex-4	hex-5
Water	-8.5	-8.7	2.2	-1.6	-5.5
Benzene	-8.8	-8.8	2.1	-1.3	-5.4
n-Hexane	-8.8	-8.8	2.0	-1.3	-5.4
1-Hexanol	-8.6	-8.8	2.2	-1.5	-5.5
cyclo-hexane	-8.8	-8.8	2.1	-1.3	-5.4
Models	sq-hex-1	sq-hex-2	sq-hex-3		
Water	-10.6	-9.3	-8.8		
Benzene	-10.1	-9.1	-8.3		
n-Hexane	-10.0	-9.1	-8.2		
1-Hexanol	-10.5	-9.3	-8.8		
cyclo-hexane	-10.0	-9.1	-8.3		

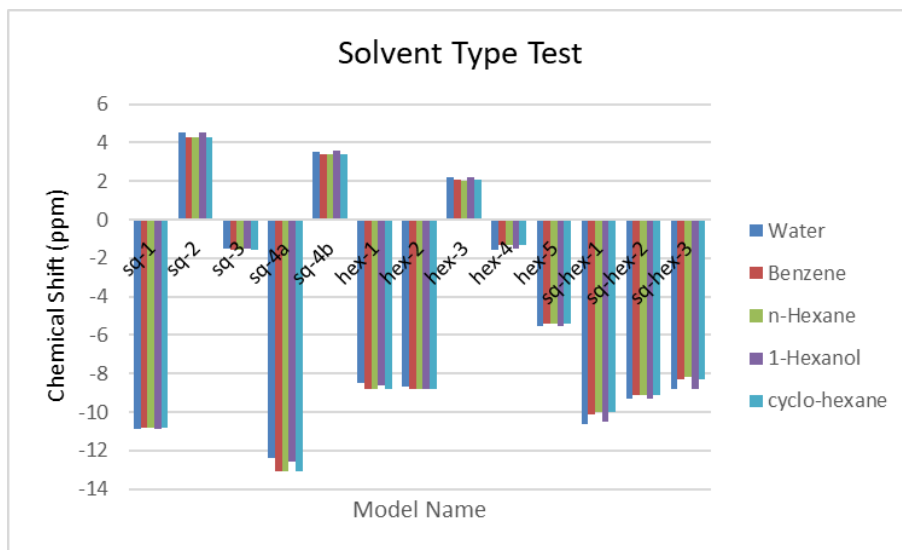


Figure S2.6 Chemical shift of Li cation in cluster models as a function of solvent types. Data are present in Table S2.

Table S2.3 Chemical shielding and chemical shift of Li cation in cluster models. Both structure optimization with constraints and NMR calculations were performed in solvent of water, hexanol, and cyclohexane, respectively, using SMD solvent model and B3LYP functional.^a

Species	Chemical Shielding (ppm)			Chemical Shift (ppm)		
	Water	Hexanol	CycloHexane	Water	Hexanol	CycloHexane
Li ⁺	95.1	95.1	95.1	-4.1	-4.1	-4.1
LiCl	93.4	93.3	92.8	-2.4	-2.3	-1.8
sq-1	101.9	101.7	104.1	-10.9	-10.7	-13.1
sq-2	86.5	87.0	88.1	4.5	4.0	2.9
sq-3	92.5	92.5	92.6	-1.5	-1.5	-1.6
sq-4 a	103.4	103.3	106.3	-12.4	-12.3	-15.3
sq-4 b	87.5	87.5	88.9	3.5	3.5	2.1
sq-5 a	97.9			-6.9		
sq-5 b	101.0			-10.0		
hex-1	99.5	100.3	101.3	-8.5	-9.3	-10.3
hex-2	99.7	99.8	100.0	-8.7	-8.8	-9.0
hex-3	88.8	92.5	92.2	2.2	-1.5	-1.2
hex-4	92.6	91.1	91.5	-1.6	-0.1	-0.5
hex-5	96.5	89.0	89.3	-5.5	2.0	1.7
sq-hex-1	101.6	102.0	102.5	-10.6	-11.0	-11.5
sq-hex-2	100.3	100.6	101.4	-9.3	-9.6	-10.4
sq-hex-3	99.8	99.4	-	-8.8	-8.4	-

^aThe dielectric constant of water, 1-hexanol, benzene, cyclohexane, and n-hexane is 78.36, 12.51, 2.27, 2.02, and 1.88, respectively. Since the dielectric constant of benzene, cyclohexane, and n-hexane are similar, we chose to optimize the structures with solvent of cyclohexane as represent.

Table S2.4 ^7Li NMR chemical shift scan in the square model. B3LYP/6-31G(d,p)&SDD with water (SMD) as solvent.

Z-coordinate (Angstrom)	Li chemical shift (ppm)	Relative energy (kcal/mol)
0.00	-6.7	43.4
1.00	-8.4	41.9
2.00	-11.5	35.0
3.00	-14.8	13.1
3.25	-14.9	7.7
3.50	-14.3	3.5
3.75	-13.0	1.0
3.81	-12.6	0.7
4.00	-10.9	0.0
4.25	-8.5	1.7
4.75	-4.0	12.7
5.00	-2.1	19.3
5.50	1.8	27.8
6.00	5.7	29.0
7.00	6.1	19.9

Table S2.5 ^7Li NMR chemical shift scan in the hexagon model. B3LYP/6-31G(d,p)&SDD with water (SMD) as solvent.

Z-coordinate (Angstrom)	Li chemical shift (ppm)	Relative energy (kcal/mol)
0.61	-8.8	20.6
1.48	-10.3	18.2
2.34	-11.1	14.0
3.21	-9.7	8.8
4.07	-6.3	7.9
4.94	-2.5	6.5
5.37	-1.0	3.4
5.81	0.0	0.6
6.24	0.5	0.0
6.67	0.4	2.1

Table S2.6 Li NMR chemical shift, Li position, and structure formation energies^a as a function of water molecules in square model. B3LYP/6-31G(d,p)&SDD with water (SMD) as solvent.

Square Model	n (number of water molecules)					
	0	1	2	3	4	5
	chemical shift of Li (ppm)					
top set	-10.9	-13.5	-13.2	-12.7	-12.9	-12.6
bottom set		-12.5	-9.7	-12.3	-12.1	
	distance of Li to cage center (Å)					
top set	4.00	3.67	3.57	3.56	3.57	3.56
bottom set		3.64	2.45	3.61	3.61	
	formation energy (kcal/mol)					
top set	-44.0	41.3	25.7	17.0	11.4	3.7
bottom set		-57.3	-62.4	-71.4	-78.8	

^aThe formation energy is calculated as the electronic energy of formation reaction $n\text{H}_2\text{O} + \text{Li}^+ + \text{sq} \rightarrow \text{Li}^+(\text{nH}_2\text{O})@\text{sq}$, where n is the number of water molecule, sq stands for the square model, and $\text{Li}^+(\text{nH}_2\text{O})@\text{sq}$ is the complex.

9.3 Supplementary Information for Chapter 6: Synthetic Pathways and Exfoliation of Uranyl Phosphate Layered Materials

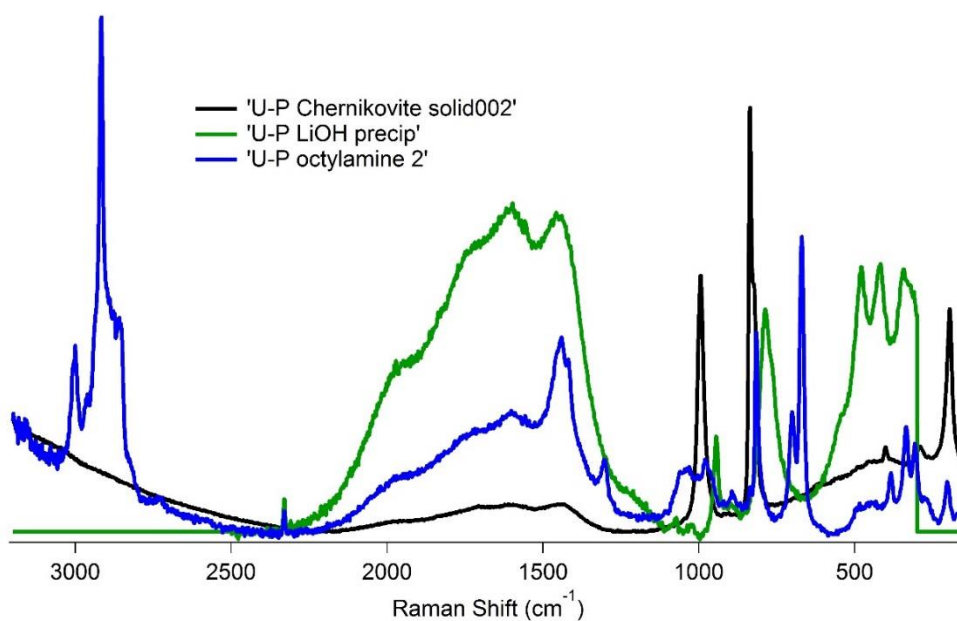


Figure S3.1: Raman spectra of solid samples of chernikovite including synthesized chernikovite (black), delaminated chernikovite with octylamine in DMSO.

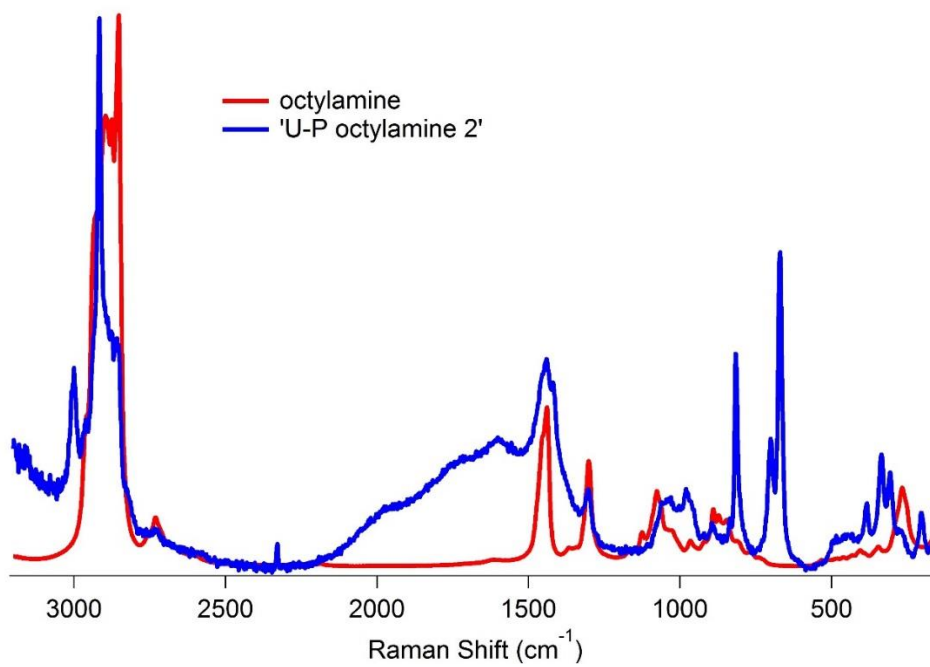


Figure S3.2: Raman spectra comparing delaminated chernikovite sample with a stock solution of octylamine.

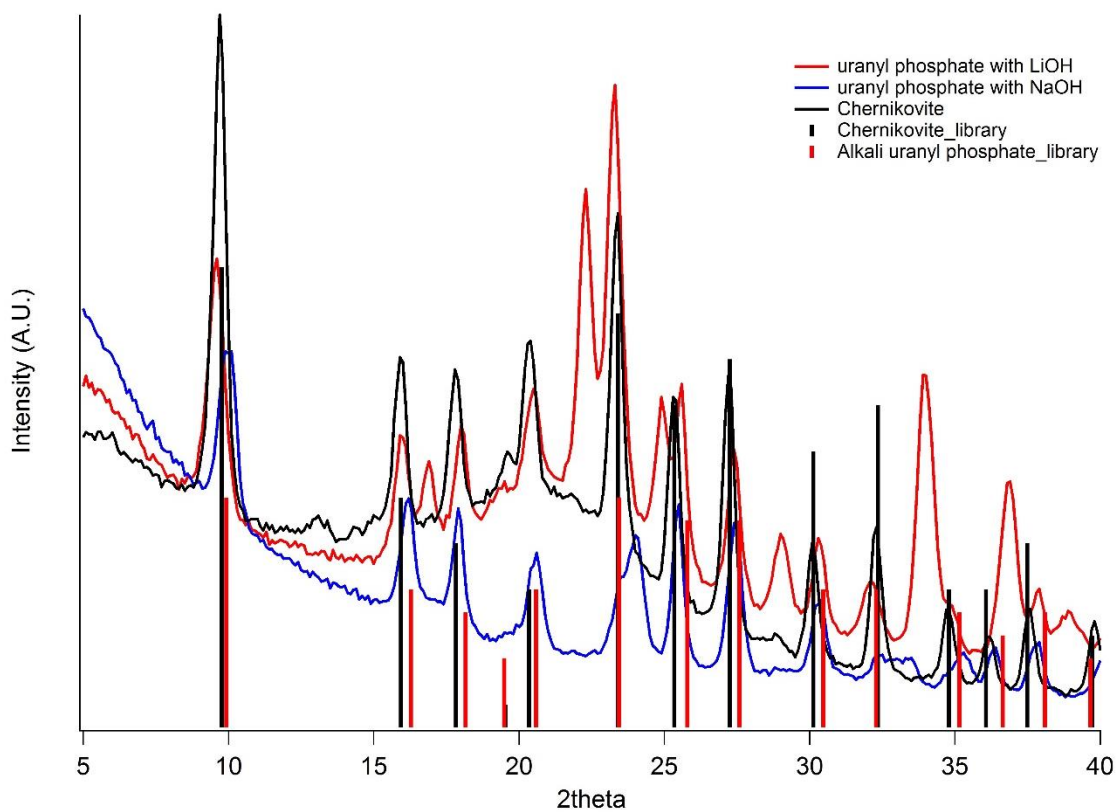


Figure S3.3: Powder X-ray diffraction of chernikovite, Li uranyl phosphate, and Na uranyl phosphate samples. The Li and Na samples were synthesized by adding LiOH and NaOH solutions, respectively, to a combination of uranyl nitrate and phosphoric acid.

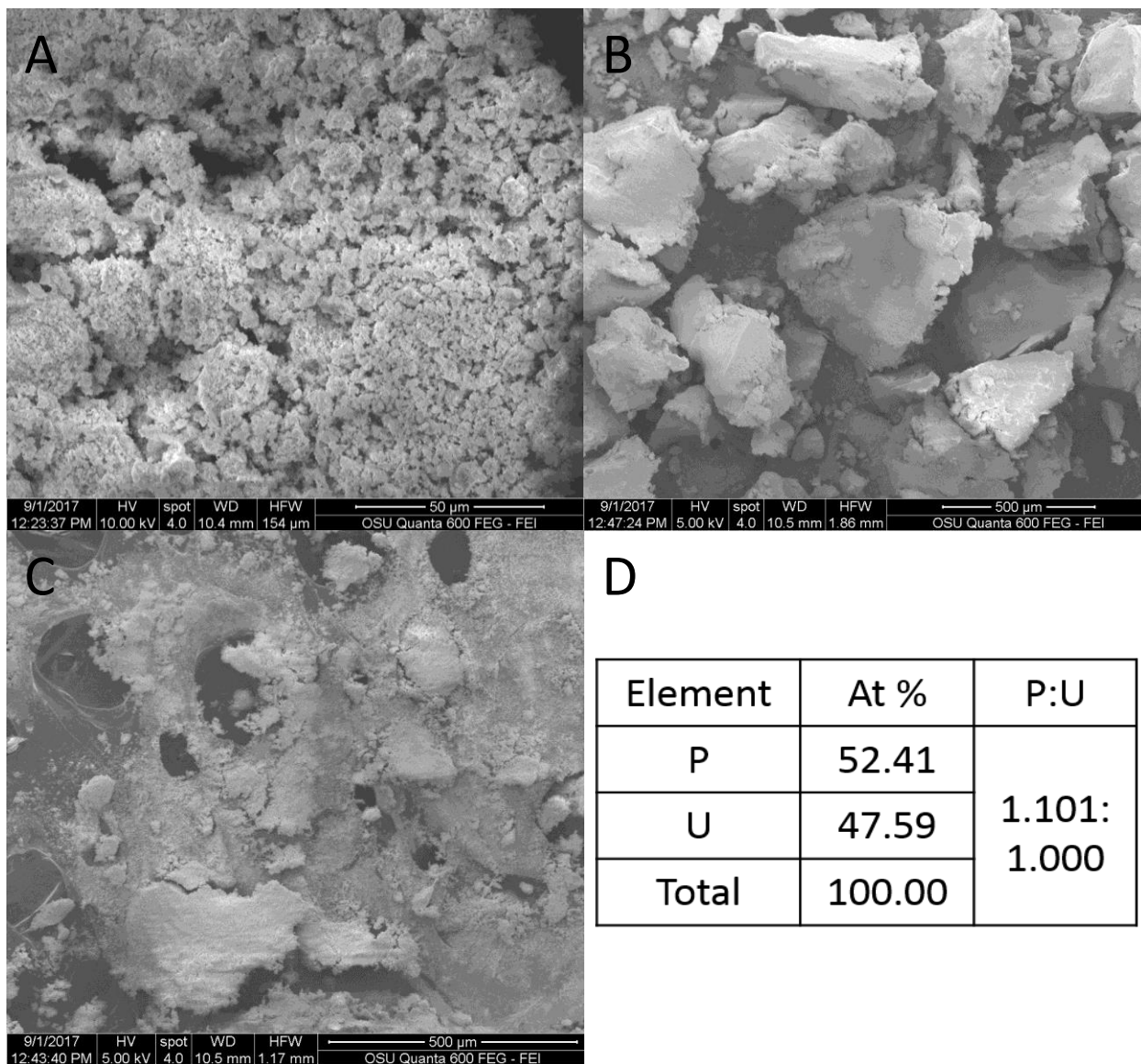


Figure S3.4: A) chernikovite B) hexylamine delamination C) octylamine delamination D) compositional analysis of chernikovite

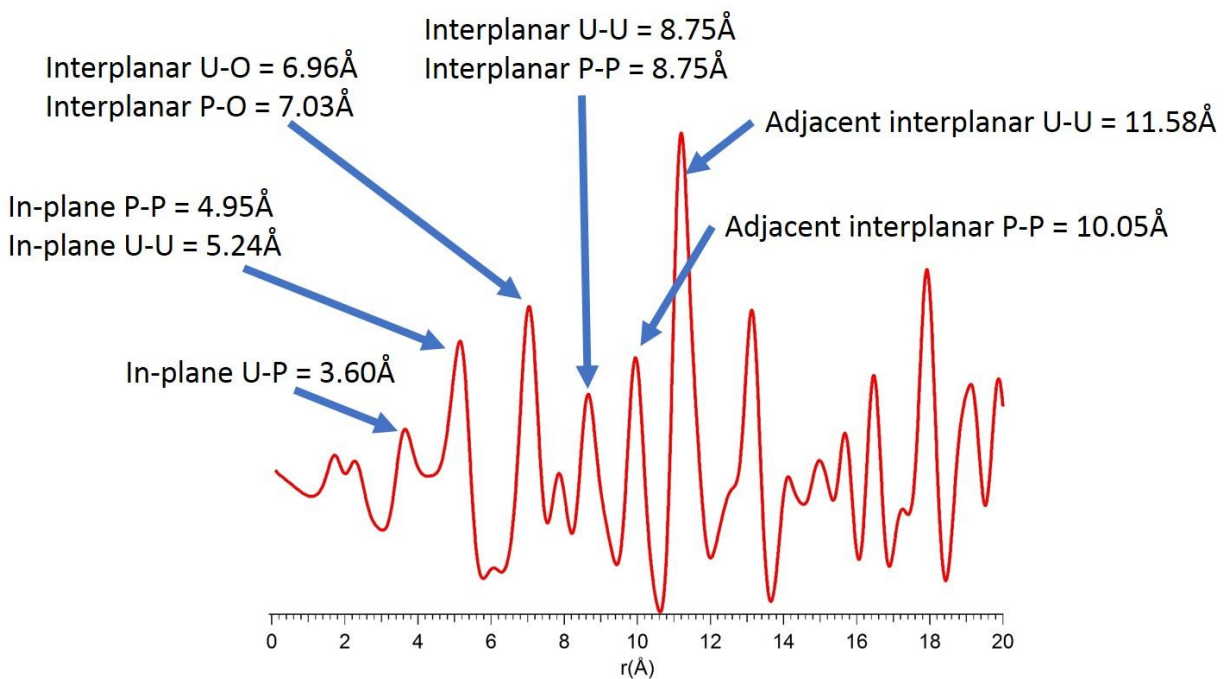


Figure S3.5: Simulated PDF peaks of chernikovite. The peaks correspond to populations of atom-atom distances found in the local structure of the solid. Each atom-atom distance is labeled appropriately from crystal structure measurements.